

Equilibrium and Dynamic Phase Behavior in Thin Films of Cylinder-Forming Block Copolymers

DISSERTATION

zur Erlangung des akademischen Grades eines
Doktors der Naturwissenschaften

- Dr. rer. nat. -

im Fach Chemie der Fakultät Biologie, Chemie und Geowissenschaften
der Universität Bayreuth

vorgelegt von

Armin Knoll

geboren in Rehau

Bayreuth, 2003

Die vorliegende Arbeit wurde in der Zeit von November 1998 bis Juni 2003 am Lehrstuhl für Physikalische Chemie der Universität Bayreuth in der Arbeitsgruppe von Herrn Prof. Dr. Georg Krausch angefertigt.

Der vorliegende Text ist ein vollständiger Abdruck der Dissertation, die von der Fakultät für Biologie, Chemie und Geowissenschaften der Universität Bayreuth genehmigt wurde.

1. Gutachter: Prof. Dr. G. Krausch

2. Gutachter: Prof. Dr. A. Müller

Promotionsgesuch eingereicht am: 02. Juli 2003

Tag des wissenschaftlichen Kolloquiums: 16. April 2004

Meinen Eltern

Anyone who has never made a mistake has never tried anything new.
Albert Einstein.

Contents

1	Introduction	1
1.1	Block Copolymers	2
1.1.1	Microphase separation	3
1.1.2	Phase Diagram for AB Diblock Copolymers	5
1.1.3	Block Copolymers and Solvents	7
1.1.4	ABA triblock copolymers	9
1.1.5	Surfaces and Thin Films	10
1.1.6	Dynamics of Structure Formation in Block Copolymers	13
1.2	Overview of Thesis	15
2	Materials and Methods	17
2.1	Polymers	17
2.1.1	Polystyrene- <i>b</i> -polybutadiene- <i>b</i> -polystyrene (SBS) triblock copolymer	17
2.1.2	Homopolymers	19
2.2	Characterization	19
2.2.1	Scanning Force Microscopy (SFM)	19
2.2.2	Ellipsometry	22
2.2.3	Small Angle X-ray Scattering (SAXS)	24
2.2.4	Optical Microscopy	25
3	Where Is the True Sample Surface?	27
3.1	Introduction	28
3.2	Experimental Section	30
3.3	Results and Discussion	31
3.4	Conclusion	42

Contents

4	Strong Segregation Theory of Thin Films	45
4.1	Introduction	46
4.2	Theory	48
4.3	Results	50
4.3.1	Example: Rectangular unit cell	50
4.3.2	Thin film unit cells for in plane oriented cylinders	52
4.3.3	Effect of Surface Tension	55
4.3.4	Terrace Heights	55
4.3.5	Comparison to other Structures	58
4.4	Conclusion	61
5	Phase Behavior	63
5.1	Introduction	64
5.2	Experimental	66
5.2.1	Materials	66
5.2.2	SAXS	67
5.2.3	Thin Film Preparation	67
5.2.4	Ellipsometry	68
5.2.5	Scanning Force Microscopy (SFM)	69
5.3	Results	69
5.3.1	Domain spacing in bulk SBS solutions	69
5.3.2	Swelling behavior and molecular interactions in thin SBS films	71
5.3.3	Coarse grain structure of the SBS films: Terrace formation	73
5.3.4	Thin film microdomain structure	74
5.3.5	Identification of the microdomain structure	79
5.3.6	Phase diagram	82
5.4	Discussion	84
5.5	Conclusion	88
6	Principal Dimensions of the Microdomain Structure	91
6.1	Introduction	92
6.2	Experimental	94
6.2.1	Materials	94
6.2.2	Preparation	94

6.2.3	SFM	95
6.3	Results and Discussion	95
6.3.1	Orientational Correlation of the C_{\parallel} Structure	97
6.3.2	Effect of curvature on the microdomain spacing	102
6.3.3	The Microdomain Spacing as a Function of Film Thickness	105
6.3.4	Comparison of Relevant Dimensions	109
6.3.5	Conclusion	113
6.4	Appendix: Image Analysis - Determination of the Characteristic Spacings	114
7	Dynamics of Structure Formation	119
7.1	Introduction	120
7.2	Material and Method	122
7.2.1	Solvent vapor control	122
7.2.2	<i>In-situ</i> Scanning Force Microscopy	123
7.2.3	Movies	124
7.2.4	Noise Reduction	125
7.2.5	Defect Recognition in the PL structure	126
7.3	Results	126
7.3.1	Overview of the experiment	126
7.3.2	Fast Dynamics	128
7.3.3	Phase Transition: C_{\perp} to C_{\parallel}	130
7.3.4	Transition from C_{\parallel} to PL	132
7.3.5	Defect Movement in the Perforated Lamellar Phase	136
7.4	Conclusion	143
7.5	Appendix: Registration, Alignment and Filtering	144
8	Summary / Zusammenfassung	147
9	Bibliography	155
10	List of Publications	169

Contents

List of Figures

1.1	Five regimes of block copolymer segregation and/or molecular conformation	4
1.2	Experimental and predicted phase diagrams	6
1.3	ABA triblock copolymer phase diagram	10
2.1	Schematic setup of a scanning force microscope	20
2.2	Resonance curve of a harmonic oscillator representing the excited cantilever system	21
3.1	Typical amplitude vs. distance and phase vs. distance curve measured on the SBS sample.	32
3.2	Height images measured with conventional TM-SFM and True Surface images	34
3.3	Comparison of indentation and phase signal determined from APD curves with the respective TM-SFM height and phase images	36
3.4	Indentation and phase signal vs <i>set point</i> A/A_0 taken in the center of PS- and PB-rich areas	37
3.5	Indentation as well as the “true surface”	41
4.1	Wedge used for building up cylindrical structures	48
4.2	Unit cells of a thin film	52
4.3	Free energy per molecule $F_{\parallel}(b, n)$	54
4.4	Free energy per unit area $\Delta\Gamma_{\parallel}(b, n)$	54
4.5	Free energy per area and common tangents of neighboring energy ‘parabolas’	56
4.6	The lateral cylinder spacing, i.e. the width of the unit cell, and the thickness of one cylinder layer as function of the number of cylinder layers	57

List of Figures

4.7	Other structures considered for the thin film than the C_{\parallel} structure	58
4.8	Phase Diagram of stable structures as a function of film thickness and relative surface tension of the A block	60
5.1	Sketch of the experimental setup for swelling in chloroform vapor	68
5.2	SAXS spectra from an SBS bulk sample and SBS $CHCl_3$ solutions	70
5.3	Polymer volume fraction ϕ_P as a function of the relative $CHCl_3$ vapor pressure	71
5.4	Optical micrographs of swollen films as a function of annealing time	73
5.5	In-situ tapping mode SFM phase images	74
5.6	3D rendered SFM images	75
5.7	SFM phase images at the edges of terraces as a function of film thickness h and polymer concentration ϕ_P	76
5.8	Cross sections across terrace steps of the height images	77
5.9	True Surface SFM of a thin SBS film	79
5.10	Comparison to computer simulations	81
5.11	Phase diagram of observed surface structures	84
5.12	Terrace height h_T and relative thickness of a cylinder layer	85
6.1	Phase image of a SBS film with thickness between one (T1) and two layers of cylinders (T2)	96
6.2	Results of the image analysis algorithm for two AFM phase images	99
6.3	Orientational correlation functions for the two samples	100
6.4	Example of the measured spacing in the C_{\parallel} structure as a function of the local curvature of the cylinders	102
6.5	Simple Model of diblock copolymer PS-PB forming a two dimensional lamella	103
6.6	Plots of the microdomain spacing versus the local film thickness .	106
6.7	Comparison of the relevant dimensions measured in the thin films	110
6.8	Filling of the binarized phase image	115
6.9	Examination of the neighborhood of the C_{\parallel} structure	117
7.1	Setup for the <i>in-situ</i> measurements	123
7.2	Position of the captured frames in time plotted as dots along the time axis	127
7.3	Fast reorientation process of the local microdomain structure	129

List of Figures

7.4	Phase transition from C_{\perp} to C_{\parallel}	131
7.5	Nucleation of the PL phase	133
7.6	Reordering of a PL grain to minimize the PL - C_{\parallel} boundary	134
7.7	Three examples of the growth of the PL grains in time	135
7.8	Schematic representation of the basic processes involving defect formation and translation	137
7.9	Two sequences of frames, which depict the experimentally found processes of dislocation glides	138
7.10	Three processes of dislocation climbs found experimentally	140
7.11	Reversible process of the annihilation of two extra half rows of material	141
7.12	T_1 and T_2 processes	142
7.13	Illustration of the non orthogonal lattices used to remove distortions induced by the non linearity of the scanning	144

List of Figures

1 Introduction

In this thesis an in depth discussion of equilibrium structures and the pathway of structure formation in a thin film of cylinder forming block copolymers is presented.

Block copolymers self assemble into a variety of structures with mesoscopic length scales of 5 to 100 nm. Only recently the potential of thin block copolymer films for applications receives increasing interest. They may be used for lithographic purposes [Par97, Gua02, Bla01, Par01, Che01], and/or templating of inorganic structures [TA00a, TA00, Li00]. The patterns may be aligned by the use of external electric fields [Mor96a], topographic templating [Seg01] and surface patterning [Hei99]. All these processes rely on the control of pattern formation of the block copolymer in thin films and therefore on a good understanding of the underlying physics.

Most of the scientific work has been done on thin block copolymer films of lamella forming block copolymers. Nevertheless typical applications require patterns in lateral direction of the thin film, which typically cannot be accomplished by the use of lamellar forming block copolymers. Therefore often conformationally asymmetric block copolymers with a non lamellar bulk structure are used, in majority cylinder forming polymers. For these systems a variety of thin film structures has been observed (for a summary of experimental results see [Wan01]). Various models have been developed to describe their complex behavior [Tur94, Hui00, Per01, Wan01] (for summary see Ref. [Wan01]), but modelling and experimental results agree qualitatively only in parts. In this thesis we systematically investigate the phase behavior of cylinder forming block copolymers in thin films.

To this extend a model system was chosen, which forms glassy cylinders in a rubbery matrix in bulk and is therefore ideally suited for thin film characterization by scanning force microscopy (SFM). In conventional tapping mode the SFM is capable of imaging the glassy cylinders, although they are buried un-

1 Introduction

derneath a rubbery surface layer. On the other hand the indentation of the tip introduces height artifacts depending on the local sample elasticity and the parameters of operation. In this thesis we present a method to *quantify the amount of indentation*, which in turn allows us to reconstruct a *True Surface* image and a *reliable identification* of the recorded microdomain structure.

A novel method of thin film sample preparation has been established by annealing the thin film in a *controlled* atmosphere of constant solvent vapor pressure, which resulted in a very reproducible sample preparation. Introducing a *constant* amount of solvent to the system not only enhances the mobility of the block copolymer chains but also changes the effective polymer-polymer and polymer-surface interactions in the system depending on the solvent concentration. In this sense we study the microdomain structure in the thin film not only as a function of film thickness but also as a function of the inherent interactions.

SFM provides the means to *quantitatively* study the dimensions of the microdomain structure in the thin films. A detailed analysis of the microdomain spacing as a function of film thickness and other parameters was possible with the help of a novel image analysis algorithm. The surprising results were compared to theoretical predictions of a novel extension of an advanced strong segregation theory of Olmsted and Milner [Olm94] to thin films.

The pathway of structure formation in the thin films gives additional insight into the physics of the system. We use the possibility of the SFM to nondestructively image the sample surface in a solvent vapor atmosphere to establish the first *in-situ* measurements of the microdomain dynamics in thin block copolymer films.

1.1 Block Copolymers

Block copolymers belong to the class of ordered fluids, which display crystal like order on a mesoscopic length scale and fluid like order at a microscopic scale. The mesoscopic structure formation in these systems is driven by competing interactions and may be described in an universal way with other systems by the phenomenology of modulated phases [Seu95]. In this picture mesoscopic domains represent modulations in some order parameter. In the case of block copolymers this order parameter is usually defined as the local volume fraction of the mi-

1.1 Block Copolymers

nority block, while other examples are the magnetization in thin epitaxial films of rare earth garnets, polarization e.g. in ferroelectric films, density fraction of superconductivity. The competing interactions are usually short range repulsive forces, e.g. due to incompatibility of the components in a two component system, and long range attractive forces like dipole moments or molecular connectivity in the case of block copolymers. The modulation period is determined by the relative strength of the competing interactions.

1.1.1 Microphase separation

The formation of modulated phases in the case of block copolymers is called microphase separation. Block copolymers are built from two or more immiscible polymeric chains, called blocks, which are covalently attached to each other. The incompatibility of the monomers of different blocks provides the short range repulsive interaction, which drives a phase segregation of the blocks into domains rich of only one component. A macroscopic phase separation is prohibited due to the covalent bonds linking the blocks.

The simplest block copolymer consists of two blocks A and B linearly attached to each other. On the level of mean field theory, two parameters control the phase behavior of diblock copolymers: The volume fraction of the A block f , and the interaction between the blocks $\chi_{AB} N$, where χ_{AB} is the Flory parameter measuring the interaction between the A and B monomers and N is the degree of polymerization of the block copolymer [Bat90, Oht86, Mat94a].

If there are no strong specific interactions between A and B monomers like hydrogen bonding or charges, the interaction parameter χ_{AB} is usually small compared to unity and positive. Positive values of χ_{AB} indicate a net enthalpic repulsion of the monomers. χ_{AB} is typically inversely proportional to the temperature of the system, therefore mixing of the blocks is typically enhanced at elevated temperatures.

If $\chi_{AB} N$ is large enough the system tries to minimize the nonfavorable contacts between A and B monomers by microphase separation. The induced order incorporates some loss of translational and configurational entropy. If the temperature of the system increases and χ_{AB} decreases, the entropic factors will eventually dominate and the system will become disordered. This process is called order-disorder transition (ODT) and the respective temperature order-disorder

1 Introduction

transition temperature (T_{ODT}). Since the enthalpic and entropic contributions scale as χ_{AB} and N^{-1} , respectively, the product $\chi_{AB}N$ controls the phase state of the polymer.

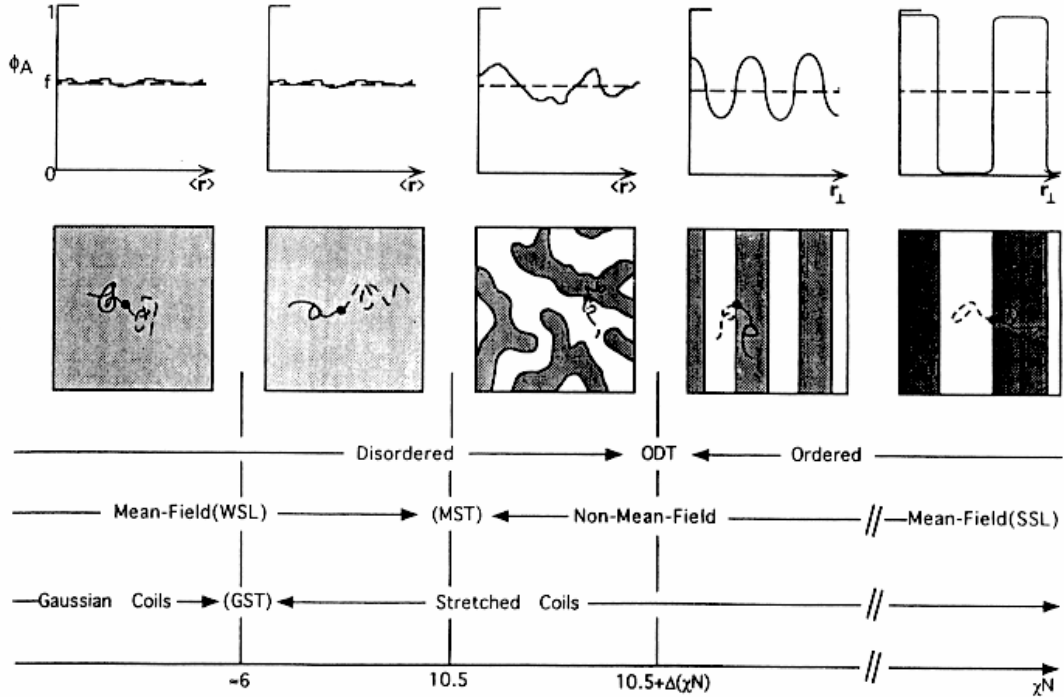


Figure 1.1: Five regimes of block copolymer segregation and/or molecular conformation [Ros95]. The borders are marked by the Gaussian to stretched (coil) transition (GST), the microphase separation temperature (MST), the order-disorder transition (ODT) and the limit of strong segregation (SSL). Depicted are from top to bottom the composition profile, the state of order and the definition of regimes depending on order, theoretical treatment and chain conformation as a function of the interaction χN .

The amount of segregation and the molecular conformation of a block copolymer melt can be divided into five regimes with increasing interaction $\chi_{AB}N$. Figure 1.1 shows from top to bottom the density profile perpendicular to the formed structures, the lateral structure formed in the system and the definition of regimes depending on order, theoretical treatment and chain conformation as a function of $\chi_{AB}N$.

At low interactions, $\chi_{AB}N < 10.5$, the composition profile is sinusoidal and the chain statistics are Gaussian, which implies that the radius of gyration of the molecules R_g scales with N as $R_g \sim N^{1/2}$ [Ros95]. This regime is referred

1.1 Block Copolymers

to as the "weak segregation limit" (WSL). Considerably below $\chi_{AB}N = 10.5$, at the Gaussian-to-stretched (coil) transition (GST), the diblock chains become stretched [Alm90]. Rosedale et al. experimentally found this transition to occur at $\chi_{AB}N \approx 6$ [Ros95], while Fried and Binder reported a GST at $\chi_{AB}N \approx 4$ based on Monte Carlo Simulations [Fri91]. The microphase separation transition (MST) occurs at $\chi_{AB}N = 10.5$ and does not necessarily coincide with the order disorder transition (ODT), which separates regions characterized by broken translational and orientational symmetry from the disordered state. This region is heavily influenced by composition fluctuations, which have been found responsible for the shift of the ODT away from the MST. The fluctuations become less important in the case of large N , and the ODT approaches the MST for constant $\chi_{AB}N$ and $N \rightarrow \infty$. For large interactions the interface between the blocks narrows and separates almost pure A and B microdomains. This regime is called the strong segregation limit (SSL) and is characterized by highly stretched chains, where the domain spacing d scales as $d \sim N^{2/3} \chi_{AB}^{1/6}$.

Since the Mean field treatments do not account for fluctuations, the intermediate regimes cannot be addressed strictly by these techniques. In the SSL fluctuations become unimportant and a mean field treatment can be applied.

1.1.2 Phase Diagram for AB Diblock Copolymers

An early self consistent (mean) field theory (SCFT) of the microphase separation has been developed by Helfand et. al. [Hel76, Hel78, Hel80]. The theory established first approximations for the phase diagram in terms of $\chi_{AB}N$ and f of an AB diblock and an ABA triblock copolymer for spherical, cylindrical and lamella forming phases. Leibler [Lei80] introduced a calculation of the ODT as a function of f for weakly segregated systems, i.e. for $\chi_{AB}N$ slightly larger than the respective ODT value. In the limit of infinitely long chains, the so called strong segregation limit, Semenov developed an alternative analytical approach [Sem85].

A very powerful method to calculate the properties of the microdomain phases was developed by Matsen and Schick [Mat94a]. They use an appropriate expansion of the A block monomer density to solve the SCFT equations, which allows the treatment of very complex 3D geometries. The method therefore spans almost the whole range of $\chi_{AB}N$. The only limitation is the computational

1 Introduction

treatable amount of basic functions, which are necessary to describe highly segregated systems. Therefore the calculations are practically limited to $\chi_{AB}N \leq 100$ [Bat99].

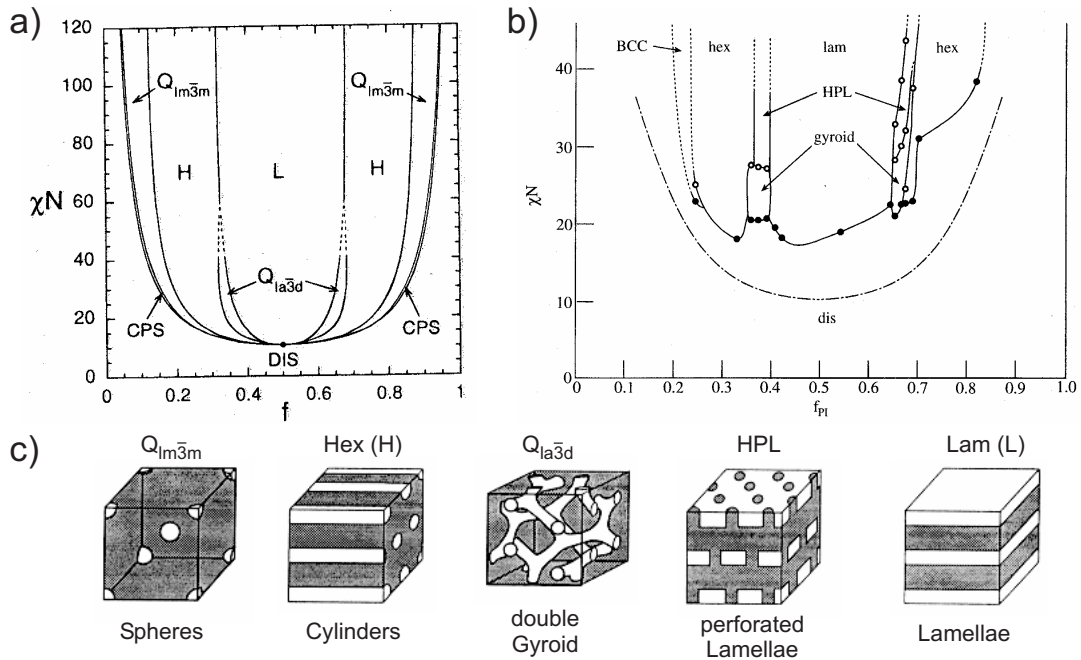


Figure 1.2: Phase diagrams predicted by SCFT calculations [Mat94a] in a) and measured for the system polystyrene-polyisoprene [Kha95] in b). The microdomain structures found are depicted in c). Note that the hexagonally perforated lamella phase (HPL) is not predicted as a stable phase by the SCFT calculations.

Figure 1.2 a) shows the phase diagram calculated with this method in comparison to an experimentally measured phase diagram of polystyrene-*b*-polyisoprene diblock copolymers [Kha95] shown in Figure 1.2 b). In c) the five structures found experimentally are depicted. The SCFT calculations predict ordered phases at sufficiently large $\chi_{AB}N$. The stable phases predicted are a lamellar phase (L), a gyroid phase (G), a phase of hexagonally ordered cylinders (C), a body centered cubic spherical (S) phase, and in a very narrow region a phase of close packed spheres (CPS) with increasing asymmetry of the block copolymer composition. The block copolymer forms structures with an increasing curvature of the interface thereby reducing the elastic energy of the chains.

The experimental diagram has been established by mapping the order-order-transitions (OOT) (open symbols) and the ODT (solid symbols) for ten PI diblock copolymers as the temperature is increased [Kha95]. The lowest line in the

1.1 Block Copolymers

phase diagram represents the mean field result of Leibler [Lei80]. The theoretical results compare rather well to the experimental phase diagram. The sequence of phases is correctly predicted with an exception of the hexagonally perforated lamellar phase, which is only seen in the experiment. In later publications it was first predicted [Mat94a] and later experimentally verified [Qi97, Haj97] that this phase is not thermodynamically stable, but rather a long-lived transient structure with epitaxial relation to the cylindrical and the lamellar phase [Bat99].

Another difference is the asymmetry of the experimental diagram with respect to $f = 1/2$. The reason is the different size of styrene and isoprene monomers and also some asymmetry in their interactions, which cannot be accounted for completely by a single χ_{AB} parameter [Bat99]. The asymmetry of the statistical segment lengths a_A and a_B of the two blocks has been theoretically examined by Matsen and Bates [Mat97a]. They find that the ratio a_A/a_B not only changes the order-order phase boundaries but affects the relative stability of the phases and may even cause the perforated lamellar structure to become an equilibrium phase. Another asymmetry may appear in the respective segment volumes v_A and v_B . Bates and Fredrickson introduced an asymmetry parameter ϵ , which is defined as $\epsilon = (l_A/l_B)^2$, where l_A and l_B are characteristic lengths of the system defined by $l = \frac{a^2}{6v}$ [Bat94]. Olmsted and Milner [Olm98] showed that ϵ influences the phase diagram of strongly segregated systems in a similar fashion as a_A/a_B as described above.

The third discrepancy is the behavior close to the ODT. While the theory predicts all phases to converge to a critical point at $\chi_{AB}N = 10.5$, the experimental diagram shows ODTs only at larger values of $\chi_{AB}N$. As discussed above the SCFT theory of Matsen and Schick is a mean field theory and does not account for compositional fluctuations, which become important near the ODT curve and destabilize ordered structures. Fredrickson and Helfand incorporated fluctuation in the mean field theories and found a shift of the ODT to higher value of $\chi_{AB}N$ indirectly proportional to the degree of polymerization N [Fre87a].

1.1.3 Block Copolymers and Solvents

Solvents play an important role in the preparation of block copolymer samples. A solvent is called a good solvent, if a homopolymer chain effectively swells in solution. If it keeps a gaussian shape the solvent is called theta solvent and if

1 Introduction

it shrinks the solvent is a bad solvent. For block copolymers the solvents can be selective or nonselective, if the solvent prefers one of the blocks or not. In a strict sense a solvent is rarely nonselective, since it typically prefers one of the blocks slightly [Hua98].

We want to restrict our discussion here to nonselective and good or theta solvents, since such solvents are used in this thesis in particular and to prepare block copolymer "equilibrium" structures in general. Solvents have to be used in preparation, if the equilibration of the structure cannot be accomplished by thermal annealing, e.g. because the block copolymer is not stable at the necessary temperatures.

The influence of a nonselective solvent of good or theta quality on the block copolymer behavior is often approximated by the so called "dilution approximation" [Hel72, Lod03]. In this approximation the phase diagram of a block copolymer solution is obtained by rescaling χ_{AB} to $\phi_P \chi_{AB}$, where ϕ_P is the polymer volume fraction or polymer concentration. The accumulation of solvent at the interfaces of the microdomains is neglected [Fre89], as is the existence of a two phase region of a solvent rich and a polymer rich phase. The latter is predicted to be very narrow and therefore of no experimental consequence [Fre89] for nonselective solvents.

The SCFT theory for block copolymer melts has been extended to block copolymer solutions [Hon83, Whi90, Whi92, Hua98]. It has been shown that the dilution approximation is valid for the construction of the phase diagram [Hua98]. As already discussed the SCFT calculations neglect the influence of composition fluctuations, which turn out to be even more important in the presence of solvent.

A series of experiments to study the influence of solvent and the validity of the dilution approximation has been performed in the group of Lodge [Lod95, Han98, Han00, Lod03a]. They show that the dilution approximation is valid for the OOTs but fails to describe the ODT in block copolymer solutions, i.e. the approximation correctly describes the phase diagram except in a range close to the ODT it fails. Dilution expands the domain of stability of the disordered state, since the presence of solvent enhances compositional fluctuations [Lod03a].

The scaling of the domains sizes in solution has been investigated in quite some detail by Hashimoto et al. [Shi83, Mor96, Mor01] and by Lodge et al. [Lod03a] for

1.1 Block Copolymers

a system of polystyrene-*b*-polyisoprene (PI) diluted with nonselective solvents. They find for all ranges of dilution a power law scaling for the microdomain periodicity D as

$$D \sim (\phi_P/T)^\alpha N^\beta. \quad (1.1)$$

In the disordered regime below the GST the exponents are $\alpha_{disorder} = 0$ and $\beta_{disorder} = 1/2$, while for the ordered regime they find $\alpha_{order} = 1/3$ and $\beta_{order} = 2/3$.

Mori et al. [Mor01] also found that $\chi_{eff} \sim (\phi_P/T) N^{1/2}$ consistent with the dilution approximation and therefore $D_{order} \sim (\chi_{eff} N)^{1/3}$ and $D_{disorder} \sim (\chi_{eff} N)^0$.

The concentration scaling of the domain period d depends strongly on the solvent selectivity. For selective solvents values of α may become even negative [Han00].

1.1.4 ABA triblock copolymers

Possibly due to their frequent use in applications, symmetric ABA triblock copolymers have been studied in a remarkable number of publications. Their phase behavior is rather similar to the one of homologous AB diblock copolymers formed by snipping the triblocks in half. A comparison of such an AB diblock and the respective ABA triblock has been performed by Matsen with the help of his SCFT technique [Mat94, Mat95, Mat99]. The resulting phase diagrams for both types of polymers is depicted in Figure 1.3 and shows qualitative similar phase diagrams. Differences in both diagrams can be tracked to the existence of the additional chain ends of the diblock molecules, which decrease the amount of segregation in the system. ABA triblock copolymers therefore order at lower values of $\chi_{AB}N$. The ABA triblock phase diagram is also asymmetric with respect to $f = 0.5$, which has been attributed to the fact that the middle block stretches more easily than the two end blocks. The same reason decreases the stability of the PL phase and increases the domain spacings of the triblock in comparison to the diblock copolymer. Similar results were found in other theoretical studies of Mayes and coworkers [May89, May91] and confirmed by experiments

1 Introduction

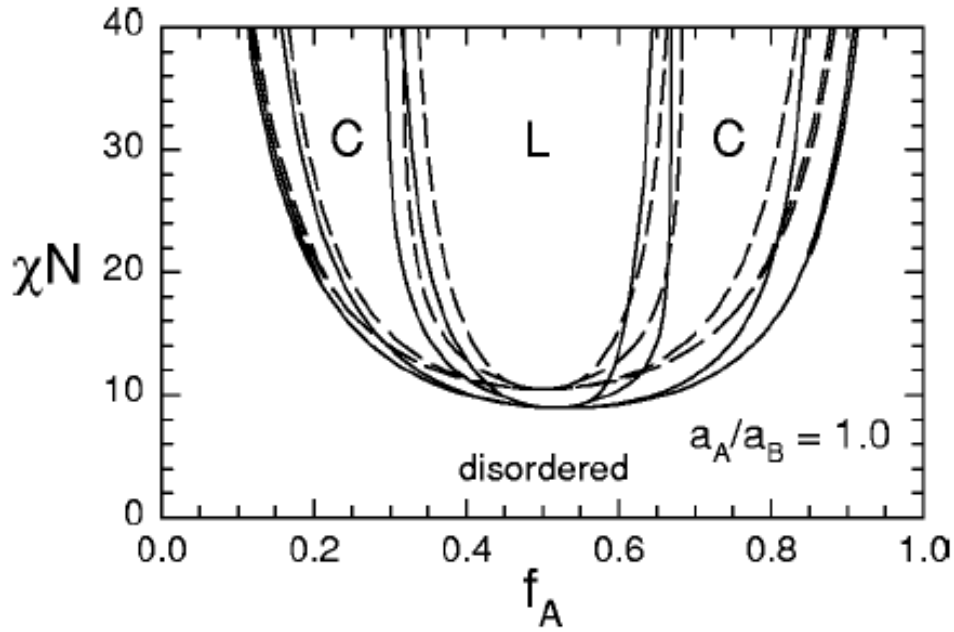


Figure 1.3: ABA triblock copolymer phase diagram (solid lines) overlaid on the AB diblock copolymer phase diagram (dashed lines). Both diagrams were calculated by the SCFT of Matsen [Mat99]. As indicated in the graph, the statistical segment length was assumed to be equal for both blocks ($a_A = a_B$).

[Kob90, Geh92, Ada94, Rii95, Nak96, Ryu97, Kim98b, Mai00, Cha00, Zhu03]. The relative increase of the domain spacing has been found to be close to 10% for intermediately segregated systems and is predicted to decrease at higher segregation [Mai00].

Any asymmetry in the size of the ABA triblock copolymer end blocks reduces the stretching energy of A domains [Mat00], which leads to further increased domain spacings and to a shift of the OOTs to larger volume fractions of the A block f .

1.1.5 Surfaces and Thin Films

The existence of an interface, either a surface (to a gaseous atmosphere) or an interface (e.g. to a substrate), opposes new boundary conditions to the block copolymer system. The interaction of a polymer with the interface is usually described by its interfacial tension γ , which denotes the energetic costs per unit area of creating an interface between the respective environment and the polymer.

1.1 Block Copolymers

In an AB diblock copolymer the interaction of both blocks to an interface has to be described by two interfacial tensions γ_A and γ_B for the blocks A and B, respectively. The difference between both quantities $\gamma_A - \gamma_B$, often referred to as the surface field, quantifies the tendency of one of the blocks to accumulate at the interface, i.e. a lower value of γ_A will lead to a preferential adsorption of the A monomers at the interface. Since the order parameter in a block copolymer system is given by the difference of the local density of one of the blocks from its bulk value, an interface will typically increase the order parameter of the block with the lower interfacial tension at the surface.

There arises a series of consequences from the existence of a surface: In the disordered phase, the connectivity of the chains leads to composition oscillation decaying into the bulk of the material [Fre87, Fos92]. In the ordered state, a lamellar phase will typically align parallel to the interface with the block of lower surface energy covering the interface. A complex reconstruction of the lamellar microdomain structure is induced, if the middle B block of a lamellar forming ABC triblock preferentially wets the interface [Reh01, Reh03]. A similar alignment has also been observed for other bulk structures like cylinders [vD95, Mag97, Kim98, Kim98a] or spheres [Yok00]. Nevertheless in the case of a preferential adsorption of the minority block, these structures cannot satisfy the boundary conditions completely due to their lateral structure. As a consequence phase transitions to other morphologies have been observed [Kar93] and predicted [Tur94]. In the case of a preferential adsorption of the majority block the influence of the interface is less obvious since in principle a surface mainly covered with the majority block is possible. Nevertheless in this case also phase transitions have been predicted, i.e. a transition from hexagonally ordered cylinders to a perforated lamellar structure [Hui00, Hui01].

In a thin film the effect of both surfaces influences the thin film structure. Additional constraints of the commensurability of the film thickness to the dimensions of the preferred microdomain structure in the thin films arise. Let us first consider the case of a commensurate film thickness as it emerges in free standing thin films [Rad96] or in films on supporting substrates [Cou89, vD95, Yok00], where the film may form islands and holes with commensurate local film thicknesses. In the case of lamella forming systems the thin film lamellar spacing corresponds to the bulk lamellar spacing except for weakly segregated systems [Fos92]. For

1 Introduction

cylinder forming systems, if the minority block has the lower surface energy a transformation to a wetting layer (a half lamella) [Kar93] and a lamella [Rad96] have been observed in very thin films. If the majority block is accumulated at the surface, a perforated lamellar phase has been reported in free standing films [Rad96].

If the film thickness is not commensurate to the dimensions of the microdomain structure, other effects come into play. Such a film thickness exists at the steps between islands and holes and if the film cannot relax, i.e. between solid interfaces or if the driving forces for terrace formation are too small. In this case lamellar phases may either stretch their lamellar spacing to fit to the film thickness in the case of strongly preferential surfaces [Lam94] or they orient perpendicular to the plane of the film [Wal94, Kel96] or form mixed phases in the case of two or one weakly preferential interfaces [Fas00, Fas01]. Similarly perpendicular alignment of cylinders has been found and mixed phases like spheres on a perforated lamella [Har98] and cylinders with necks [Kon00]. Various models have been developed [Tur94, Hui00, Hui01, Sev02, Per01, Wan01, Sza03, Fen02, Fen02b, Fen02a] to describe different aspects of the complex phase behavior of cylinder forming block copolymers in thin films. However, it remained unclear, which of the reported phenomena are specific to the particular system and/or route of film preparation and which are general behavior.

The behavior of ABA triblock copolymers in thin films has been studied theoretically [Suh98], by simulations [Sev02, Sza03], and experiments [vD95, Mag97, Har99]. The results are qualitatively similar to the diblock case, but no systematic comparison has been performed.

In this work we establish a detailed analysis of the microdomain structure of thin films of cylinder forming ABA triblock copolymers. A phase diagram of the stable structures as function of the film thickness and polymer concentration is established and the governing parameters are discussed in chapter 5. A detailed analysis of the relevant dimensions of the different stable microdomain structures is presented in chapter 6 and reveals surprising insight into the physics of the thin film system.

1.1.6 Dynamics of Structure Formation in Block Copolymers

Structure formation in bulk block copolymer systems has been studied either by quenching an unordered system to an ordered state thereby inducing a disorder to order transition or by crossing a phase boundary in the phase diagram to induce an order-order transition (OOT). The first set of experiments examines the structure formation out of an unordered state. The samples are typically quenched from a temperature above the order-disorder transition temperature (T_{ODT}) to a temperature below. After a finite incubation time slow nucleation takes place. The resulting grains were shown to be highly anisotropic, extended in the lamellar phase perpendicular to the lamellar direction as revealed by TEM imaging [Has95] but extended along the cylinder direction as concluded from depolarized light scattering experiments [Dai96]. The grains grow rather fast, depending on the depth of the temperature quench until the whole volume is filled by grains [Has98, Dai96]. It has been shown, that there is a optimal quench depth, where the grain growth rate is maximized as a result of the interplay between phase separation driving forces and frictional forces [Kim01a]. The subsequent growth of individual grains on the expense of other grains via defect annihilation was show to be very slow [New98].

Another field of interest are order-order transitions (OOT). In these experiments a non equilibrium morphology is prepared for example in a selective solvent and is then annealed to regain its equilibrium morphology [Sak93, Jeo03]. Another way to induce order-order transitions is to choose a suitable composition of the block copolymer close to a phase boundary in the phase diagram. Annealing at different temperatures or dilution with a nonselective solvent then induces phase transitions [Lod03a, Sak96]. The same effect can be reached by using selective solvents to selectively increase the effective volume fraction of one of the blocks [Han98].

Proposed mechanisms of the structural transitions are the coalescence of the smaller structures to form the more extended structures. Preceding the coalescence is a deformation of the starting structure. The sphere to cylinder transition takes place along the (111) direction of the bcc sphere lattice [Sak96], while cylinders coalesce along their long axis to form a lamellar structure [Sak93]. In both examples the original and final structure were approximately commensurable resulting in a rather fast phase transition. The subsequent ordering of the

1 Introduction

structures was shown to be much slower.

Structure formation in thin films of block copolymers has been studied by equilibrating films for different times. For example, Fukunaga et al. [Fuk03] studied the structure formation in lamellar forming ABC triblock copolymer films with different times of solvent vapor treatment. The authors used SFM and cross sectional transmission electron microscopy (TEM) to study the samples. Since the latter method requires cutting of the film in thin slices, it obviously cannot be applied *in-situ*. Therefore multiple samples with different preparation conditions have to be studied and only statistical conclusions about the general behavior can be drawn. In a similar approach Segalman et al. studied the number of defects and the two dimensional melting in a block copolymer with spherical minority microdomains [Seg01].

In-situ investigations of the structure formation in the same thin film at the same surface area requires a nondestructive method. The scanning force microscope (SFM) is a very well suited tool to establish *in-situ* measurements as long as the microdomain structure is accessible. Nevertheless so far no *in-situ* measurements on thin block copolymer films have been reported in literature. Harrison claims that the phase contrast diminishes at temperatures above the glass transition temperature [Har02]. Therefore, in order to study structural dynamics, the samples are typically repeatedly annealed at elevated temperatures, and imaged at room temperature by SFM [Har00, Har02, Hah98].

In this work we report the first *in-situ* measurements of structure formation and microdomain dynamics in thin block copolymer films. The measurements include the *in-situ* observation of phase transitions in cylinder-forming block copolymers and are presented in chapter 7.

1.2 Overview of Thesis

This thesis is organized as follows:

- Chapter 2 includes the presentation of the model system used in this study and the analytical methods used to characterize the system.
- The processes involved when soft polymeric materials are imaged with tapping mode scanning force microscopy (TM-SFM) are discussed in detail in chapter 3. A way to quantify the indentation of a SFM tip into a soft sample is presented. The procedure enables the reconstruction of a true surface image and a clear assignment of the phase contrast to material properties in our two component system.
- A strong segregation theory (SST) for cylinder forming block copolymers is introduced in chapter 4. The theory is an extension of the advanced SST of Olmsted and Milner [Olm94] to thin films. In particular the principal microdomain spacings of a cylinder forming structure in a thin film is discussed.
- Chapter 5 covers the phase behavior of a cylinder-forming ABA triblock copolymer/chloroform system in thin films. The use of the solvent allows us to tune the interactions governing the system. The stable phases are mapped as a function of film thickness and polymer concentration.
- The principal microdomain spacings of the thin film microdomain structure are investigated in detail in chapter 6 and compared to the SST results presented in chapter 4. A new image analysis algorithm provides the recognition and the localization of the different structures in the SFM phase contrast images. It also allows the determination of local director and, if applicable, the curvature of the microdomain structure. The microdomain spacings are discussed as a function of various parameters like the film thickness, the polymer concentration and the local curvature of the structure.
- In chapter 7 the first *in-situ* observation of phase transitions in thin block copolymer films is presented. The measurements capture the fluctuations

1 Introduction

of the microdomain structure, the nucleation and growth of two new phases and the healing of a phase by defect motion and annihilation.

- A summary of the results presented in this thesis is given in chapter 8.

2 Materials and Methods

2.1 Polymers

2.1.1 Polystyrene-*b*-polybutadiene-*b*-polystyrene (SBS) triblock copolymer

The model block copolymer used in this study is a polystyrene-*b*-polybutadiene-*b*-polystyrene (SBS) triblock copolymer. SBS was obtained from Polymer Source Inc. with molecular weights $M_{w,PS} = 14.0$ kg/mol, $M_{w,PB} = 73.0$ kg/mol, and $M_w = 15.0$ kg/mol (PS is polystyrene, PB is 1,4-polybutadiene). The polydispersity of the polymer is given by the manufacturer as $M_w/M_n = 1.05$.

The bulk behavior of the polymer is determined by the volume fraction f_{PS} of PS and the interaction $\chi_{PS,PB} N$. Taking into account the densities of the homopolymers (1.05 g/cm³ for PS and 0.93 g/cm³ for PB) [Bra89] the volume fraction of PS is $f_{PS} = 0.26$. The degree of polymerization N may be calculated by the molecular weight of the monomers and the molecular weight of the blocks. The result is $N = 1628$.

The interaction parameter of PS-PB block copolymers was studied by several groups [Hew86, Owe89, Sak92, Ada98]. The determination of the $\chi_{PS,PB}$ parameter relies on a comparison of the experimentally found ODT temperature to a theoretically expected one. Note that there are different methods to obtain $\chi_{PS,PB}$, which are not consistent [Mau98]. Here we would like to approximately determine the degree of segregation of our block copolymer and therefore average over the data for $\chi_{PS,PB}$ found in literature.

It should be noted that the interaction parameter depends on the microstructure of the polymers, i.e. the percentage of 1,2 linkage of PB. The temperature applied for the measurements always exceeded 100 °C. The resulting χ parameters agree well for temperatures around 150 °C, so we get a rather large scatter for the χ parameter at 25 °C.

2 Materials and Methods

Owens et al. reported for a SB diblock copolymer with $M_n = 1.86 \cdot 10^4$ g/mol and $f_{PS} = 0.49$ and 95% 1,2 linkage of BP

$$\chi_{S-B} = -0.021 + 25/T. \quad (2.1)$$

Hewel et al. found for a series of SB diblock copolymers with $f_{PS} = 0.3$ and $1.80 \text{ g/mol} \leq M_n \leq \text{unit}[4.00] \text{ g/mol}$ and undefined microstructure

$$\chi_{S-B} = -0.027 + 28/T. \quad (2.2)$$

Sakurai et al. examined commercially available triblock SBS copolymers from Shell, the TR-1102 and the Kraton D-1102. They have a volume fraction of PS of $f_{PS} = 0.31$ and $f_{PS} = 0.28$, 7.4% and 9.8% 1,2 linkage of BP and $M_w = 5.9 \cdot 10^4$ g/mol and $M_w = 5.7 \cdot 10^4$ g/mol, respectively. A neutral and theta solvent dioctyl phthalate (DOP) was added to the polymers with concentrations of the polymer of $\phi_P = 0.61 \dots 1$. Their result is

$$\chi_{S-B} = 6.5910^{-3} + 13.6/T. \quad (2.3)$$

For $T = 25^\circ\text{C}$ averaging yields a value of $\chi_{PS,PB} = 0.061 \pm 0.008$. The total interactions between the blocks is calculated by multiplying $\chi_{PS,PB}$ by the degree of polymerization N in the case of diblock copolymers. For ABA triblock copolymers an intuitive calculation would be $\chi N/2$, since the triblock may be considered as two linked diblocks with degree of polymerization $N/2$.

Calculating $\chi N/2$ at $T = 298 \text{ K}$ yields 51.2, 54.5 and 42.5 for equations 2.1, 2.2 and 2.3, respectively. The average value is 49 ± 6 . Therefore our block copolymer is in the intermediate segregation regime. Dilution with the nonselective solvent chloroform as used in this study should lead to a weaker segregated system according to the "dilution approximation" as discussed in chapter 1.

The phase behavior is also influenced by the asymmetry of the monomers. Although the segment length of the two monomers are almost identical ($b_{PS} = 0.70$; $b_{PB} = 0.65$), there exists a large asymmetry in the monomer volumes

2.2 Characterization

$v_k = M_k/\rho_k$: $v_{PS} = 107.4 \text{ cm}^3/\text{mol}$; $v_{PB} = 58.3 \text{ cm}^3/\text{mol}$.

The polymer is ideally suited for SFM studies, since the two components exhibit a large mechanical contrast and the majority component PB is soft at room temperature. The glass transition temperature of the homopolymer PB is $T_{g,PB} = -83.. - 107^\circ\text{C}$ and the one of PS is $T_{g,PS} = 80..100^\circ\text{C}$ [Bra89]. Since both ends of the copolymer are anchored in glassy domains a pickup of single molecules by the SFM tip is highly unlikely.

The surface tensions to air and the interfacial tensions to the substrate, i.e. SiO_x are important for the thin film behavior of the polymer. The surface tension of PB of $\gamma_{PB} = 31 \text{ mN/m}$ is considerably smaller than the surface tension of PS, $\gamma_{PS} = 41 \text{ mN/m}$ [Sto96]. The interactions of the blocks to the substrate are unknown quantitatively. Harrison et al. [Har98a] found the PB block of PS-PB diblocks covering the native oxide of the SiO_x substrate by SIMS.

2.1.2 Homopolymers

Homopolymers have been used to study the swelling behavior of PS and PB in chloroform. Polystyrene (PS) with and Polybutadiene (PB) homopolymers were obtained from Polymer Standard Service (Mainz, Germany). The PS homopolymer had a molecular weight of $M_{w,PS} = 520 \text{ kg/mol}$ and a polydispersity of $M_w/M_n = 1.03$. The PB homopolymer had a molecular weight of $M_{w,PB} = 47 \text{ kg/mol}$ and a polydispersity of $M_w/M_n = 1.04$.

2.2 Characterization

2.2.1 Scanning Force Microscopy (SFM)

Since its invention in 1986 [Bin86], the SFM has become a very successful and widely used tool to study surfaces in various fields. The success is based on a set of advantages of the SFM in comparison to other high resolution real space imaging methods like scanning electron microscopy (SEM) or transmission electron microscopy (TEM). Two of them are the ease of use, i.e. the easy sample preparation and its applicability in different environments like ultra high vacuum, gaseous atmospheres, or liquids.

A scanning force microscope is build as shown in Figure 2.1. A tip positioned

2 Materials and Methods

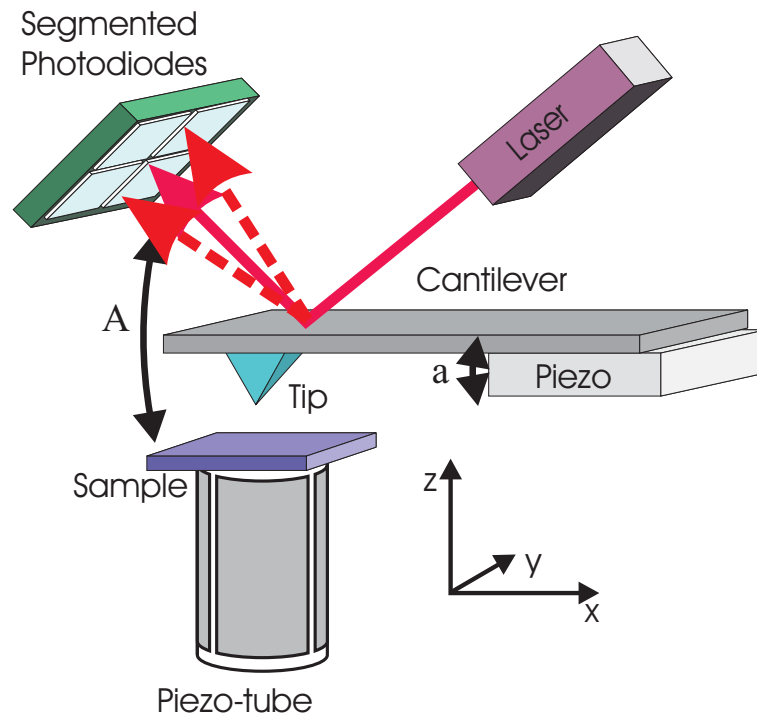


Figure 2.1: Schematic setup of a scanning force microscope. The tip is located at the end of a cantilever. A laser is reflected from the cantilever onto a segmented photodiode. Either the sample (as shown here) or the tip are positioned in 3d space by piezo elements (here a piezo tube). In a dynamic mode of operation the cantilever is excited by a piezo element causing the cantilever to vibrate at an amplitude A .

at the very end of a cantilever is used as probe. A laser is focussed onto the end of the cantilever and reflected into the center of a segmented photo diode. Any forces acting on the tip result in a bending (vertical forces) or twisting (lateral forces) of the cantilever and therefore in a different reflection angle. The difference of the output of the photodiodes is used as output signal, which is in good approximation proportional to the deflection of the cantilever. Depending on the mode of operation the photodiode signal is used directly or in another way as a feedback signal as discussed below. A feedback loop continuously checks the feedback signal, compares it to some user defined setpoint value and adjusts the height of the tip over the sample such that the difference is minimized. Stable operation is possible if the feedback signal is monotonous in the tip-surface distance. The tip is then kept at a height corresponding to a constant interaction over the sample surface.

Either the sample or the cantilever is mounted to piezoelectric elements, which

2.2 Characterization

provide the necessary means to position the tip relative to the sample in three-dimensional space. With the feedback enabled the tip is then scanned relative to the sample surface and the height adjustments to keep the feedback value at its setpoint are recorded as an height image of the surface.

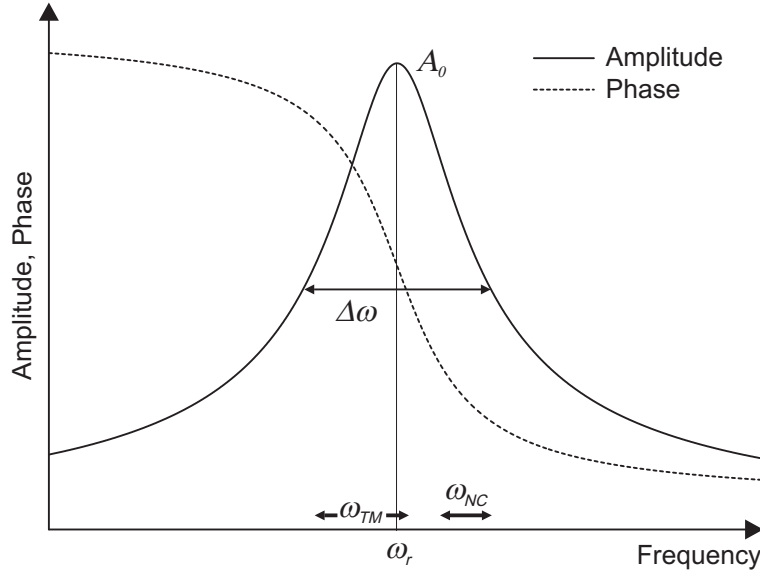


Figure 2.2: Resonance curve of a harmonic oscillator representing the excited cantilever system. The resonance frequency is ω_r and the width of the resonance curve is $\Delta\omega$. The arrows at the bottom of the curves denote the ranges of the typical excitation frequencies for the tapping mode (ω_{TM}) and the noncontact mode (ω_{NC}).

A variety of modes have been established depending on the environment of scanning and the source of forces acting on the tip. To simply measure topographic information, the early used contact mode is more and more replaced by dynamic modes. In the latter the tip is forced to oscillate close to its resonance frequency excited by an additional piezo element positioned at the base of the cantilever. The oscillation is monitored by the photodiodes and converted to an amplitude and a phase signal. A typical resonance curve is shown in Figure 2.2. The phase signal measures the phase difference between the detected cantilever vibration and the exciting oscillation and scales between 0 and $-\pi$.

If the tip experiences any kind of forces from the sample surface, the resonance curves of the tip sample system deviate characteristically from the resonance curve of the tip only. Elastic interactions cause the resonance frequency of the tip-sample system to either decrease or increase in the case of attractive or repulsive

2 Materials and Methods

forces. Dissipative interactions decrease the energy in the system and therefore the amplitude of oscillation. See also chapter 3 for details.

Two modes of operation have found widespread use. The first one is the so called "dynamic mode", which uses the shift of the resonance frequency as feedback parameter. This mode is best suited for ultra high vacuum application, since in this environment the resonance curve is very small (quality factor $Q_{UHV} = \omega_r/\Delta\omega \approx 20000$) and the resonance frequency shift is larger than the width of the resonance curve. In ambient conditions the presence of air decreases the quality factor to $Q_{ambient} \approx 400$, Therefore either the "tapping mode" (also called "intermittent contact" mode) or the "noncontact mode" are typically used. These modes use the amplitude signal as feedback signal, which normally decreases monotonous with the tip sample distance. One major obstacle in scanning in ambient conditions is the adhesion force between the tip and the sample, which is much larger than in liquid or in vacuum environments due to an absorbed water layer on tip and sample surfaces. Therefore rather stiff cantilevers (spring constants ≈ 40 N/m) and large vibration amplitudes (10-80 nm) are used, such that the restoring force at maximum amplitude exceeds the adhesion force. Only under these conditions a stable operation is possible. Depending on the setpoint amplitude the forces between the tip and the sample are attractive or repulsive. The noncontact mode operates at very large amplitudes setpoints only slightly below the free amplitude of the tip and at frequencies larger than the resonance frequency in order to establish scanning with only attractive forces between tip and sample. This mode has the advantage of being the least destructive of the two modes. The tapping mode or intermittent contact mode uses lower setpoints at which repulsive forces due to tip sample indentation come into play. Only in this case the phase signal exhibits material contrast. Another advantage to the noncontact mode is the fact that the amplitude distance dependence is steeper at lower setpoints, which in turn enables faster scanning of the sample surface.

2.2.2 Ellipsometry

Ellipsometry has been used to measure the thickness of homopolymer and block copolymer films. Ellipsometry uses the change in polarization of light, which has been reflected from a surface covered by a thin film. To this extend the sample is illuminated with circular polarized light and the ellipticity of the reflected light

2.2 Characterization

is analyzed.

As a result one obtains the two ellipsometric angles, Ψ and Δ . Ψ is related to the reflectivities r_P and r_S of the reflected light, where the index denotes parallel (P) or perpendicular (S) polarized light, as

$$\tan(\Psi) = r_P/r_S, \quad (2.4)$$

while Δ is related to the change in phase $\Delta\phi_P$ and $\Delta\phi_S$ as

$$\Delta = \Delta\phi_P - \Delta\phi_S. \quad (2.5)$$

In the case of a spectroscopic Ellipsometer as the used SENTECH SE 850, both angles are measured over a range of wavelength in the visible or near infrared spectrum. Details to this instrument are given in ref. [Elb01].

In this work a spectral range of 400 to 800 nm was used. In order to extract physical quantities from the Ψ and Δ curves one has to know some details about the sequence of layers of the system under study. For each of the layers one further has to assume a model for the wavelength dependence of the refractive index and of the absorption index for the respective material. The software "Advanced Fit" supplied with the instruments then solves the Fresnel equations for all wavelengths and tries to least square fit the data with an iterative algorithm.

Models for silicon, silicon oxide and air are supplied with the instruments. Therefore one measures the clean substrates with a silicon oxide layer between air and silicon with the thickness of the silicon oxide layer as fit parameter. Then polymeric films on substrates of the same wafers are measured. The model used for the polymeric layer is the so called "cauchy model", which assumes the following wavelength dependence of the refractive index,

$$n(\lambda) = n_0 + n_1 \frac{100}{(\lambda/nm)^2} + n_2 \frac{10^7}{(\lambda/nm)^4} \quad (2.6)$$

The absorption of the polymeric layers is assumed to be negligible and is set to zero. The remaining fit parameters are the thickness d_P and the coefficients

2 Materials and Methods

for the refractive index n_0 , n_1 and n_2 . The results of the fit procedure resulted typically in very good fits of the Ψ and Δ curves measured for the system.

In situ measurements of solvent swollen films could also be fitted very well with a simple cauchy layer assumed for the polymer/solvent film (see also chapter 5). This in turn either means that ellipsometry is not well suited to measure inhomogeneities of the solvent distribution in our systems or that the solvent is distributed rather homogeneously throughout the film.

The least square error of the fit became larger if the samples formed islands or dewetted during the sample preparation (for details see [Lip03]). Ellipsometry can therefore be used to monitor the preparation process. One can not only directly measure the amount of solvent in the film but also stop the measurement if the samples start to dewet.

2.2.3 Small Angle X-ray Scattering (SAXS)

Synchrotron SAXS has been used to investigate the bulk microdomain structure of the SBS/chloroform system. It is able to measure periodic structures in the range of 2 to 200 nm and is therefore ideally suited to investigate the mesoscale microdomain structure of block copolymers.

X-Ray radiation is scattered from the electrons in the system. The scattered x-rays interfere constructively, if Bragg's law is fulfilled,

$$n \lambda = 2 d^* \sin(\Theta), \quad (2.7)$$

where n is the order of the reflection, λ is the wavelength of the x-rays, d^* is an characteristic, periodic distance of scattering planes in the sample and Θ is the angle of reflection.

In a typical SAXS experiment the intensity of the x-rays is measured as a function of the scattering vector q , which quantifies the momentum change of the scattered x-rays perpendicular to the beam. According to Bragg's law a SAXS spectrum shows intensity maxima at first and higher order peaks appear

at scattering vectors of

$$q = \frac{2\pi n}{d^*}. \quad (2.8)$$

The principal spacing of lattice planes is usually extracted using equation 2.8 for the first order peak of the spectrum. The sequence and position of the peaks relative to the first order peak allows the identification of the symmetry of the system. Block copolymers consisting of two blocks form only a limited number of microdomain structures, namely lamellae, a gyroid structure, hexagonally ordered cylinders and close packed or body centered cubic packed spheres. Since the symmetry is different in all available structures, it is very easy to identify the bulk microdomain structure of such a system. For example the structure consisting of hexagonally ordered cylinders shows higher order peaks typical for the structure at $\sqrt{3}q_0$, $\sqrt{7}q_0$, $\sqrt{9}q_0$, where q_0 is the scattering vector of the primary peak.

The SAXS data shown in this thesis were acquired at the synchrotron-SAXS beamline ID02A at the European Synchrotron Radiation Facility (ESRF) in Grenoble, France. Details on the beam line can be found in [Boe02]. The energy of the x-ray photons is set at 12.5 keV, which corresponds to a wavelength of 0.1 nm. This is a rather large energy compared to typical SAXS energies used in the lab and results in rather small scattering angles, which are compensated by a large distance of the detector from the sample of 10 m. On the other hand this energy is larger than the K-absorption peak of chlorine at 2.8 keV and therefore very well suited for measurements on our SBS/chloroform system.

2.2.4 Optical Microscopy

Optical microscopy (OM) reaches a resolution of $\approx 1\ \mu\text{m}$ in lateral direction. If a thin polymeric film on a reflective substrate is illuminated by a white light source, the light reflected at the substrate and at the film surface interferes, which results in characteristic colors of the reflected light. The color depends on the film thickness and the refractive index of the thin film. Thickness changes of a few nm are enough to result in a visible color contrast, which makes OM a very useful tool to detect changes in the local film thickness with a lateral resolution

2 Materials and Methods

of μm .

This feature has been used in this work to investigate the formation of islands and holes in thin block copolymer films during preparation (see chapter 5). The instrument is a Axiotech OM from Zeiss combined with a digital camera with a resolution of 752×582 pixels. Depending on the chosen magnification of $100\times$, $200\times$ or $500\times$, a frame captured by the digital camera is 1 mm, $500 \mu\text{m}$ or $200 \mu\text{m}$ wide.

3 Tapping Mode Scanning Force Microscopy on Polymers: Where Is the True Sample Surface? ¹

We investigate in detail the processes involved when soft polymeric materials are imaged with tapping mode scanning force microscopy (TM-SFM). Measuring lateral arrays of amplitude/phase vs. distance (APD) curves, we are able to determine quantitatively the amount of tip indentation and reconstruct the shape of the “real” surface of the sample. Moreover, contrast inversion in height and tapping mode phase images is explained on the basis of attractive and repulsive contributions to the tip-sample interaction. The experiments are performed on surfaces of poly(styrene-*block*-butadiene-*block*-styrene) (SBS) triblock copolymers acting as a model system.

¹The results of this chapter have been published in: *Macromolecules* [Kno01]

3 Where Is the True Sample Surface?

3.1 Introduction

Tapping mode scanning force microscopy (TM-SFM) [Bin86, Zho93, Qui94] has been established in recent years as a standard tool to investigate surfaces of soft materials. Its excellent lateral resolution together with its potential to distinguish different materials without further staining has made TM-SFM an attractive alternative to established techniques such as transmission electron microscopy. Despite its widespread use, however, the complex dependence of TM-SFM images on the imaging parameters [Mag97] gives rise to the notion that the results may be subject to various uncontrolled artifacts and raises the question whether and how reproducible imaging conditions can be established. Typical problems occurring when TM-SFM is applied to polymeric samples concern the quantitative reproducibility of height and phase images, the distinction between real surface topography and indentation [Höp95], and even the frequently occurring contrast inversion of height and phase images [Mag97, Pic98, Spa97, Küh98]. In the present work, we apply TM-SFM to a typical heterogeneous block copolymer surface. Recent theoretical [Tur94, Mat97, Hui00] and experimental work [Sto96, Kon00, Kon96, Mor97] has shown that the near-surface microdomain structure of block copolymers can differ significantly from the bulk situation. As a model material, we use a commercial poly(styrene-*block*-butadiene-*block*-styrene) (SBS) triblock copolymer. We present a simple means to distinguish between tip indentation and real surface topography and describe in detail the dependence of the resulting height and phase images on the imaging parameters.

In tapping mode (ref [Zho93]), the AFM cantilever is excited to a mechanical oscillation near its resonance frequency. Typical amplitudes A_0 at the tip side of the freely oscillating cantilever are some 10 nm. With typical spring constants of the cantilever of about 50 N/m, adhesive forces can be overcome, and an almost free oscillation of the cantilever is realized with the tip touching the surface only during a small fraction of each oscillation period. In consequence, lateral forces are minimized, and damage of the specimen is largely avoided with hardly any loss in lateral resolution. The interaction of the tip with the surface leads to a change of the amplitude A of the oscillation. The latter is detected and kept at a constant value (referred to as *set point* A/A_0) through a feedback mechanism continuously adjusting the distance between the cantilever and the surface under study. Changes in the position of the sample (or the cantilever) needed to keep a

3.1 Introduction

constant amplitude of oscillation are monitored and displayed as what is typically called a *topography* or *height image* of the surface.

In addition, the phase difference between the free end of the cantilever and the driving piezo element can be measured as well. The resulting *phase images* are discussed quite extensively in the recent literature [Gar98, Win96, Tam97, Non99, Wha98, Wan99]. Following a suggestion by Cleveland et al. [Cle98], the phase shift can be related to the power dissipated by the sample during the mechanical contact with the tip. It is generally accepted that the phase signal to some extent reflects the viscoelastic properties of the sample [Gar98]. It is therefore often used to qualitatively distinguish different materials on the surfaces of heterogeneous samples. Quantitative information about materials constants, however, can hardly be extracted from phase images at present.

One reason for this deficiency is the fact that the time of contact between tip and sample is increasing with decreasing *set point* [Gar98]. Therefore, the choice of the *set point* affects both the relative phase and the relative height signal on a heterogeneous sample. Under certain conditions, an inversion of the phase and height contrast can occur as the *set point* is changed. One way to quantitatively examine this dependence is to determine the amplitude and phase signals as a function of the distance between cantilever and sample (referred to as “APD curves”). Chen et al. [Che98, Beh99] measured APD curves on gelatin, polystyrene, and mica samples and compared the respective results. The authors discussed height artifacts and phase contrast reversal on the basis of single APD curves measured on the different materials. Bar et al. [Bar00] examined in this way polybutadiene/ polystyrene-*co*-polybutadiene rubber blends.

In the present paper, we extend this work by determining APD curves as a function of the lateral position on a block copolymer surface exhibiting lateral heterogeneities on the 10 nm scale. Thereby we can compare the information contained in the APD curves directly to conventional TM-SFM images taken at the same spot of the sample. Furthermore, information about the surface can be extracted from the APD curves without the influence of the tapping conditions, and possible artifacts on the height image can be discussed. The indentation of the tip into the sample is determined quantitatively from the APD curves, and a model of the volume composition near the block copolymer surface can be estimated.

3 Where Is the True Sample Surface?

3.2 Experimental Section

All measurements were performed under ambient conditions using a commercial scanning probe microscope (Digital Instruments NanoScope Dimension 3100). A *single* silicon cantilever (NANOSENSORS, typical spring constant: 40 N/m) was used for all measurements in order to avoid possible artifacts due to differences in tip shape or spring constant. The parameters of the cantilever oscillation were determined by fitting a simple harmonic oscillator model to the amplitude vs frequency curves measured at a distance of about 100 nm above the sample surface. This distance is controlled by disabling the feedback loop of the instrument being in light tapping and subsequently retracting the tip and performing the frequency sweep. The resonance frequency and the quality factor of the cantilever were determined to 336.0 kHz and 365, respectively. It is worth mentioning that these values differ significantly at larger distances from the surface (336.4 kHz and 460, respectively, at 1 mm).

Quantitative measurements with TM-SFM rely upon a good calibration of the cantilever amplitude to the photodiode signal. In this work we used a procedure suggested by Nony et al. [Non99]: A series of APD curves are measured on the sample for different drive amplitudes of the piezo element exciting the cantilever oscillation, and the root-mean-square (rms) value P_{rms} of the photodiode signal is monitored. For each curve one determines the absolute position z_0 of the piezo element adjusting the cantilever sample distance when the tip first touches the sample (see below). The calibration factor is determined from the slope of the z_0 vs P_{rms} curve. Another way of calibrating the amplitude is measuring the decrease of the amplitude while approaching a hard surface (e.g., silicon). Both procedures resulted in a calibration factor of 23.7 ± 0.3 nm/V.

In the instrument used in this work the phase signal is generated by multiplying the normalized cantilever excitation signal with the normalized photodiode signal. This signal is closely related to the physical phase of the oscillation but has a value of zero at the resonance frequency of the cantilever. In this work we used this signal without any transformations as a measure of the physical phase.

Poly(styrene-*block*-butadiene-*block*-styrene) (SBS) was obtained from Polymer Source Inc. The PS, PB, and PS blocks had weight-averaged molecular weights of 14 kg/mol, 73 kg/mol, and 15 kg/mol, respectively, and a polydispersity of 1.02. In bulk the PS blocks self-organize into cylinders of about 25 nm diameter

3.3 Results and Discussion

embedded within a PB matrix. Viewed along their long axes the cylinders form a hexagonal lattice with a mean distance of 45 nm between two next-nearest cylinders. An SBS film was prepared on a polished silicon wafer by spin-casting (2000 rpm) from a 2 wt % toluene solution, which results in a film thickness of about 100 nm. For equilibration and long-range ordering of the SBS microdomain structure the sample was exposed to chloroform vapor [Kim98, Kim98a]. The vapor pressure was reduced from about 80 % of saturation to zero over 1 day. This procedure results reproducibly in films of about the same thickness with cylinders oriented parallel to the plane of the film.

The Nanoscope III software supplied with the instrument provides a means to measure an array of amplitude/phase distance (APD) curves. In the present work an array of 30×30 curves with a lateral separation of 4 nm was measured within a total time of some 8 min. The resulting 900 curves were analyzed with home-built software (see below).

3.3 Results and Discussion

Figure 3.1 shows the typical behavior of amplitude (a) and phase (b) of the cantilever oscillation, when the tip approaches the surface. In this study only approach curves are used. At larger distances between tip and sample ($z > z_0$ in Figure 3.1 a,b), both amplitude and phase are constant, indicating that in this regime the forces acting on the cantilever are negligible or distance independent. At a certain point z_0 the phase signal exhibits a kink and turns to negative values. At about the same z-position the amplitude starts to decrease. On further approach the amplitude signal continues to decrease while the phase signal eventually starts to increase.

This behavior can be explained with a model accounting for the additional forces introduced by the tip-sample interaction [Wha98, Wan99, Wan98]. Within this model it is assumed that these forces are weak and can be considered as a perturbation of the mechanically oscillating system. In this case additional attractive (repulsive) conservative forces result in an decrease (increase) of the force constant of the oscillator, which in turn leads to a negative (positive) shift $\Delta\varphi$ of the resonance frequency of the tip-sample system. In addition, energy dissipation into the sample will result in an increased damping of the system, i.e.,

3 Where Is the True Sample Surface?

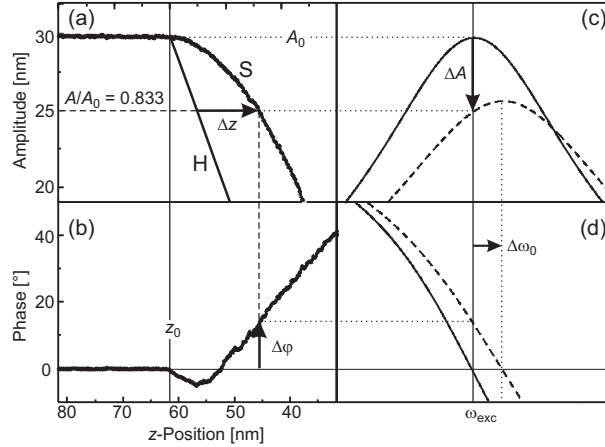


Figure 3.1: Typical amplitude vs. distance (a) and phase vs. distance curve (b) measured on the SBS sample. The straight line H represents an infinitely hard surface. Dashed lines indicate how indentation Δz and phase shift $\Delta\varphi$ are determined for a given *set point* A/A_0 . (c, d) Cantilever amplitude and phase as a function of excitation frequency measured for the free oscillation (solid line) and for a cantilever in repulsive contact with the sample corresponding to a *set point* $A/A_0 = 0.833$ (dashed line) calculated based on a harmonic oscillator model. In contact the resonance frequency is shifted by $\Delta\omega_0$, and the quality factor is reduced, resulting in an amplitude reduction ΔA and a phase shift $\Delta\varphi$ at the excitation frequency ω_{exc} .

in a decrease of the quality factor. In Figure 3.1 c,d the amplitude and phase behavior for the free cantilever (solid lines) is shown together with a model resonance curve (dotted lines) of a harmonic oscillator assuming a positive shift of the resonance frequency and an increased damping. The latter serves as a model for a cantilever in (repulsive) contact with the sample. For a given *set point* the change of the resonance curve affects both amplitude and phase values at the excitation frequency ω_{exc} . In our experiment, the cantilever was excited (ω_{exc}) at its resonance frequency ω_0 . The figure demonstrates how a net repulsive, dissipative force leads to a decrease of the amplitude ΔA and an increase of the phase value $\Delta\varphi$ at the excitation frequency ω_{exc} . The dotted curves correspond to a *set point* $A/A_0 = 0.833$, i.e., a cantilever amplitude $A = 25$ nm. It becomes clear from the figure that the sign of the phase shift $\Delta\varphi$ indicates whether attractive or repulsive forces govern the tip sample interaction.

Returning to the experimental APD curves displayed in Figure 3.1 a, we can identify the initial decrease of the phase values as the result of attractive forces between tip and sample. Attractive forces are expected to result from long-range

3.3 Results and Discussion

van der Waals interactions [Tam97, Boi98, Non99] and adhesive contributions including capillary forces [Lun98]. The increase of the phase signal at smaller tip-sample distances can be attributed to increasing repulsive forces due to the indentation of the tip into the sample.

One major problem in TM-SFM on soft materials is the distinction between the real surface topography and an apparent one due to lateral variations of the indentation depth of the tip [Höp95]. One therefore faces the problem to define at which z -position the tip touches the surface. In the present work we chose the initial kink in the phase signal as this point z_0 in all APD curves [Dor99].² This choice seems reasonable assuming that long-range attractive forces are independent of the lateral position of the tip. This assumption seems justified on our particular sample, since van der Waals forces will be similar for the two components of the block copolymer under study. Therefore, we may at worst introduce a systematic error at this point, which does not effect the general conclusions drawn in the following discussion.

When the tip touches the surface, i.e., around $z = z_0$, the amplitude signal shows a much weaker effect than the phase signal. The rather soft sample allows the tip to indent the surface, which results in a smoothly varying amplitude signal. If the sample would be infinitely hard, the amplitude of the cantilever oscillation would decrease linearly as the cantilever base is getting closer to the surface. This behavior is indicated by the straight line H in Figure 3.1 a). At any given *set point* A/A_0 , the indentation Δz of the tip is given [Höp95] by the difference in z when the amplitude reaches the *set point* value on the soft sample (S) and the ideally hard surface (H) (horizontal arrow in Figure 3.1 a). We note that this measurement of the indentation relies on two assumptions. Since only the rms value of the oscillation is measured, one has to assume that the oscillation of the cantilever remains harmonic even when it is in contact with the sample surface. This assumption has been found to be valid on soft samples [Cle98, Del00]. Second, the average deflection of the cantilever has to be zero. This can be measured by monitoring the dc offset of the photodiode signal, and

²Different procedures can be used to determine z_0 . We find that the most reliable way is to determine first for large distances the mean phase $\langle \varphi \rangle$ and the corresponding standard deviation σ and then to take as z_0 the largest distance z of a phase vs distance curve at which $\varphi(z)$ deviates more than 2σ from $\langle \varphi \rangle$. This introduces a systematic offset in the order of 0.3 nm and a mean error for z_0 of about one z -step (0.12 nm) of the measured $\varphi(z)$ curve.

3 Where Is the True Sample Surface?

it was found that the signal is negligible in the measured z range.

On the basis of the above considerations, we are now able to determine the shape $z_0(x, y)$ of the physical surface of our block copolymer sample and to quantitatively determine lateral maps of tip indentation $\Delta z(x, y)$ for any given *set point*. A 30×30 array of APD curves was measured on an SBS sample. This procedure enables us to directly compare surface morphology and indentation maps to the common height images obtained in a standard TM-SFM experiment performed at the same spot of the sample. In addition, images of the phase shifts can be reconstructed from the APD curves and compared to TM-SFM phase images.

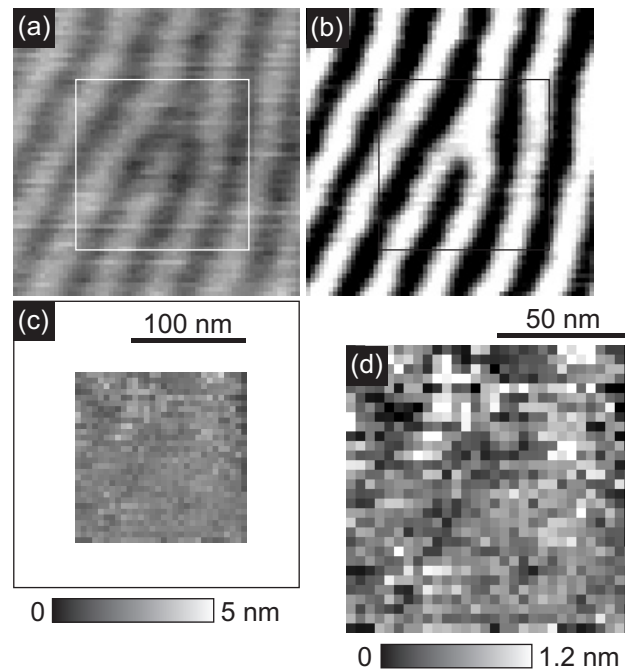


Figure 3.2: Height images measured with conventional TM-SFM ($A_0 = 30$ nm at *set points* $A/A_0 = 0.99$ (a) and 0.70 (b)). (c, d) “Real surface topography” z_0 of the area indicated by the box in (a) reconstructed from the APD curves. In (a), (b), and (c) the same height scale has been chosen (0-5 nm), while in (d) the height scale is blown up to 0-1.2 nm.

We start with the reconstruction of the surface topography $z_0(x, y)$ from the absolute z -positions of the z -piezo element when the cantilever comes into contact with the sample. Figure 3.2 shows a comparison of conventional TM-SFM height images taken at *set points* $A/A_0 = 0.99$ (a) and 0.70 (b). In addition, we show the surface topography $z_0(x, y)$ of the same spot of the sample reconstructed from

3.3 Results and Discussion

APD curves in the same height scale (0-5 nm) (Figure 3.2 c). Figure 3.2d shows the same data with the height scale blown up to 0-1.2 nm. The TM-SFM height images show a stripelike pattern at both *set points*, indicative of a regular hill and valley morphology on the surface. Dependent on the *set point* value, however, the height contrast is inverted; i.e., hills observed at $A/A_0 = 0.99$ turn into valleys at $A/A_0 = 0.70$ and vice versa. The reconstruction of the surface topography from the APD curves (Figure 3.2 c) indicates that the polymer surface is essentially flat with a surface roughness less than 1 nm. As can be seen from Figure 3.2d, the surface roughness (fwhm of z_0 histogram = 0.6 nm) is of the order of the uncertainty of the z_0 determination.

Using the procedure described above for calculating indentation and phase values for a given *set point*, one can calculate indentation and phase images. To compare these pictures to regular TM-SFM images, a set of TM-SFM images was taken with the same tip at the same spot of the sample using *set points* between $A/A_0 = 0.99$ and 0.50. At *set points* smaller than 0.50 the imaging conditions became unstable, resulting in distorted TM-SFM images. A comparison between the conventional TM-SFM images and the images reconstructed from the APD array is shown in Figure 3.3. In the left part the indentation maps (a) are compared to the TM-SFM height images (b) at the respective *set point* values. Note that the indentation scale is an absolute scale while the height scale in TM-SFM is only a relative measurement. Therefore, only the difference of maximum and minimum values in the scales can be chosen equal. In the right-hand part of Figure 3.3, the phase images obtained from the APD curves (c) are compared to the conventional TM-SFM phase images (d). The scales of the images are the same for the corresponding *set points*; therefore, only a single scale bar is shown. It can be seen that the indentation maps and the phase images based on the APD curves correspond very well to the respective TM-SFM height and phase images. The striking result of this comparison is the observation that, for the particular sample under study, the conventional TM-SFM “height images” merely reflect lateral differences in tip indentation depth on a virtually flat sample. They are not related to the real surface topography. In general, TM-SFM height images will be determined by an interplay between real surface topography and indentation. The procedure described above is able to distinguish and to determine quantitatively the two contributions.

3 Where Is the True Sample Surface?

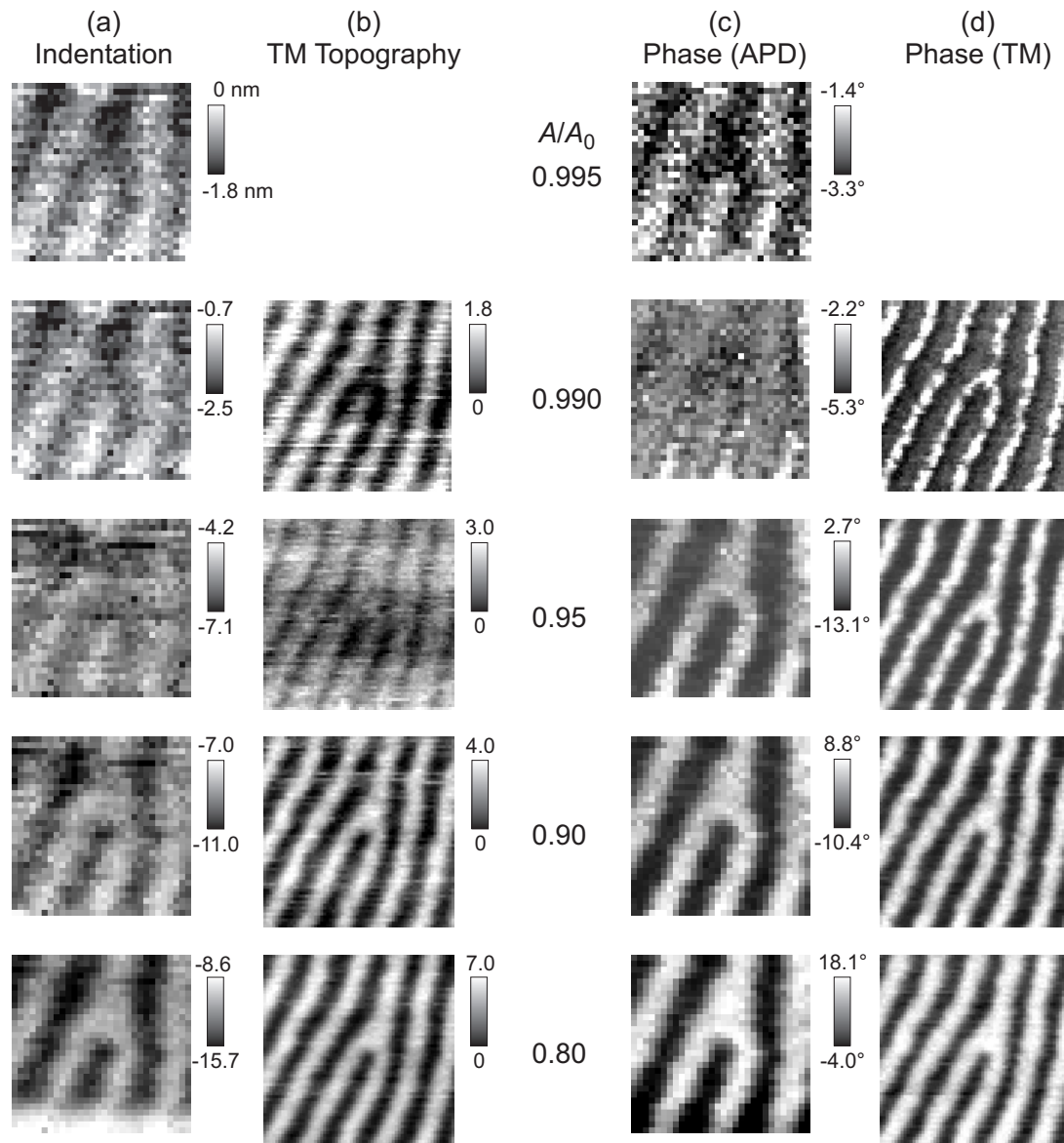


Figure 3.3: Comparison of indentation (a) and phase signal (c) determined from APD curves (imaged area = $120 \times 120 \text{ nm}^2$) with the respective TM-SFM height (b) and phase (d) images ($250 \times 250 \text{ nm}^2$) taken at different *set points* A/A_0 ranging from 0.995 to 0.80 ($A_0 = 30 \text{ nm}$). Note that only the central part of the area imaged by conventional TM-SFM (b, d) is reconstructed from the APD curves (a, c).

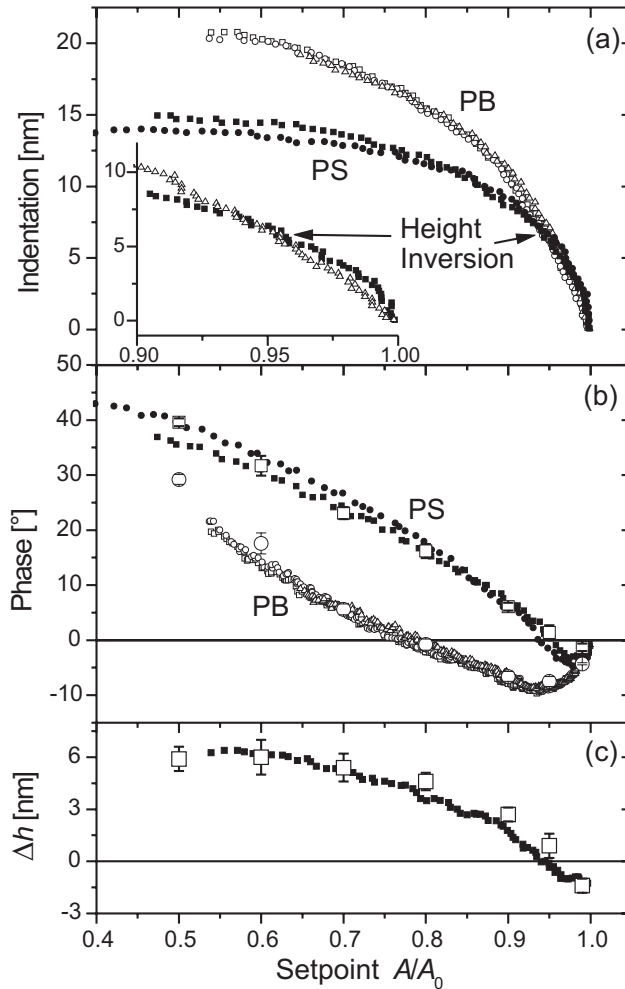


Figure 3.4: Indentation (a) and phase signal (b) vs *set point* A/A_0 taken in the center of PS- and PB-rich areas ($A_0 = 30$ nm). The crossing of the indentation signals at $A/A_0 = 0.95$ indicates the height inversion in a TM-SFM experiment. In (b) the large open symbols and error bars represent average values extracted from 10 scan lines taken from the TM-SFM height and phase images. (c) Height difference δh (open symbols) between PS- and PB-rich areas in TM-SFM height images and differences in indentation (closed symbols) between PS and PB-rich areas determined from APD data shown in (a).

3 Where Is the True Sample Surface?

The absolute amount of indentation is surprisingly high, taking into account the free amplitude $A_0 = 30$ nm. To further elucidate this point, Figure 3.4 shows another plot of the indentation depth and the phase shift as a function of the *set point* for five APD curves taken at different lateral positions showing very high and very low absolute indentations. Given the different rheological properties of PS and PB at room temperature, we identify the regions of high indentation with PB-rich microdomains located near the surface, while the smaller indentation is expected in the vicinity of PS-rich microdomains. Together with the APD data, we show amplitude and phase values taken from TM-SFM images in the following way: The open symbols were obtained as average maxima and minima of 10 scan lines taken perpendicular to the direction of the stripes. The error bars represent the standard deviations of these values. Since only height differences Δh are measured in TM-SFM (see Figure 3.4 c) the difference in indentation (determined from the average of the respective curves shown in Figure 3.4 a) is shown for comparison. Figure 3.4 b,c shows that the data obtained with both methods agree quantitatively in the measured regime. On the softer parts of the sample the indentation reaches values as high as 20 nm. This corresponds to 66% of the free cantilever amplitude A at a *set point* A/A_0 of about 0.5, which in turn relates to a cantilever amplitude A of about 15 nm. This finding implies that the tip is in contact with the sample more than half of its oscillation period.

As expected, the indentation increases with decreasing *set point*. On the harder parts of the surface the indentation levels off at about 15 nm. Interestingly, at high *set points* the increase of indentation with decreasing *set point* is faster on the harder parts as compared to the softer parts of the sample. Consequently, the indentation curves cross at a *set point* A/A_0 of about 0.95. In the TM height images this behavior appears as an inversion of the height contrast between the two materials (see Figure 3.2 a,b). As a possible physical explanation of this effect, one needs to consider the fact that PB is liquid at room temperature and therefore is expected to strongly adhere to the tip. This adhesion will effectively damp the cantilever oscillation leading to the observed steep decrease in amplitude as the tip approaches the sample. At lower *set points* repulsive contributions will eventually dominate, and the harder material (PS) will show larger decrease in amplitude (i.e., smaller indentation).

The phase signal at lower *set points* rises much faster on the harder (PS-

3.3 Results and Discussion

rich) phase. In TM-SFM this typically results in a phase contrast with the polystyrene part appearing brighter. In this regime the repulsive forces between the tip and the sample dominate. It has been stated that the difference in the phase signal cannot be explained by simply assuming different material constants of the constituent materials [Gar98]. This, however, is true only if damping is neglected. If the damping constant of both materials happens to be similar, the harder material will shift the phase to higher values because it introduces the higher additive force constant to the system. In this particular experiment no phase inversion could be detected in the TM-SFM images. The APD curves display a phase inversion at very high *set points*, where stable TM-SFM imaging was hardly possible. This phase inversion in the purely attractive regime could again result from a higher adhesion hysteresis of the butadiene phase.

At this point we like to report on the reproducibility of our results. Comparable experiments with different tips and different free amplitudes between 20 and 40 nm have been done. The behavior of indentation, height, and phase vs *set point* A/A_0 (as shown in Figures 3.2, 3.3, and 3.4) is very reproducible as long as “fresh and clean” tips from the same tip wafer are used on identically prepared SBS samples. In these cases and within the *set point* range 0.5-0.95 indentation increases systematically with increasing free amplitude A_0 and decreasing *set point* A/A_0 . For PS, *set point* $A/A_0 = 0.75$, and free amplitude A_0 between 20 and 40 nm, for example, indentation varies (almost linear) between 7 and 18 nm. Variations from tip to tip are in the range of $\pm 10\%$. For *set points* close to 1.0 reproducibility is limited by the amplitude noise. Similar holds for the phase vs *set point* curves. For PS for instance, the minimum value of the phase varies by $\pm 10\%$ and is always reached within the *set point* range of 0.99 and 0.96. AFM tips get “dirty” or dull after some time of scanning. This happens more frequently when high scan speeds are used or when hard surfaces such as Si are scanned with *set points* < 0.5 . In these cases we observe that indentation is considerably reduced. Also, the contrast in conventional TM-SFM phase images is drastically reduced (if not lost), and phase vs distance curves change considerably while keeping qualitatively their shape. Apparently, indentation and phase vs *set point* curves depend critically on tip shape. However, their quantitative description with a detailed model including tip shape, elasticity of the sample, etc., is beyond the scope of this paper. Nevertheless, we like to stress that for the quantitative

3 Where Is the True Sample Surface?

determination of the “true surface shape” $z_0(x, y)$ and indentation in conventional TM-SFM experiments such a detailed model is not needed.

Figure 3.5 a shows the surface topography z_0 (topmost line) and the indentation depths δz at *set points* A/A_0 ranging from 0.995 to 0.65. The figure shows data taken from a single line of the 30×30 APD curve array. One clearly sees that the indentation becomes more and more sinusoidal at lower *set points*, suggesting to draw spherical cylinder cross sections below the lines. This seems reasonable if one assumes that it is impossible for the tip to push the glassy PS cylinders deeper into the PB matrix.

Figure 3.5 b) shows two indentation curves taken on a silicon surface (using the same tip; $A_0 = 55$ nm) and on a thin film of homopolystyrene (using a different tip, $A_0 = 45$ nm). The surface of silicon is very hard; therefore, only small indentation is expected. Nevertheless, the indentation rapidly grows to 3 nm and then increases to about 4 nm at very low *set points*. Therefore, the z -position of the tip where attractive forces become measurable is roughly 3 nm apart from the point where the hard surfaces really touch each other, leading to the kink in the indentation. This distance may be due to a thin layer of water adsorbed on both the tip and the SiO_x surfaces and/or to a nonvanishing contribution of van der Waals forces. On homopolystyrene, a maximum indentation of 5 nm is found. This value is significantly smaller than the maximum indentation on the PS-rich phase of the SBS sample (some 15 nm).

In the following we like to compare this findings with the near-surface microdomain structure derived from crystallographic data (Figure 3.5 c). The high indentation depths observed even on the harder parts of our sample indicate that the block copolymer surface is covered by a continuous layer of polybutadiene on top of the polystyrene cylinders. This is expected given that polybutadiene has a lower surface energy than polystyrene. The measurements of the indentation depth enable us to estimate the thickness of this PB surface layer. Considering that homopolystyrene could be indented by some 5 nm and that the hard region of the block copolymer sample could be indented by some 15 nm, one can estimate a PB layer thickness of $\geq 10 \pm 1$ nm. This certainly is a lower limit, since it is based on the assumption of infinite PB compressibility. This estimate for the PB layer thickness happens to agree quite well with the values expected for an ideal SBS surface of the given bulk structure. Given a diameter of 25 nm for the

3.3 Results and Discussion

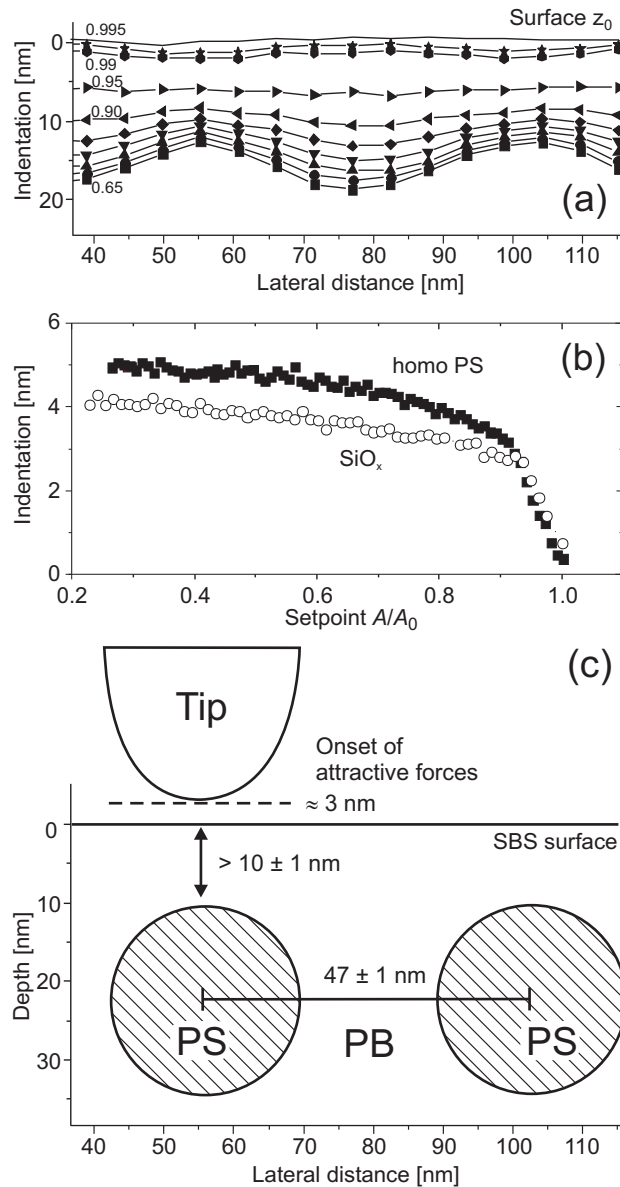


Figure 3.5: (a) Indentation for *set points* $A/A_0 = 0.995, 0.990, 0.95, 0.90, 0.85, 0.80, 0.75, 0.70,$ and 0.65 as well as the “true surface” z_0 (data from one line of the 30×30 APD array; both axis have the same scale). (b) Indentation on silicon (free amplitude $A_0 = 55$ nm) and homopolystyrene (different tip, $A_0 = 45$ nm). (c) Proposed model for the near surface structure of the SBS sample (corresponding to the data shown in (a) and Figure 3.3; the cross section does not cut perpendicular through the PS cylinders).

3 Where Is the True Sample Surface?

PS cylinders and an inter cylinder spacing of 45 nm, one calculates a thickness of 7 nm for the PB layer covering the topmost PS cylinders.

We are well aware of the limitations of such a quantitative evaluation of the TM-SFM data. One has to realize though that other techniques capable of determining the PB surface layer thickness with nanometer resolution (e.g., cross-sectional TEM or depth profiling) require complex sample preparation or do not have sufficient lateral resolution. Therefore, we feel that quantitative TM-SFM experiments can serve as an accurate while still simple technique for a quantitative characterization of the *native* near-surface morphology of soft materials.

3.4 Conclusion

We have investigated in detail the processes involved when soft polymeric materials are imaged with TM-SFM. In particular, we have presented a procedure to establish reliably with TM-SFM the true surface topography of a soft polymeric sample. The measurement of an array of APD curves enabled us to distinguish quantitatively between the “real” surface topography and lateral differences in tip indentation. We find that conventional TM-SFM height images are not necessarily reflecting the surface topography of the sample. In the case of the investigated SBS we find that the surface is flat and that conventional TM-SFM height images reflect lateral differences of tip indentation. Changes in height and phase contrast could be attributed to the crossover between regimes where attractive and repulsive forces, respectively, dominate the tip-sample interaction. Laterally resolved quantitative determination of indentation depths finally enables one to estimate the thickness of “soft” surface layers on such tiny structures as block copolymer microdomains. In the case of SBS, the AFM results obtained in this way agree quantitatively with the microdomain spacing expected from crystallographic data.

We note that a sound determination of the real surface topography is of quite some importance for the comparison of experimental data with any model of a sample’s subsurface structures in particular, in numerical simulations aiming to predict near-surface morphologies of block copolymers and other complex fluids [Mat97, Hui00]. Flat boundaries are often used as they tend to simplify the simulations. Our results on SBS demonstrate that for this particular case the as-

3.4 Conclusion

sumption of a planar interface between the block copolymer and the surrounding medium (air) is valid.

Finally, we have demonstrated that even on very soft polymeric samples TM-SFM can be applied as a quantitative and well-controlled analytical technique. What sometimes appears as artifacts in TM-SFM height and phase images can be related to the particular tip-sample interactions dominating in different *set point* regimes.

3 Where Is the True Sample Surface?

4 Strong Segregation Theory of Thin Films of Cylinder Forming Block Copolymers

In this chapter a strong segregation theory for thin films of cylinder forming block copolymers is developed. The free energies and the principal dimensions of structures build up from cylinders are discussed in the case of equally interacting surfaces. The cylinders may be aligned perpendicular C_{\perp} or parallel to the surface with the majority component wetting the surfaces C_{\parallel} or with half cylinders at the surface $C_{\parallel}^{1/2}$. The existence of a surface distorts the unit cell of the C_{\parallel} structure, which leads to a general increase in the free energy of this structure. In a phase diagram this phase becomes stable only for a finite attraction of the B block to the surfaces. For a smaller attraction of the B block to the surfaces the perpendicular alignment of the cylinders is stable, while a parallel configuration with half cylinders at either surface becomes stable for repulsion of the B block from the surfaces. The existence range of the parallel structures is modulated by the energetic penalty of fitting an integer number of cylinder layers to a non commensurable film thickness. This stretching or compression of the cylindrical unit cell in turn leads to a decrease or increase in the principal spacing of the parallel oriented cylinders, respectively.

4 Strong Segregation Theory of Thin Films

4.1 Introduction

As in the experimental case most of the theoretical work on AB diblock copolymer films has been done for symmetric diblock copolymers forming lamellar phases. A first study of the influence of a surface on a block copolymer has been done by Fredrickson [Fre87] in the weak segregation regime by extending the bulk theory of Leibler [Lei80]. A surface which has preferential affinity to one of the blocks induces composition oscillations close to the surface even if the bulk copolymer is disordered. The decay length is predicted to diverge at the critical point meaning it transforms into lamellae aligned parallel to the surface. Shull [Shu92] presented a self consistent mean field (SCFT) treatment of block copolymers in bulk and in films for phases without lateral structure, i.e. lamella oriented parallel to the surface. SCFT theory accounts for the full range between weak and strong segregation. Turner investigated the same system using strong segregation theory (SST) [Tur92]. SST calculations are analytic. On the other hand they rely on simple geometries of the phases and assume that the chains are uniformly stretched. Therefore they apply only at high interactions between the blocks, where the stable phases only depend on the composition and not on the interfacial tension of the block copolymer. SCFT calculations done by Matsen [Mat97] extend this work for structures having lateral but still lamellar structures. He compares his results to previously found strong segregation results of Semenov [Sem85]. Matsen found that in general parallel alignment is favorable, while perpendicular alignment is stabilized by an incommensurability of the lamellae period with the film thickness [Mat97]. A mixed structure was found to be only stable for slightly asymmetric copolymers. Further studies of lamellar systems have been performed by Fasolka [Fas00] for ultra thin films. They find "hybrid structures" stable for asymmetric surface and substrate interactions. Recently it has been shown with density functional theory (DFT) calculations that packing effects at the surfaces might stabilize perpendicular orientations and enhance their existence range [Fri02]. DFT calculations have the advantage to include compressibility effects and therefore density fluctuations. The same is true for Monte Carlo simulations. They deal with highly simplified models but treat the statistical thermodynamics exactly and are therefore well suited to test SCFT calculations. For a review see ref. [Bin00]. The outcome is that SCFT calculations predict the sequence of phases correctly at least for large $\chi N > 30$ but

4.1 Introduction

slightly underestimate the width of the interfaces between A and B rich regions.

Theoretical calculations for thin films of a block copolymer with a bulk structure of hexagonally ordered cylinders have been done with the help of various techniques. Turner et al. [Tur94] combined weak segregation calculations for asymmetric block copolymers with strong segregation calculations. They found a transition from the bulk hexagonal phase to a surface induced lamellar ordering of the diblock copolymers. Similar results are found by Brown et al. [Bro94]. Huinink et al used a dynamic DFT [Hui00, Hui01] algorithm and found similar results as in the lamellar case for parallel and perpendicular orientation of the cylinders. They also predict a transition from a cylindrical to a perforated lamellar and then to a lamellar phase with increasing surface interactions. Monte Carlo simulations on asymmetric block copolymers [Wan01, Sza03, Wan03] show the same transitions and show that the lateral cylinder spacing might be smaller than in the bulk [Wan01]. At weak interactions they also report half cylinders at the surfaces. This structure was also investigated by SST theory [Per01, Mat03, Per03].

In summary, it is well established that surfaces might induce transitions from a hexagonal phase to a perforated lamellar or a lamellar phase in the case of strong surface interactions. For weak surface interactions parallel or perpendicular alignment of the cylinders is predicted depending on the commensurability of the film thickness to the bulk spacing of the cylinder layers. The parallel aligned cylinders either terminate with a half cylinder or with the matrix B block at the surfaces in the case of a preferential attraction of the A block or the B block to the surfaces, respectively.

In the following we want to study the behavior of cylinder forming block copolymers in the case of weak surface interactions in more detail. We model the equilibrium behavior of thin AB diblock copolymer films by means of strong segregation theory, which assumes that the copolymer forms sharp interfaces between the A and B block. The block copolymer is assumed to have a volume fraction f such that it forms hexagonally ordered cylinders in bulk. We want to study the free energy and the lateral distances between the cylinders in the thin film as a function of the film thickness t .

Olmsted and Milner [Olm98, Olm95] introduced a method to estimate an upper bound of the free energy in the phases of lamellae, cylinders, spheres, and bicontinuous structures. In order to locally fix the volume fraction per molecule

4 Strong Segregation Theory of Thin Films

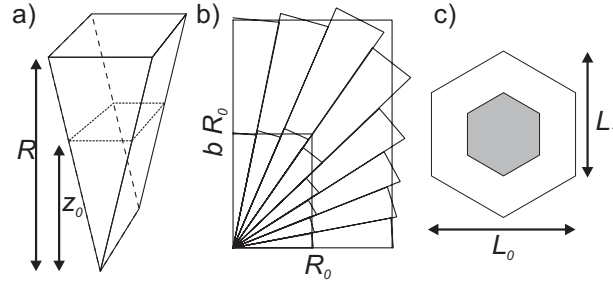


Figure 4.1: (a) Wedge used for building up cylindrical structures. The height of the wedge is R and the A/B Polymer interface is located at height z_0 . (b) Filling of the rectangular unit cell by wedges. c) Bulk unit cell of width L_0 . The bulk spacing of cylinder layers is $L_1 = \sqrt{3}/2 L_0$

they split the geometry into tiny wedges of a certain shape, which themselves fulfill the volume constraint. In a first approach they assumed straight paths of the chains through the A-B interface, i.e. straight wedges. It turns out that this method estimates a free energy of the hexagonal cylinder phase 3.6% larger than the free energy of a cylinder with a round unit cell. Later they relaxed the straight path approximation for the hexagonal phase by introducing kinked paths. They found an upper bound of the free energy to this phase, which lies very close to the lower bound using round unit cells.

4.2 Theory

We start with a brief outline of the Olmsted-Milner wedge calculation and recover their results for the hexagonal cylinder unit cell and the square unit cell in the straight path approximation. Then we adopt the method for the unit cells present in a thin film and calculate the dimensions of the cells and the free energies per molecule depending on the thickness of the film. Additionally we study the influence of the surface tension on our results and present a phase diagram of stable structures for varying surface interactions.

The wedge used for describing cylinders and the distribution of the wedges in a rectangular unit cell is shown in Figure 4.1 (a) and (b), respectively. Block A fills the volume below the interface located at height z_0 while the B block fills the remaining volume up to height R . The volume occupied by the A block relative to the total wedge volume has to satisfy the local volume constraint and thus

4.2 Theory

determines the height z_0 of the dividing interface as

$$z_0^2/R^2 = f \quad (4.1)$$

The energy of stretching in a single wedge is calculated by methods developed for polymer brushes and is outlined in ref [Olm98]. The result of this calculation is:

$$F_{stretch}(R) = \frac{3\pi R^2}{8v(1)} \left[\frac{1}{(1-f)R_B^2} I_A + \frac{1}{fR_A^2} I_B \right] \quad (4.2)$$

$$I_A = \int_0^{1-\sqrt{f}} (y + \sqrt{f})y^2 dy \quad (4.3)$$

$$I_B = \int_0^{\sqrt{f}} (\sqrt{f} - y)y^2 dy, \quad (4.4)$$

where R_A and R_B are the radii of gyration of the respective blocks and $v(1) = 1/2$ is the relative volume of the wedge for the hexagonal phase. Introducing the characteristic lengths $l_A = V_A/R_A^2$ and $l_B = V_B/R_B^2$ and the asymmetry parameter $\epsilon = \sqrt{l_A/l_B}$ we get

$$F_{stretch}(R) = \frac{3\pi R^2}{8v(1)} \frac{\sqrt{l_A l_B}}{V} \left[\frac{\epsilon}{(1-f)^2} I_A + \frac{1}{\epsilon f^2} I_B \right], \quad (4.5)$$

where $V = V_A + V_B$ is the total volume of a polymer molecule. The characteristic length l_A is independent of the length of the A block and is larger for more flexible chains. A smaller ϵ indicates an enhanced tendency for the B block to stretch. For the blocks polybutadien (PB) and polystyrene (PS) used in our experiments ϵ has been determined to be $\epsilon_{PS-PB} = 0.76$ [Olm98].

The total Energy F_{tot} of a unit cell of width L is calculated by integrating

4 Strong Segregation Theory of Thin Films

$F_{stretch}$ over all wedges and adding the interfacial energy $F_{Interface}(L)$:

$$F_{tot}(L) = \frac{1}{\int_{cell} dv} (F_{interface}(L) + \int_{cell} F_{stretch}(R(\theta)dv(\theta))) \quad (4.6)$$

$$F_{Interface}(L) = \gamma_{AB}A_{Int}(L), \quad (4.7)$$

where A_{Int} is the area of the AB interface in the unit cell, γ_{AB} is the surface tension between A and B blocks. The geometry of the unit cell used for the calculation is included in the length of the wedge $R(\theta)$ and the wedge volume $dV(\theta)$. These terms have to be adapted to the geometry under consideration.

To find the optimal size L_{min} of the unit cell, equation 4.6 is minimized with respect to L . The optimal free energy is then $F_{tot}(L_{min})$.

4.3 Results

4.3.1 Example: Rectangular unit cell

As we want to calculate the free energy as a function of the film thickness, we need to consider stretched unit cells. As an example we calculate the free energy of a stretched cubic or rectangular unit cell. The cell is shown in Figure 4.1 (b). In the straight path approximation the core of the cell is also a rectangle scaled down by a factor of \sqrt{f} .

The length $R(\theta)$ for a wedge in the rectangular unit cell of width L and height bL is given by $R(\theta) = L \cos^{-1}(\theta)$ for the first sector and by $R(\theta) = bL \cos^{-1}(\frac{\pi}{2} - \theta)$ for the second sector. The wedge volume $dv(\theta)$ is given by $dv(\theta) = \frac{1}{2} L^2 \cos^{-2}(\theta) d\theta$ and $dv(\theta) = \frac{1}{2} L^2 b^2 \cos^{-2}(\frac{\pi}{2} - \theta) d\theta$ for the two sectors, respectively.

Inserting this into equation 4.6 and minimizing with respect to L yields values for the optimal size $L_{min,rect}$ and the optimal free energy $F_{min,rect}$ as a function

of the stretching b :

$$L_{min,rect}(b) = \left(\frac{24(1+b)}{b(1+b^2)} \right)^{1/3} \left(\frac{f^{3/2} \gamma V^2}{c(f, \epsilon) \pi^2 \sqrt{l_A l_B}} \right)^{1/3} \quad (4.8)$$

$$F_{min,rect}(b) = \left(\frac{9(1+b)^2(1+b^2)}{64b^2} \right)^{1/3} \left(c(f, \epsilon) \gamma^2 \pi^2 V \sqrt{l_A l_B} \right)^{1/3}, \quad (4.9)$$

where $c(f, \epsilon) = \frac{2f}{\epsilon} - \frac{2\epsilon(-1+\sqrt{f})^3(3+\sqrt{f})f}{(1-f)^2}$ captures the f and ϵ dependence of the free energy.

Olmsted and Milner expressed all free energies in terms of the free energy of a symmetric ($\epsilon = 1$) lamellar phase $F_{Lam} = \left(\frac{27\gamma^2\pi^2V\sqrt{l_A l_B}}{32} \right)^{1/3}$. We get:

$$F_{min,rect}(b) = F_{Lam} \left(\left(\frac{4}{3} \right)^{1/3} \left(\frac{1}{3b} + \frac{1}{2} + \frac{b^2}{6} \right) c(f, \epsilon)^{1/3} \right) \quad (4.10)$$

Since $F_{cyl} = c(f, \epsilon)F_{Lam}$ gives the free energy of a cylinder F_{cyl} with a round unit cell (see Olmsted for details), we recover their result in the case of a symmetric rectangle ($b = 1$) of $F_{min,rect}(1) = \left(\frac{4}{3} \right)^{1/3} F_{cyl}$.

We want to compare all values to the respective bulk values. The bulk unit cell is shown in Figure 4.1 c). The distance between cylinders in the bulk is L_0 , while the spacing of cylinder layers is $L_1 = \sqrt{3}/2 L_0$. Therefore it is suitable to express our results in terms of the unit cell width L_0 and the free energy per molecule F_0 of the bulk hexagonal phase in the further scope of this work.

$$F_0 = \left(\frac{10}{9} \right)^{\frac{1}{3}} F_{cyl} = \left(\frac{15}{16} \right)^{1/3} \left(c(f, \epsilon) \gamma^2 \pi^2 V \sqrt{l_A l_B} \right)^{1/3} \quad (4.11)$$

$$L_0 = \left(\frac{144}{5} \right)^{1/3} \left(\frac{f^{3/2} \gamma V^2}{c(f, \epsilon) \pi^2 \sqrt{l_A l_B}} \right)^{1/3} \quad (4.12)$$

4 Strong Segregation Theory of Thin Films

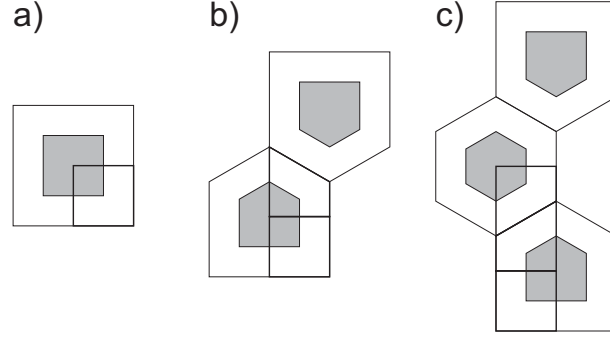


Figure 4.2: Unit cells of a thin film: (a) One layer of cylinders: rectangular cell. (b) Two layers: mixed stretched hexagonal and rectangular cell. (c) Three layers: additional stretched hexagonal unit cell. The thick lines mark the actually calculated cells.

4.3.2 Thin film unit cells for in plane oriented cylinders

The unit cells used for building up a thin film structure are shown in figure 4.2. The rectangular unit cell of one layer of cylinders has already been calculated in the example and can be written in terms of F_0 and L_0 as

$$F_{rec} = \left(\frac{3}{20}\right)^{1/3} \left(\frac{(1+b)^2(1+b^2)}{b^2}\right)^{1/3} F_0 \quad (4.13)$$

$$L_{rec} = \left(\frac{5}{6}\right)^{1/3} \left(\frac{1+b}{b+b^3}\right)^{1/3} L_0. \quad (4.14)$$

Note that for no deformation ($b = 1$) the width of the cubic cell is $\left(\frac{5}{6}\right)^{1/3} L_0 \approx 0.941 L_0$, which is 6% less than the width of the hexagonal unit cell. Its free energy is $\left(\frac{6}{5}\right)^{1/3} F_0 \approx 1.062 F_0$, which is 6% more than the free energy of the hexagonal unit cell.

The unit cell for $n+1$ layers of cylinders consists of a mixture of one rectangular unit cell and n hexagonal unit cells (see Figure 4.2 c)). Since the equilibrium widths of both structures is different, we need to add the free energies of the two structures and minimize the compound free energy again with respect to L .

The free energy $F_{\parallel}(b, n)$ and the width of the unit cell $L_{\parallel}(b, n)$ of a film of any number of cylinder layers can be expressed as a function of the number of

cylinder layers $n + 1$ and calculated analytically.

$$\frac{F_{\parallel}(b, n)}{F_0} = \frac{1}{90^{\frac{1}{3}}} \left(\frac{(1 + b^2) (12 + 5 \sqrt{3} n) (3 + \sqrt{3} \sqrt{3 + b^2} n + b (3 + \sqrt{3} n))^2}{b^2 (2 + \sqrt{3} n)^3} \right)^{\frac{1}{3}} \quad (4.15)$$

$$\frac{L_{\parallel}(b, n)}{L_0} = \left(\frac{10}{3} \right)^{\frac{1}{3}} \left(\frac{3 + \sqrt{3} \sqrt{3 + b^2} n + b (3 + \sqrt{3} n)}{b (1 + b^2) (12 + 5 \sqrt{3} n)} \right)^{\frac{1}{3}} \quad (4.16)$$

The derived equation 4.15 gives the free energy per molecule in a thin film without surface interactions. Also any entropic configurational penalties at the surfaces are neglected [Mat97].

Up to this point we calculated all values as a function of the stretching b of the unit cell. For each "stretching" number b we get a width of the unit cell $L_{\parallel}(b, n)$ and the free energy per molecule area $F_{\parallel}(b, n) / F_0$. The thickness of the thin film $t(b, n)$ is given in equation 6.4. To express all values as a function of the film thickness t , we need to solve equation 6.4 for b . This can be done for the rectangular and the stretched hexagonal unit cell, but not for the mixed unit cells.

$$t(b, n) = \left(n \frac{\sqrt{3}}{2} + 1 \right) b \frac{L_{\parallel}(b, n)}{L_0} \quad (4.17)$$

Therefore we plot $F_{\parallel}(b, n) / F_0$ and $L_{\parallel}(b, n)$ as a function of the film thickness $t(b, n)$. The result of this procedure is shown in Figure4.3. Note that the energetic offset of the minima in the free energy curve becomes smaller with increasing film thickness. In the limit of large n the value of the free energy has to approach the bulk free energy. The increase in the minimal free energy with decreasing number of cylinder layers is caused by the increasing importance of the (partially) rectangular unit cell close to the surface.

A more appropriate quantity for describing thin films is the excess free energy per unit area of the film $\Delta\Gamma$, equivalent to an additional surface tension of the

4 Strong Segregation Theory of Thin Films

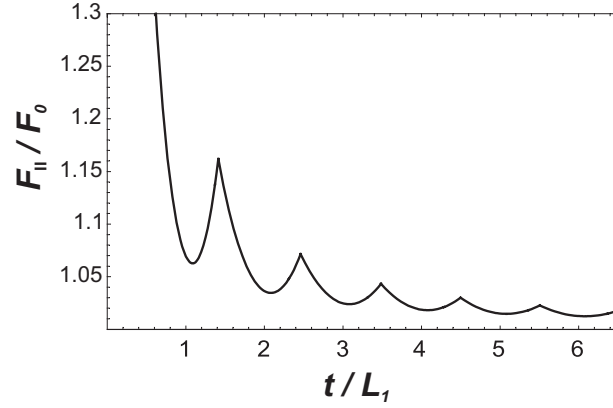


Figure 4.3: Free energy per molecule $F_{||}(b, n)$ in units of the free energy in the bulk F_0 versus the number of cylinder layers in the thin film $n + 1$.

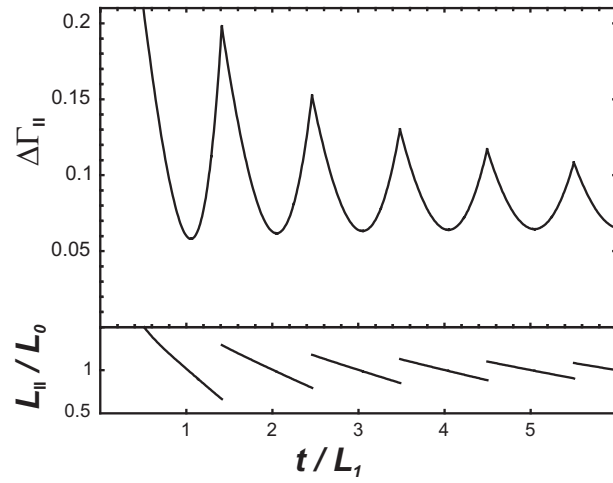


Figure 4.4: Free energy per unit area $\Delta\Gamma_{||}(b, n)$ and width of the unit cell $L_{||}$ as a function of the thickness of a thin film. Surface energies are not included.

film. It can be derived from $F_{||}$ by multiplying its energy difference to the bulk value F_0 with the thickness $t(b, n)$ of the film.

$$\Delta\Gamma_{||}(b, n) = \left(\frac{F_{||}(n, b) - F_0}{F_0} \right) t(b, n) \quad (4.18)$$

The result of this calculation is shown in Figure 4.4. This time the energetic offset of the minima in the free energy increases with increasing film thickness since the total free energy is considered. As mentioned before, the width of a cubic unit cell is smaller than the width of the rectangular unit cell. Therefore in

thick films ($t \rightarrow \infty$) the overall energy penalty is determined by the free energy of a rectangular unit cell of width L_0 , while it is less in thinner films, since the total structure relaxes. Note the sawtooth like behavior of the unit cell width, which has to be compared to the lateral cylinder spacing found in an experiment.

4.3.3 Effect of Surface Tension

The existence of a surface to air and an interface to the substrate gives a considerable contribution to the free energy of the film. In the literature the free energy contribution of a surface/interface is usually calculated by considering the surface tension γ of the block being in contact with the surface. We need to express the surface and interfacial tensions in terms of F_0 and L_0 and get the additional free energy contribution $\Delta\Gamma_{sur}$ of the surface tension γ .

$$\Delta\Gamma_{sur} = \frac{\gamma_{BS} \gamma_{AB} V}{F_0 L_0} = \frac{\gamma_{AB}}{3\sqrt{f}}, \quad (4.19)$$

where $\gamma_{BS} = \gamma/\gamma_{AB}$ is the dimensionless surface tension in units of the interfacial tension γ_{AB} . Since the surface tension gives rise to an additive value to the free energy of the system and is independent of the film thickness, it does not affect the behavior of the film as long as it does not dewet. This result is in contradiction to results presented by Turner [Tur92]. Turner calculated the free energy per molecule and not per unit area. In a thin film the relevant quantity is the surface energy per unit area, which is minimized in equilibrium. This result is supported by several other publications [Mat97, Wan01, Fri02].

4.3.4 Terrace Heights

A film prepared at a film thickness in between two optimal film thicknesses will eventually split into areas having a lower thickness (holes) and areas having a larger film thickness (islands). This behavior is driven by a minimization of the free energy of the system. If the curvature of the free energy as a function of film thickness is negative the film is unstable and will spontaneously form holes and islands. Within our theoretical treatment the curvature of the free energy is always positive except at the points where the free energy curves of a different

4 Strong Segregation Theory of Thin Films

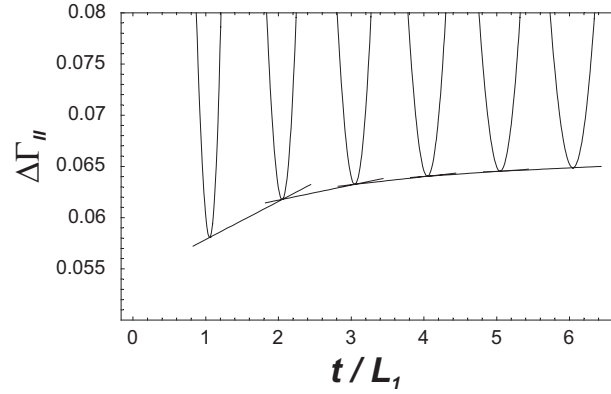


Figure 4.5: Free energy per area and common tangents of neighboring energy 'parabolas'. The thickness at which the tangents touch the free energy curve is the equilibrium thickness of holes and islands in a thin film.

number of cylinder layers meet. If it is still possible for the film to gain energy by splitting into terraces, the film is called metastable.

The equilibrium thickness of the terraces can be deduced by minimizing the free energy per area of the holes and of the islands under the constraint of volume conservation in the thin film. This can be done graphically by constructing a common tangent of two neighboring 'parabolas' of the free energy per unit area. The thickness at which the common tangent touches the first and the second 'parabola' gives the thickness of the hole and of the island, respectively.

Figure 4.5 shows this construction for our system. Deviations of the film thickness of a given number of cylinder layers either formed as hole or island increase with decreasing number of cylinder layers in the system. For the first layer of cylinders only a tangent to the free energy of the second layer of cylinders can be constructed. Therefore we can only make statements about this layer formed as a hole. Films with a thickness below the optimal thickness of the first layer of cylinders would be stable in our treatment. Nevertheless additional minima of the free energy will exist at lower thickness due to structures not accounted for in this treatment. For example at very low thicknesses additional effects of an effective surface potential will come into play [See01, See01a, BW91].

Mathematically the common tangents have been constructed as follows. The formula of the tangent for any point on the free energy curve has been derived by using the derivative of the free energy as slope and the point as zero point of the tangent. Then the common tangent is found by comparing the y-axis intercept

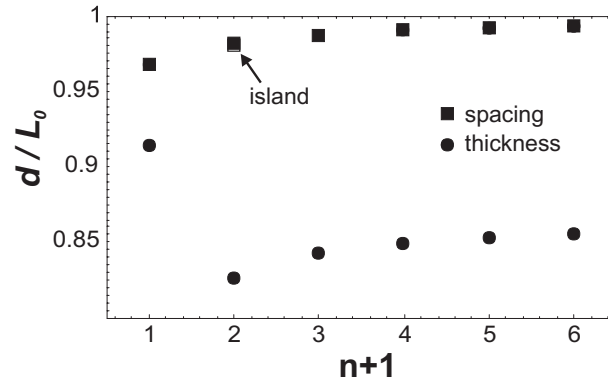


Figure 4.6: The lateral cylinder spacing (■), i.e. the width of the unit cell, and the thickness of one cylinder layer as function of the number of cylinder layers. For the first layer the optimal thickness is plotted. The differences in the lateral cylinder spacing determined on a terrace formed as hole or island is only seen for 2 layers of cylinders as marked by the arrow.

and the slope for two tangents belonging to neighboring 'parabolas'.

The thickness of a single layer of cylinders is displayed in figure 4.6 together with the respective width of the unit cell. The thickness is given by the thickness difference of a terrace consisting of $n+1$ cylinder layers formed as an island and a terrace of n layers of cylinders formed as a hole. Since our theory cannot predict the thickness of the first layer of cylinders formed as an island, its optimal thickness is plotted. All distances are measured in terms of the bulk cylinder spacing L_0 . The thickness of a single cylinder layer for thick films approaches the bulk value $L_1 = \sqrt{3}/2 L_0 \approx 0.866L_0$. Note the rather large value for the thickness of the first layer of cylinders. This is due to its rectangular rather than hexagonal unit cell shape.

The cylinders spacing measured for a terrace which forms as a hole is always lower than the spacing measured for a terrace with the same number of cylinder layers formed as an island. The difference of both values is rather small and can only be seen in Figure 4.6 for the second layer cylinders as marked by the arrow. For the first layer of cylinders only the value found for this terrace formed as a hole is plotted.

4 Strong Segregation Theory of Thin Films

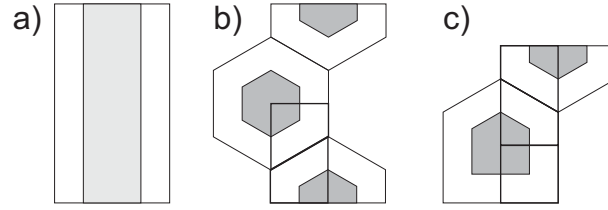


Figure 4.7: Other structures considered for the thin film than the C_{\parallel} structure. a) Cylinders oriented perpendicular to the film surface C_{\perp} . b) Cylinder oriented parallel with half cylinders at either surface $C_{\parallel}^{1/2}$. c) Cylinders oriented parallel terminating at one surface with a half cylinder and on the other surface with a rectangular unit cell C_{Mix} .

4.3.5 Comparison to other Structures

As mentioned before the calculation used here only gives an upper bound to the free energy of the film. The deviation from the lower limit, the free energy of a round cylinder unit cell is about 3.6 percent. Therefore it does not make sense to compare our results to free energies calculated for lamellar or spherical morphologies, since the free energy penalty of adapting the spacing of these structures to the film thickness will be in the same order of magnitude.

Nevertheless we can compare our results for parallel cylinders, denoted as C_{\parallel} for further reference, to other structures formed by cylinders in the thin film as shown in Figure 4.7. The structures are cylinders oriented perpendicular to the film C_{\perp} , in plane cylinders terminating on either side with a half cylinder at the surfaces of the film $C_{\parallel}^{1/2}$ and in plane cylinders terminating at one side with a rectangular unit cell and on the other side with a half cylinder unit cell C_{Mix} . Since we restrict our discussion to symmetric surface fields, the energy of the latter structure is degenerate with the energy of its inverted structure.

The first structure we consider are upright oriented cylinders C_{\perp} shown in Figure 4.7 a). We assume cylinders, which are not deformed by the existence of the surfaces but are simply cut by the surfaces. In this case we get an additional free energy from the fact that the A block is now in touch with the substrate interface and the surface. The area of A block exposed at the surfaces is f times the unit cell area. Therefore we can write the excess free energy $\Delta\Gamma_{sur,A}$ per unit

area as

$$\Delta\Gamma_{sur,A} = 2 \frac{\Delta\gamma_{AS} f}{3\sqrt{f}}, \quad (4.20)$$

where $\Delta\gamma_{AS}$ is the surface tension difference of the A block and the B block in units of the interfacial tension γ_{AB} .

The excess free energy per unit area is simply $\Delta\Gamma_{sur,A}$, since its structure is the same as the bulk structure.

$$\Delta\Gamma_{\perp} = \Delta\Gamma_{sur,A}, \quad (4.21)$$

Additionally we include a comparison to a thin film structure of parallel oriented cylinders terminating with half cylinders at the two surfaces denoted as $C_{\parallel}^{1/2}$ [Per01]. This structure is shown in Figure 4.7 b). The free energy of a unit cell of this structure is simply the free energy of a stretched hexagonal unit cell plus the energy penalty of exposing the half core to the surface. The area fraction of A block at the surface is \sqrt{f} .

$$\Delta\Gamma_{\parallel}^{1/2}(b, n) = \Delta\Gamma_{hex}(b, n) + 2 \frac{\Delta\gamma_{AS} \sqrt{f}}{3\sqrt{f}}, \quad (4.22)$$

The last structure we want to consider is a mixed structure C_{Mix} terminating at on surface with a half cylinder and on the other surface with a rectangular unit cell as shown in Figure 4.7 c). This structure is actually the C_{\parallel} structure cut in the middle of the film. Therefore its excess free energy per unit area for $n+1$ layers of cylinders equals half of the excess free energy of the C_{\parallel} structure for $2n+1$ cylinder layers. This can be seen by comparing the unit cells calculated for the C_{Mix} in Figure 4.7 c) with the ones calculated for the C_{\parallel} structure shown in Figure 4.2 c). The surface energy penalty for this structure is half of the one for the $C_{\parallel}^{1/2}$ structure.

$$\Delta\Gamma_{sur,Mix} = \frac{1}{2} \Delta\Gamma_{sur, half} = \frac{\Delta\gamma_{AS} \sqrt{f}}{3\sqrt{f}} \quad (4.23)$$

4 Strong Segregation Theory of Thin Films

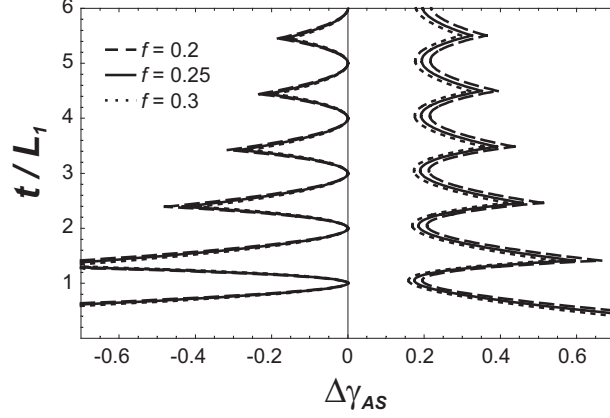


Figure 4.8: Phase Diagram of stable structures as a function of film thickness and relative surface tension of the A block. At zero preferential interaction of the blocks to the surfaces, the energy of the C_{\parallel} structure is degenerate with the energy of the non deformed $C_{\parallel}^{1/2}$ structure, since both structures are given by the energy of a hexagonal unit cell. The onset of the C_{\parallel} structure is at a finite $\Delta\gamma_{AS}$, since the deformation of the unit cell at the proximity of the surfaces induces an energy penalty.

$$\Delta\Gamma_{Mix}(b, n) = \frac{1}{2} \Delta\Gamma_{\parallel}(b, 2n) + \Delta\Gamma_{sur, Mix} \quad (4.24)$$

Now we can construct a phase diagram of the stable structures in a thin film. The stability lines are determined by comparing the excess free energies for the C_{\perp} structure to the one of the other structures and solving for $\Delta\gamma_{AS}$. As an example we do this for the C_{Mix} structure by comparing equations 4.21 and 4.24.

$$\Delta\gamma_{AS, BS, Mix} = \frac{3}{2(2\sqrt{f} - 1)} \Delta\Gamma_{\parallel}(b, 2n) \quad (4.25)$$

This formula diverges at $f = 0.25$. For $f < 0.25$ $\Delta\gamma_{AS, BS, Mix}$ becomes negative, while it is positive for $f > 0.25$. In the range of $0.2 < f < 0.3$ the value of $\Delta\gamma_{AS, BS, Mix}$ is too high to appear in the phase diagram. Nevertheless this structure will become important if one considers asymmetric boundary conditions.

Figure 4.8 shows the phase diagram depending on the relative surface tension of the A block $\Delta\gamma_{AS}$.

$C_{\parallel}^{1/2}$ is stable for a preferential attraction of the A block to the surface, while C_{\parallel} is stable at a preferential attraction of the B block to the surface. The surface tensions for aligning the structures parallel is in both cases rather small and will be easily met in most realistic systems.

4.4 Conclusion

Free energies

We established an analytical treatment of cylindrical microdomain structures in thin block copolymer films. The distortion of the unit cell of cylinders oriented parallel to the surface with the matrix polymer located at the surface induces an energetic penalty to this structure. The other structures under consideration, namely perpendicular oriented cylinders C_{\perp} and parallel oriented cylinders with half cylinders at the surfaces $C_{\parallel}^{1/2}$ maintain the bulk hexagonal unit cell, in the latter case, if the film thickness is commensurate to the bulk cylinder spacing. At an intermediate film thickness the C_{\parallel} and the $C_{\parallel}^{1/2}$ structure have to adjust their unit cells to the film thickness, which raises their free energy.

Principal dimensions

The non hexagonal unit cell of the C_{\parallel} structure close to the surface also effects the cylinder spacing and the thickness of a cylinder layer in the case of a small number of cylinder layers. The deviations amount to a few percent of the bulk dimensions and should be visible in experiments. If the film thickness is not optimal the height of the unit cell has to adapt and thereby induces modulations to the width of the cell. If the structure is compressed or stretched it shows a larger or smaller cylinder spacing, respectively. For the first layer of cylinders this effect is predicted to be directly related to the thickness variation, while it decreases indirectly proportional to the number of cylinder layers under consideration in thicker films.

Phase Diagram

A phase diagram has been calculated showing the stable structures for varying symmetric interfacial interactions. Perpendicularly oriented cylinder are stable at low effective attraction of the B block to the surfaces, while C_{\parallel} is stable at larger positive attraction and $C_{\parallel}^{1/2}$ is stable at repulsive interactions. In the considered case of symmetric interactions at the surfaces a mixed morphology of

4 Strong Segregation Theory of Thin Films

C_{\parallel} and $C_{\parallel}^{1/2}$ is not stable for $0.2 < f < 0.3$ at the considered range of surface interactions.

The existence of the C_{\parallel} structure depends on the volume fraction f of the A block since the contact area of A block with the surfaces increases with f for the C_{\perp} structure. The stability of the $C_{\parallel}^{1/2}$ structure is less affected by a change in f .

Note that the optimal thickness of the C_{\parallel} is always slightly higher than the one for the $C_{\parallel}^{1/2}$ structure. This of course is again due to the non hexagonal unit cell of the C_{\parallel} structure at the surfaces.

Comparison to other theories

This SST treatment of thin films of cylinder forming block copolymers should be compared to results determined by other methods. It does not include several effects which are incorporated in other methods.

The width of the interface is always sharp, which is a good approximation for strongly segregated systems. In weaker segregated systems this leads to an overestimation of the energy penalty for stretching the unit cells [Mat03], which in turn effects the variation of the cylinder spacing.

Entropic effects of chain ends close to the surface are not included in our calculations. The enrichment of chain ends near the surfaces results in a slight preference of neutral surfaces for the shorter block [Wan01]. This enhances mostly the stability of the $C_{\parallel}^{1/2}$ structure, since this structure has the highest fraction of A block at the surface. In the phase diagram its existence should be shifted to larger values of $\Delta\gamma_{AS}$, eliminating the degenerate behavior of $C_{\parallel}^{1/2}$ and C_{\perp} at $\Delta\gamma_{AS} = 0$. The same is true for the C_{\perp} in comparison to the C_{\parallel} structure.

Since no other structures than cylindrical ones are included in the calculations the phase diagram is only valid for weak interactions. Larger surface interactions enable a deformation of the cylinder unit cell and transitions to a perforated lamellar and a lamellar phase are expected close to the surfaces. This effect will also strongly depend on the volume fraction f of the A block since a larger f decreases the free energy difference between a lamellar phase and a phase of hexagonally ordered cylinders.

5 Phase Behavior in Thin Films of Cylinder-Forming ABA Triblock Copolymers ¹

We experimentally establish a phase diagram of thin films of concentrated solutions of a cylinder forming polystyrene-*block*-polybutadiene-*block*-polystyrene (SBS) triblock copolymer in chloroform. During annealing the film forms islands and holes with energetically favored values of film thickness. The thin film structure depends on the local thickness of the film and the polymer concentration. Typically, at a thickness close to a favored film thickness parallel orientation of cylinders is observed, while perpendicular orientation is formed at an intermediate film thickness. High polymer concentration eventually lead to a reconstruction of the cylindrical microdomains to a perforated lamella structure. Deviations from the bulk structure, such as the perforated lamella and a wetting layer are stabilized in films thinner than ≈ 1.5 domain spacings.

¹Parts of the results of this chapter have been published in: *Physical Review Letters* [[Kno02](#)]

5 Phase Behavior

5.1 Introduction

Supramolecular self assembly is widely used in nature to build highly regular and complex structures with dimensions much larger than the dimensions of the molecules. Block copolymers are an interesting model system to study this phenomenon because one is able to precisely control the architecture of the molecules. Furthermore these systems self assemble into patterns with length scales of 5 to 100 nm, which might be interesting for a variety of applications.

A block copolymer is built from two or more polymeric chains (blocks), which are chemically different and covalently attached to each other. Their phase behavior is controlled by the interaction between the blocks and the relative lengths of the blocks. If the interaction is large enough the polymer microphase separates and forms ordered structures depending on the relative volume fraction of the blocks, e.g. lamellae, gyroid, cylinders or spheres. The size of the nanostructures can be adjusted within a certain range by the overall molecular weight of the block copolymer (for recent reviews, see Ref. [Bat90, Bat99, Ham98]) and by addition of homopolymer [Has90, Jeo02]. An interesting application of these features is the use of block copolymers films for lithographic purposes [Par97, Gua02, Bla01, Par01, Che01], and/or templating of inorganic structures [TA00a, TA00, Li00]. The patterns may be aligned by the use of external electric fields [Mor96a], topographic templating [Seg01], and surface patterning [Hei99]. All these processes rely on the control of pattern formation of the block copolymer in thin films and therefore on a good understanding of the underlying physics.

The presence of a surface or interface is known to influence the microdomain structure in the vicinity of the surface, even if the bulk is not ordered [Fre87]. Generally, the block with the lower surface energy tends to accumulate at the surface. This preferential attraction to the surface (the surface field) typically leads to an alignment of the structure (lamellae, layers of cylinders, layers of spheres) parallel to the interface. In some cases this alignment extends over a large distance into the bulk of the material [Yok00]. In addition to alignment, the presence of a surface can also modify the microdomain structure close to the surface, similar to surface reconstructions known from classical solid state physics. This has first been observed for cylinder forming systems. If the minority component has a sufficiently lower surface energy than the majority component, a wetting layer is formed at the surface allowing the low surface energy phase

to completely cover the surface [Kar93]. In the opposite case, if the majority component is favored at the surface, a transition to one layer of a perforated lamella of the minority phase [Hui00, Hui01] and a lamella [Tur94] has been predicted to form at the surface. In lamella forming ABC triblock copolymers a complex surface reconstruction was observed for the case that the middle block has the lowest surface energy [Reh01, Reh03].

In a thin film the copolymer material is confined to a certain film thickness, which gives rise to additional effects: If the film thickness deviates from an integer multiple of the characteristic spacing, the chains need to stretch or compress, which leads to an increase of the free energy by entropic contributions. Therefore supported as well as free standing films form regions of different film thickness (terraces), which correspond to an integer multiple of the natural microdomain layer spacing. This has been observed for lamella [Cou89], cylinder [vD95] and sphere [Yok00] forming systems.

If the film is not free to adjust its local film thickness, i.e., in the case of two solid interfaces, the difference in the interfacial tension of the blocks controls the thin film behavior. For lamella forming systems a large surface field forces the lamellae to stretch and adapt a new, commensurable layer spacing [Lam94]. In the case of a weak surface field, lamellae oriented perpendicular to the substrate [Wal94, Kel96]. In cases where the two interfaces favor different orientations, both can coexist and a mixed (hybrid) microdomain structure is stabilized [Fas00, Fas01].

Cylinder forming block copolymers show a more complex phase behavior in thin films. In the case of a weak surface field, the bulk microdomain structure is not significantly altered and the orientation behavior of cylinders is analogous to lamella forming systems. When the surfaces preferentially attract the majority block, the cylinders align parallel to the substrate [vD95, Mag97, Kim98, Kim98a]. Otherwise, half cylinders may form [Kim01a]. A perpendicular orientation of cylinders, however, has been stabilized only with the help of an electric field [TA00a] or by fast drying in solvent cast films [Kim98, Kim98a, Lin02].

In the case of strong surface fields, a variety of deviations from the bulk structures has been observed. If the minority block has the lower surface energy a transformation to a wetting layer (a half lamella) [Kar93] and a lamella [Rad96] have been observed in very thin films. If the majority block is accumulated

5 Phase Behavior

at the surface, a perforated lamellar phase has been reported in free standing films [Rad96]. Also mixed (or hybrid) structures, such as cylinders with necks [Kon00] and spheres on top of a perforated lamella layer [Har98] as well as an “inverted phase” [Zha00] have been observed. Various models have been developed [Tur94, Hui00, Hui01, Sev02, Per01, Wan01, Sza03, Fen02, Fen02b, Fen02a] to describe different aspects of this complex phase behavior. However, it remained unclear which of the reported phenomena are specific to the particular system and/or route of film preparation and which are general behavior.

In this chapter we present a unifying description of these phenomena. With experiments and computer simulations based on DDFT we show that the phase behavior in thin films of cylinder-forming block copolymers is dominated by surface reconstructions. Their stability regions are determined by the surface field and the film thickness and we show how these two constraints interact.

The outline of the chapter is as follows. We first show that chloroform is a nonselective solvent for our system, which does not alter the bulk microdomain structure of our polymer in the considered range of dilution. Therefore it merely introduces mobility to our system. We show how the thin film forms regions of preferred thickness to minimize its free energy. In-situ measurements prove the existence of microphase separation inside the thin films during preparation. They also show that the microdomain structure is preserved during the drying process of the swollen films. We then systematically analyze and identify the microdomain structure as a function of film thickness and polymer concentration and establish a phase diagram for our system.

5.2 Experimental

5.2.1 Materials

We have studied thin films of a polystyrene-*b*-polybutadiene-*b*-polystyrene (SBS) triblock copolymer swollen in chloroform vapor. SBS was obtained from Polymer Source Inc. with molecular weights $M_{w,PS} = 14$ kg/mol, $M_{w,PB} = 73$ kg/mol, and $M_{w,PS} = 15$ kg/mol (PS is polystyrene, PB is polybutadiene). Taking into account the densities of the homopolymers (1.05 g/cm³ for PS and 0.93 g/cm³ for PB) [Bra89] the volume fraction of PS is $f_{PS} = 0,26$. Polystyrene (PS) and Polybutadiene (PB) homo polymers used for ellipsometry were obtained from

5.2 Experimental

Polymer Standard Service (Mainz, Germany) with molecular weights of $M_{w,PS} = 520$ kg/mol and $M_{w,PB} = 47$ kg/mol.

For scanning force microscopy (SFM) and ellipsometry experiments, polished silicon substrates were cut from wafers, cleaned in fresh 1:1 H_2SO_4 (conc.)/ H_2O_2 (30%) solution, thoroughly rinsed in boiling and cold Millipore water and finally cleaned with a Snowjet®.

5.2.2 SAXS

The bulk microdomain structure of concentrated SBS solutions in chloroform was investigated using small angle X-ray scattering (SAXS). All measurements were performed at the ID2A beamline at the European Synchrotron Radiation Facility (ESRF, Grenoble, France). The energy of the beam was set at 12.5 keV. SAXS spectra were measured of SBS solutions in chloroform at different polymer weight fractions. Solutions of 30, 40 and 50 wt% SBS and a bulk sample were prepared. Dilute solutions were either injected into a chamber with microscope slides as windows (30 wt%) or directly prepared in capillaries (30 and 40 wt%). At high concentrations (40 and 50 wt%) injection was not possible due to the high viscoelastic behavior of the solution. For these concentrations a droplet of the solution was put directly into the beam and immediately measured. The bulk sample was prepared by slowly drying a SBS solution inside a mark capillary. Due to the high scattering cross section of the chlorine atoms and the long beam path of 5 mm through the chamber, imaging times of 3 to 5 s had to be chosen for the samples not prepared in capillaries.

5.2.3 Thin Film Preparation

For ellipsometry measurements, polymer films of PS, PB, and SBS were spun cast from toluene solutions (2 wt%) yielding an initial film thickness of about 125 nm.

To study the thin film phase behavior of SBS, films were spun cast from toluene solution onto polished silicon substrates. Solutions with 0.25, 0.5, 0.75, 1, 1.5 and 2 wt% SBS and a spinning speed of 2000 rounds/min were used. This procedure resulted in films with a thickness of about 12, 25, 35, 50, 80 and 125 nm, respectively, and with a surface roughness of less than 1 nm as measured

5 Phase Behavior

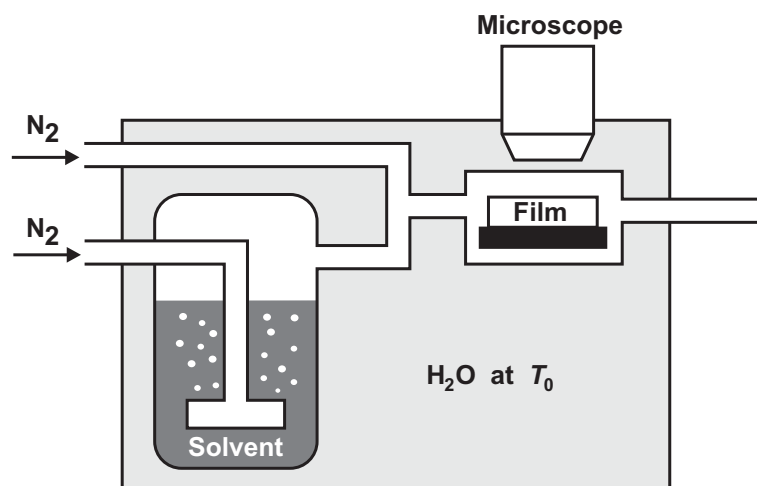


Figure 5.1: Sketch of the experimental setup for swelling in chloroform vapor. Two flows of air or N_2 are mixed, one of them is saturated by $CHCl_3$ vapor by passing it through a washing-bottle. The flow ratio of the two gas streams determines the vapor pressure in the sample chamber. The sample can be viewed with an optical microscope to follow terrace formation. After annealing, the sample is quickly removed from the vapor in order to quench the microdomain structure.

by SFM. In order to equilibrate (anneal) the microdomain structure, the films were exposed for several hours to a controlled partial pressure p of chloroform vapor. The experimental setup is shown in Figure 5.1. Two flows of Nitrogen gas, one saturated with chloroform vapor in a washing bottle, are mixed just before entering the sample chamber. The volume flow for each line was regulated via flow-meters and ranged from 20 to $50\text{ cm}^3/\text{min}$. The whole setup was made from glass using Teflon connectors. It was inserted into a water bath kept at $T_0 = 25.0 \pm 0.1\text{ }^\circ\text{C}$. An overpressure of $0.3 \pm 0.1\text{ bar}$ was applied to the system to detect possible leakage. The samples were placed onto a glass slide welded to a flange, which could be quickly removed from the chamber after equilibration to extract the solvent and quench the microdomain structure.

5.2.4 Ellipsometry

We used ellipsometry to determine the amount of chloroform within the polymer films at a given chloroform vapor pressure. All measurements were done on a SENTECH SE 850 spectroscopic ellipsometer. A homemade setup [Elb01] was used to establish an atmosphere with a controlled solvent vapor pressure.

The temperature of the sample and the temperature of a solvent reservoir were controlled to within 0.1 K. All measurements were performed at 65° incidence angle within a spectral range from 400 nm to 800 nm. The thickness h at a certain vapor pressure p was obtained from least-squares fits to the spectral data of the ellipsometer. The thickness of all films was measured upon swelling and deswelling of the sample to rule out possible hysteresis effects. Before and after measuring in solvent vapor, the thickness h_{dry} of the dry samples was measured. The polymer concentration ϕ_P in the film is given by

$$\phi_0 = \frac{h_{dry}}{h}, \quad (5.1)$$

assuming that the partial volumes of polymer and solvent in the film are additive.

5.2.5 Scanning Force Microscopy (SFM)

The microdomain structures at the surface of the dry films were imaged with a Dimension 3100 Metrology SFM from Digital Instruments, Veeco Metrology Group and a Nanoscope IIIa controller. Some data were taken using a Dimension 3100. The metrology system uses a hardware linearized piezo scanner, which allows very accurate measurements of distances and heights from the images. Both instruments were operated in tapping mode. Olympus and Nanosensors tapping mode cantilevers were used (spring constant ≈ 40 N/m, resonance frequency ranging from 200 to 300 kHz). All measurements were performed at free amplitudes of about 30-50 nm and a relative setpoint of about 0.95. Some experiments were performed in the presence of chloroform vapor (see text for details).

5.3 Results

5.3.1 Domain spacing in bulk SBS solutions

To measure the microdomain spacing of the copolymer solutions in bulk samples, we have performed synchrotron SAXS measurements at copolymer concentrations of 30, 40, and 50 wt % and for a bulk sample. The corresponding polymer

5 Phase Behavior

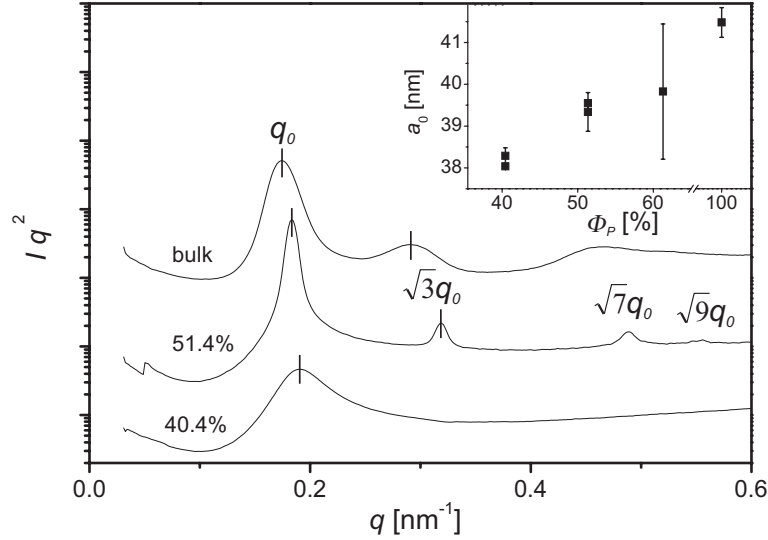


Figure 5.2: SAXS spectra from an SBS bulk sample and SBS CHCl₃ solutions with polymer weight fractions of 30%, 40% and 50%. The scattering peaks typical for a microdomain structure of hexagonally ordered cylinders are marked. The inset shows the spacing a_0 between next-nearest cylinders as a function of ϕ_P .

volume fractions of the solutions amount to $\phi_P = 0.40$, 0.51 , and 0.61 , respectively. The 2D-SAXS images were averaged azimuthally. The results obtained for the solutions prepared in the capillaries are shown in Figure 5.2. From the first order scattering peak at q_0 , the spacing between layers of cylinders can be extracted as $c_0 = 2\pi/q_0$. While the curve measured for $\phi_P = 0.40$ shows a rather broad first order peak and no higher order peaks, the spectrum measured at $\phi_P = 0.51$ shows a narrow first order peak and three higher order peaks at $\sqrt{3}q_0$, $\sqrt{7}q_0$, and $\sqrt{9}q_0$ characteristic for hexagonally packed cylinders. Since the bulk sample still shows one higher order peak at $\sqrt{3}q_0$, we assume a bulk microdomain structure of hexagonally ordered cylinders throughout the concentration regime used in this study for the thin film.

The inset to Figure 5.2 shows the next nearest neighbor spacing between cylinders $a_0 = 2/\sqrt{3}c_0$ as a function of ϕ_P for all samples prepared. The spacing increases with increasing polymer concentration. Within the concentration regime studied here, a_0 increases from 38.0 ± 0.3 nm to 41.5 ± 0.4 nm. The large error bar at $\phi_P = 0.51$ results from a highly distorted, elliptic scattering image due to difficult sample preparation at high ϕ_P .

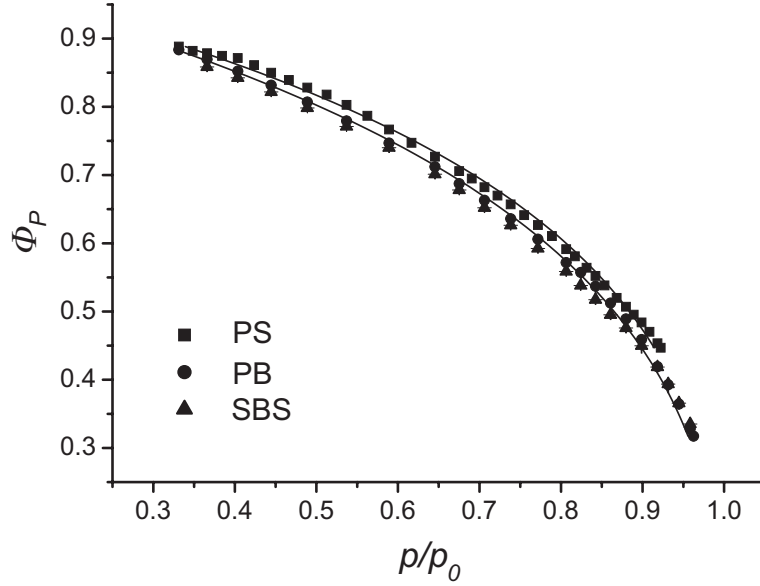


Figure 5.3: Polymer volume fraction ϕ_P as a function of the relative CHCl_3 vapor pressure of swollen films of polystyrene, polybutadiene, and the triblock copolymer SBS. The lines show fits of the measured data with a simple model (see text).

5.3.2 Swelling behavior and molecular interactions in thin SBS films

In order to quantify the polymer volume fraction within the thin films at a given solvent vapor pressure, we have measured the film thickness in the swollen state for films of PS and PB homopolymers, and SBS block copolymer. The solvent pressure was controlled by keeping the sample at 25°C and adjusting the temperature of a solvent reservoir inside the chamber to a lower temperature. With increasing solvent vapor pressure p the film takes up more solvent, i.e. ϕ_P decreases. If we denote the vapor pressure at saturation as p_0 , the chemical potential in the vapor phase is given by $\mu_v = \ln(p/p_0)$. A comparison to the chemical potential in the thin film μ_s , given by Flory Huggins theory [Flo89], yields the following relation between the normalized vapor pressure p/p_0 and the polymer volume fraction ϕ_P [Elb01]:

$$\ln(p/p_0) = \frac{\mu_v}{RT} = \frac{\mu_s}{RT} = \chi_{P,S} \phi_P^2 + \ln(1 - \phi_P) + (1 - 1/N) \phi_P. \quad (5.2)$$

N is the total degree of polymerization and $\chi_{P,S}$ is the Flory-Huggins inter-

5 Phase Behavior

action parameter between polymer and solvent. Assuming that $\chi_{P,S}$ does not depend on ϕ_P , the ellipsometric data can be fitted with a single parameter $\chi_{P,S}$. The results of least-squares fits are shown in Figure 5.3 (solid lines) together with the data. The agreement between the fit and the data is very good. The resulting interaction parameters $\chi_{P,S}$ of 0.29 ± 0.01 for PS/CHCl₃ and 0.21 ± 0.1 for PB/CHCl₃ agree with the published values [Bra89] in the respective concentration regime.

PB films swell by only about 3% more than PS films at a given chloroform vapor pressure. This shows that chloroform is a good solvent for both polymers, exhibiting only a small selectivity to PB. SBS takes up slightly more solvent than the respective homopolymers possibly due to an enrichment of solvent at the polymer-polymer interfaces, which thereby screens repulsive interactions between the S and B monomers [Fre89].

To measure the polymer volume fraction ϕ_P as a function of vapor pressure p under the conditions used for thin film preparation, the flow setup described above was connected to the ellipsometer cell and the same overpressure and temperature were applied. ϕ_P was measured for all combinations of gas flows applied during sample preparation. A table of the observed results is given in table 5.1.

Table 5.1: Polymer concentration at given flow in channel 1 (pure) and channel 2 (saturated) at 0.3 bar overpressure. Also given is the time of annealing and the number of the terraces formed as holes.

flow ch 1	flow ch 2	Polymer content ϕ_P	time [h]	Tn _h
3.5	3.5	0.76	6	0
4	4.7	0.69	6	0
3	4	0.66	6	1
3	4.5	0.63	12	1
3	4.5	0.63	2	0
4	6	0.62	8	0,1,2
3	5	0.58	6	1
3	5	0.58	6	0,1,2
3	5	0.58	6	1
3	5.3	0.55	6	1
3	6	0.53	1	0,1
3	7	0.49	7	0,1,2

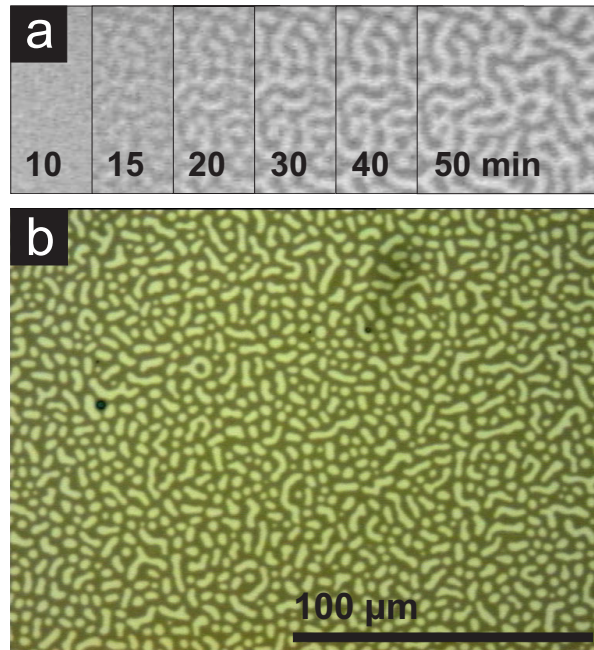


Figure 5.4: a) Optical micrographs of swollen films as a function of annealing time, visualizing the terrace formation. Terraces with different film thickness are visible because of interference of light scattered by the surface of the film and the substrate. The time scale of terrace formation depends on the vapor pressure and on the initial thickness of the film. b) Image of the quenched film after 7h of annealing. It shows that terraces extend over large areas of the sample.

5.3.3 Coarse grain structure of the SBS films: Terrace formation

During annealing the swollen SBS films form islands and holes. Figure 5.4a) shows a series of optical micrographs taken at different times of annealing. Within a timescale of about one hour the initially flat film develops areas of uniform thickness characterized by uniform interference colors in the optical image (Figure 5.4b). This behavior is known from experiments of thin films of block copolymer melts [Cou89]. It suggests that the local thickness adjusts to local minima of the free energy of the system, which are related to energetically preferred microdomain structures of the films. The initial film thickness was chosen such that islands and holes had similar area fractions at the applied solvent vapor pressure. Note that microphase separation inside the thin film is necessary to provide a driving force for terrace formation. Terrace formation has been observed for all samples with $\phi_P < 0.7$ during solvent annealing, indicating that the material

5 Phase Behavior

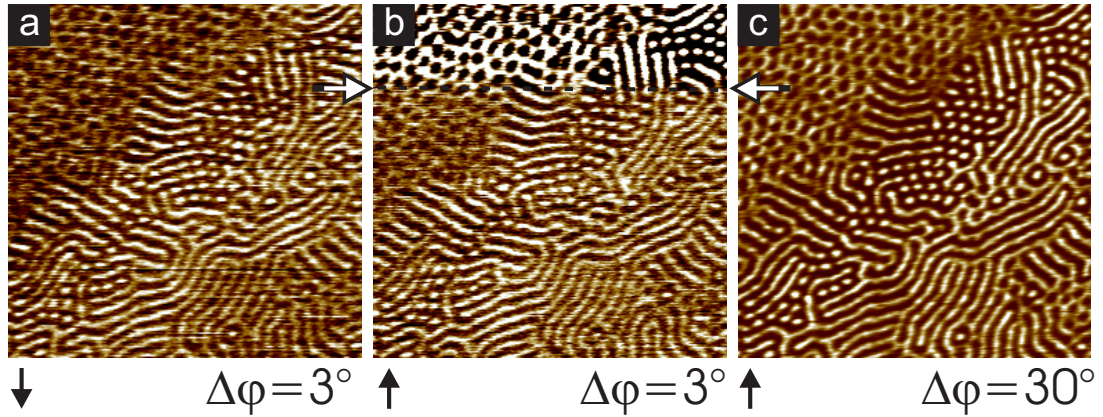


Figure 5.5: In-situ tapping mode SFM phase images ($2 \times 2 \mu\text{m}^2$). The capture direction, the time relative to the start of the in-situ experiment, and the range of the phase scale are denoted below the images. a) Image taken during swelling at $p/p_0 = 0.65$ ($\phi_P = 0.7$). In the upper part of b) (dark arrow) the drying process was started by switching to pure N_2 gas flow. c) Image of the dry film. Note the change in the phase scale from 3° in the wet state to 30° in the dry state.

inside the film is always well phase separated. Islands and holes formed in a very similar way in all samples irrespective of the film thickness except for the thickest films and the highest polymer volume fractions. In particular, at a film thickness of more than $3c_0$ and at polymer volume fractions $\phi_P > 0.65$ no well defined terraces were formed within the time scale of the experiment.

Typically the terrace formation was faster at higher vapor pressures and for thinner films, but no systematic study on the kinetics of terrace formation has been performed. The films prepared by spin casting are somewhat thicker near the edges of the samples. In these regions a stepped surface structure with a larger number of different film thicknesses could be observed. During vapor treatment the films started to dewet. The annealing procedure was stopped either after roughly half of the film surface was dewetted or after 7 hours of annealing.

5.3.4 Thin film microdomain structure

We performed in-situ AFM measurements during sample preparation. Details of this experiment are described in chapter 7. Figure 5.5 shows three consecutive AFM phase images taken at approximately $\phi_P \approx 0.7$ and during the drying process of the thin film. Although the phase contrast is rather small in the presence of chloroform, it clearly reveals the microdomain structure of the thin

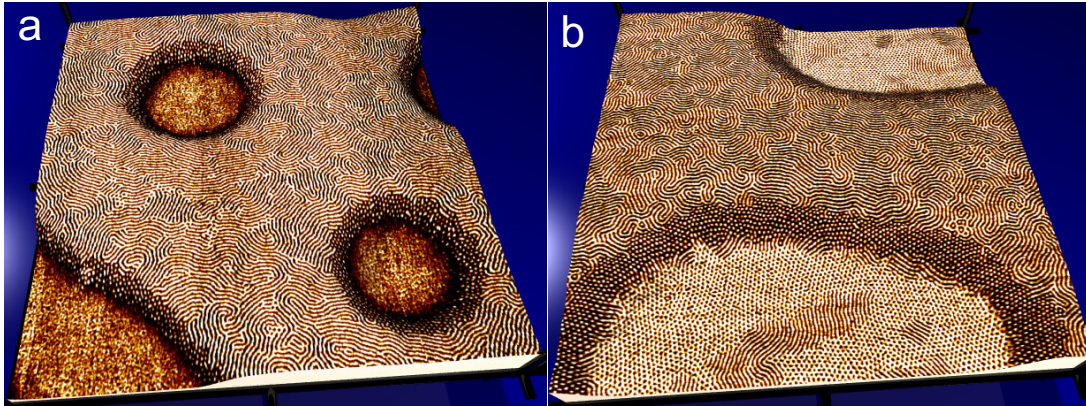


Figure 5.6: 3D rendered SFM images ($5 \times 5 \mu\text{m}^2$) using the height image as height-field and the phase image as texture. The images show the formation of terraces in the film and the systematic change of microdomain structures along the changes in film thickness. a) A film with 11 nm holes and 40 nm thick islands, b) A film with 32 nm holes and 57 nm thick islands.

film. In this case the quench of the microdomain structure is done by switching to a pure N_2 gas flow. White arrows in Figure 5.5 b) mark the position of the tip, when the gas flow has been switched. The strong increase in phase contrast renders the quick drying of the polymer film visible. Figure 5.5 c) was captured after drying of the film and readjustment of the tapping parameters. Comparison of the phase images demonstrates that the drying process does not alter the intrinsic structure of the microdomain pattern.

Figure 5.6 shows two SFM measurements of two samples with different film thickness. The 3D images were rendered with Pov-Ray™ [PT02]. From the SFM height image the shape of the surface is calculated (“heightfield”), while the color information corresponds to the tapping mode phase image (“texture”). The images visualize simultaneously the existence of the terraces and the local microdomain structure in the film. The microdomain structure changes at distinct values of film thickness. In particular, different microdomain structures are found within the holes, at the steps, and on top of the islands.

Figure 5.7 shows 9 SFM tapping mode phase images of annealed films with different polymer concentration and different film thickness: The film thickness increases from bottom to top and the polymer volume fraction ϕ_P increases from left to right. Samples with different initial film thickness around $0.5 c_0$ (bottom row), $1.5 c_0$ (middle row), and $2.5 c_0$ (top row) are shown. On exposure

5 Phase Behavior

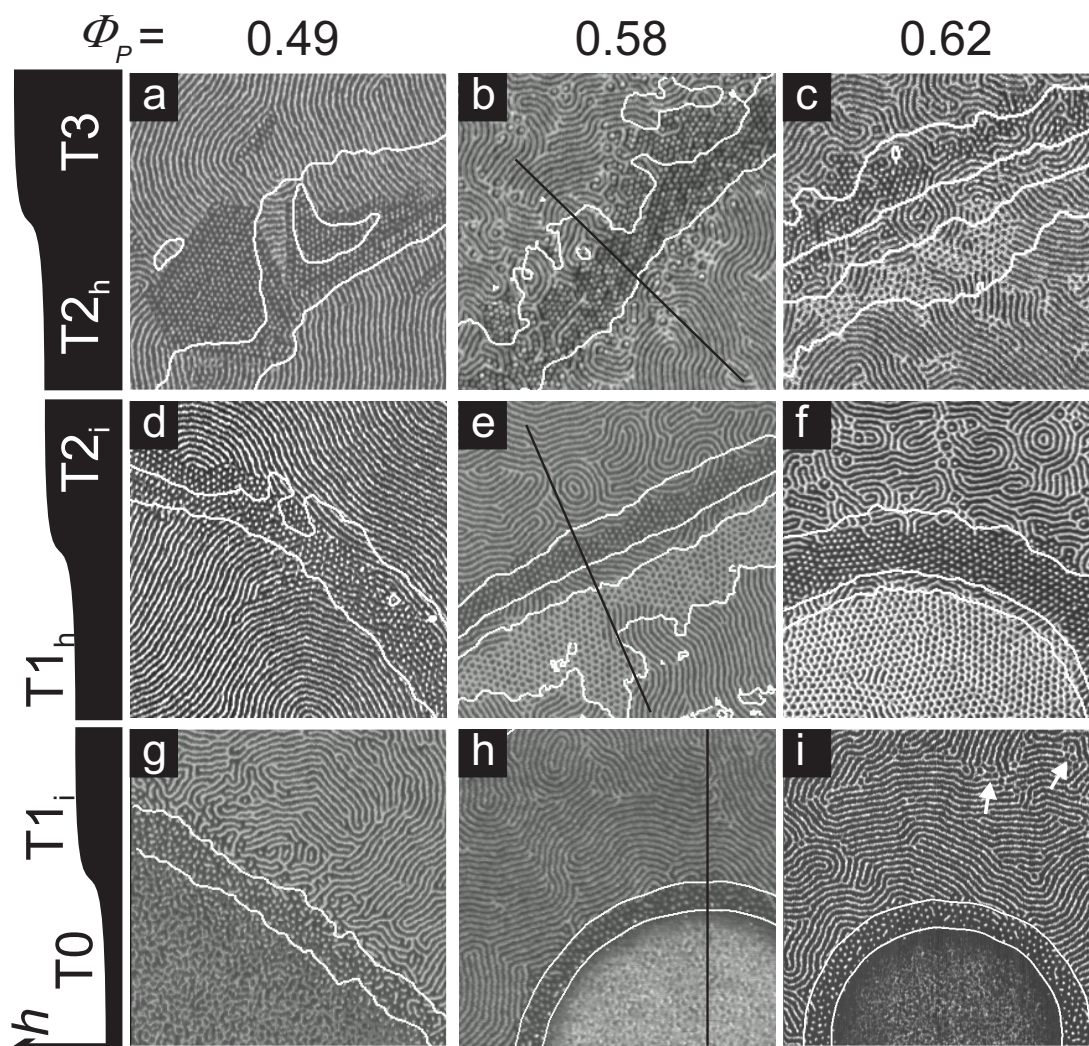


Figure 5.7: SFM phase images at the edges of terraces as a function of film thickness h and polymer concentration ϕ_P . Images are oriented such that the lower terrace is at the bottom in each image. ϕ_P increases from left to right from 0.49, 0.58 to 0.62. From bottom to top the absolute height of the film increases. White lines correspond to contour lines, calculated from the corresponding height images, at which the microdomain structures change. Black lines indicate where the cross sections shown in Figure 5.8 originate.

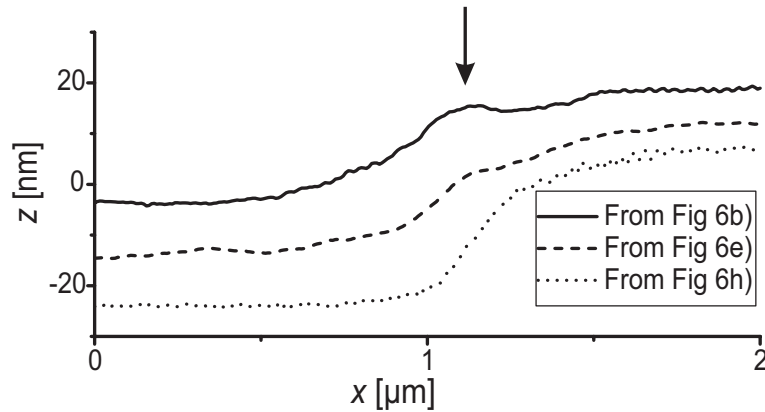


Figure 5.8: Cross sections across terrace steps of the height images corresponding to the dark lines shown in Figure 5.7b, 5.7e, and 5.7h. The thickest film shows a local maximum along the step profile. This is attributed to the fact that the C_{\perp} phase shrinks less than the C_{\parallel} phase during the drying process.

to chloroform vapor, the films form terraces of well defined thickness, which we will refer to as T0, T1, T2, and T3, respectively. See the sketch to the left of Figure 5.7 for the variation of the film thickness and the numbering of the different terraces. The images in Figure 5.7 are oriented such that the lower terrace always lies to the bottom of the image. Thereby, corresponding terraces T_n formed as holes from initially thicker films and as islands from initially thinner films are located next to each other in Figure 5.7. Although their thickness is equal to within the experimental error, we observe different behavior depending on whether a given terrace was formed as a hole or as an island. Therefore we distinguish between T_{nh} and T_{ni}, respectively. All images have a size of $2 \times 2 \mu\text{m}^2$ and were recorded at an arbitrarily chosen edge of islands and holes. Height images are not shown, for they are very similar to the ones used in Figure 5.6. White contour lines calculated from the height images are superimposed onto the phase images. They clearly demonstrate that the boundaries between different structures always appear at a well-defined film thickness. Cross sections of the height image taken along the black lines shown in Figure 5.7b, 5.7e and 5.7h are shown in Figure 5.8.

The images show systematic changes in the microdomain patterns. Four characteristic patterns can be distinguished at the film surfaces: A stripe pattern, which we identify as PS cylinders aligned parallel to the plane of the film (C_{\parallel}), a pattern of hexagonally ordered bright dots originating from perpendicularly

5 Phase Behavior

oriented PS cylinders (C_{\perp}), a pattern of hexagonally ordered dark dots corresponding to a perforated PS lamella (PL), and a rather featureless pattern, which we identify with a disordered phase (dis). The assignment of the surface patterns to three-dimensional microdomain structures is based on results of computer simulations (see below, [Hor02]), on Nanotomography experiments [Mag00, Kon00], and on True Surface measurements (see chapter 3). They will be discussed in more detail below. The terraces of larger thickness usually exhibit C_{\parallel} , which extends over larger areas and has a better long range order at a low polymer concentration. In all images C_{\perp} appears in the regions between holes and islands. At high ϕ_P , PL appears at the rim of the lower terrace $T1_h$, extending over the entire terrace at very high ϕ_P . The lowest terrace shows a disordered pattern (dis). This pattern shows more pronounced lateral features at low ϕ_P .

The contour lines mark the border between different patterns quite accurately. This is particularly the case at low thickness, at the border from C_{\parallel} to C_{\perp} . Figure 5.8 shows three cross sections of the height image corresponding to the black lines displayed in Figure 5.7. The local maximum in the step profile of the C_{\perp} phase at high thickness is attributed to the fact that C_{\perp} has an almost continuous phase of styrene throughout the entire thickness of the film. During drying of the film the PS-rich regions become glassy first, which causes this microdomain structure to shrink less than the other phases. Therefore, height lines do not fit to the border of the pattern in these cases.

With increasing polymer concentration ϕ_P the perforated lamella morphology (PL) appears in thin films within the terraces formed as holes ($T1_h$, $T2_h$). On the terraces of same thickness formed as islands ($T1_i$, $T2_i$) this structure is only rarely observed and merely appears as a characteristic defect in the C_{\parallel} phase (marked with white arrows in Figure 5.7i). At intermediate ϕ_P , the perforated lamellar phase exists only near the edge of the hole. The thickness of these regions is a few nm larger than the thickness in the center of the respective terrace. The area fraction of the PL phase increases with ϕ_P , until the entire terrace $T1_h$ is filled. The finding that PL appears predominantly in holes and at somewhat larger film thickness indicates that the favored thickness of the PL is a few nanometers larger than the one for C_{\parallel} . This is consistent with theoretical results, which predict a few percent increase of the characteristic domain spacing

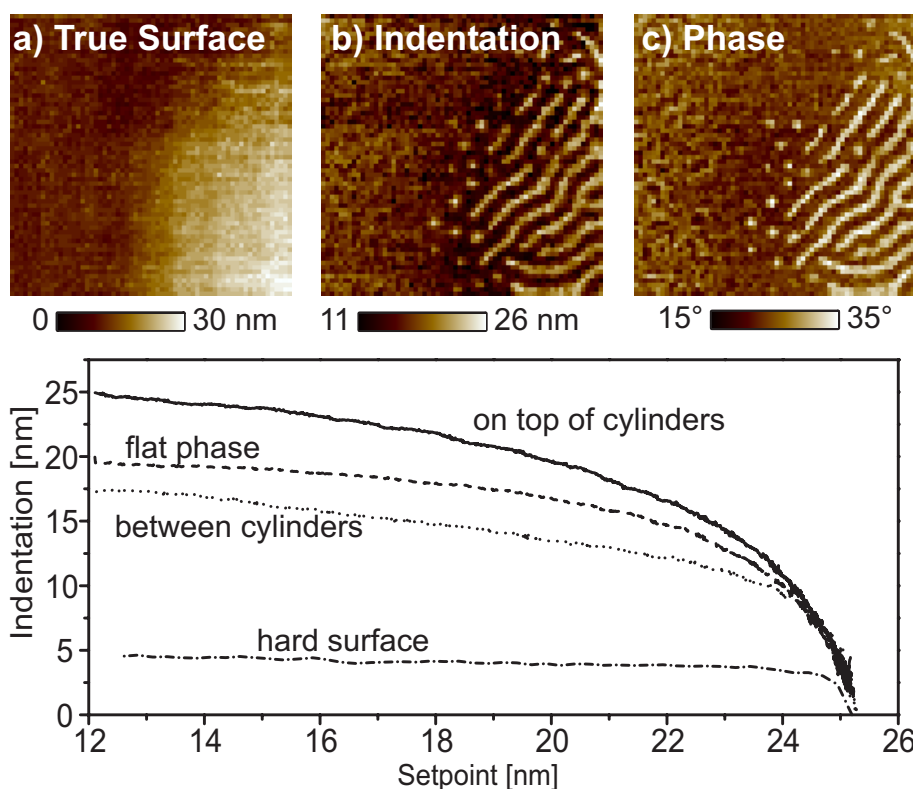


Figure 5.9: True Surface SFM of a thin SBS film. a) Reconstructed True Surface image of a terrace edge. The surface is locally flat with no sign of a lateral structure corresponding to the underlying microdomain structure. b) Indentation image and c) phase image at a relative setpoint of 0.7. The comparison of both images shows that harder regions (less indentation) appear bright in the phase image. d) Averaged Amplitude-Phase-Distance (APD) curves of selected regions in the image. At least 3 curves were averaged. For comparison an APD curve for a hard polymeric surface is shown.

as one moves from cylindrical microdomains through the perforated lamella to the lamella at a given molecular weight [Mat97].

5.3.5 Identification of the microdomain structure

To unambiguously assign the observed patterns found on the film surfaces to distinct microdomain structures, we have identified the origin of the contrast observed in the SFM height and phase images and have measured the position of the true surface (see chapter 3). A laterally resolved array of 64×64 amplitude and phase versus distance (APD) curves was recorded. From each APD curve the z-location of initial contact between tip and surface can be determined. This

5 Phase Behavior

procedure allows to determine the true shape of the surface irrespective of the tip indentation into the soft polymeric material. Moreover, indentation maps and phase images can be calculated from the APD data for any given setpoint A/A_0 . Figure 5.8 shows a true surface image, an indentation image, and a phase image at a setpoint $A/A_0 = 0.7$. The indentation curves in Figure 5.9d) show the indentation as a function of the amplitude setpoint. At the free amplitude of about 30 nm used in the experiments and at lower setpoints ($A/A_0 < 0.95$) repulsive interactions dominate over attractive forces and the indentation is higher on softer materials. Therefore, larger (smaller) indentations are related to soft, PB rich (glassy, PS rich) areas. When we compare the indentation and the phase images, we can clearly show that the brighter regions in the phase image corresponds to the harder material, i.e. to PS rich areas. The True Surface image is virtually flat on top of the terraces and does not reflect the microdomain structure. Together with the relatively large indentations at the given parameters this finding suggests that there is a PB-rich layer of about 10 nm thickness covering the entire sample surface (see (see chapter 3) for details). This result is in agreement with the fact that PB has the lower surface energy of the two components ($\gamma_{PB} = 31$ mN/m, $\gamma_{PS} = 41$ mN/m) [Sto96] and a PB-rich surface layer is thermodynamically stable.

The assignment of surface patterns to distinct phases is corroborated by DDFT simulations of the complete thin film structure. We have used the MESODYN code [Sev99] to simulate a melt of $A_3B_{12}A_3$ “molecules”. Briefly, the block copolymer is modeled as a Gaussian chain with different beads A and B . For the bead-bead interaction potential a Gaussian kernel is used characterized by ε_{AB} . The film interfaces were treated as mask (M) with corresponding bead-mask interaction parameter $\varepsilon_M = \varepsilon_{AM} - \varepsilon_{BM}$. The spatio-temporal evolution of bead densities $\rho_i(\vec{r}, t)$ is obtained using the complete free energy functional $F[\{\rho_i\}]$ and the chemical potentials $\mu_i = \partial F[\{\rho_i\}]/\partial \rho_i$. The Langevin diffusion equation is solved numerically starting from homogenous densities. Appropriate noise is added to the dynamics. We have done simulations with $\varepsilon_{AB} = 6.3, 6.5,$ and 7.1 (in kJ/mol) and varied systematically the strength of the polymer/surface interaction ε_M and the film thickness H . We have used the parametrisation of Ref. [Hui00] and have followed the temporal evolution until no longer significant changes occurred. We chose to model the swollen SBS film as a melt to keep the

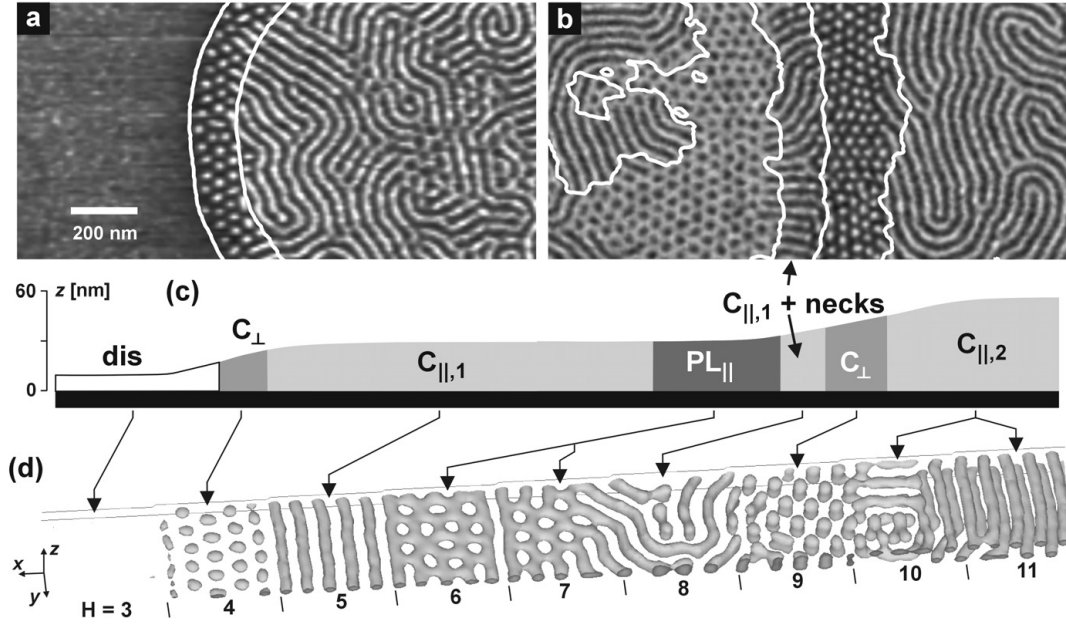


Figure 5.10: (a,b) TM-SFM phase images of thin SBS films on Si substrates after annealing in chloroform vapor at $\tilde{p} = 0.62$. The surface is everywhere covered with a ≈ 10 nm thick PB layer. Bright (dark) corresponds to PS (PB) microdomains below this top PB layer (see chapter 3). Contour lines calculated from the corresponding height images are superimposed. (c) Schematic height profile of the phase images shown in (a,b). (d) Simulation of a $A_3B_{12}A_3$ block copolymer film in *one* large simulation box of $(352 \times 32 \times H(x))$ grid points with increasing film thickness $H(x)$, $\varepsilon_{AB} = 6.5$, and $\varepsilon_M = 6.0$. The latter corresponds to a preferential attraction of B -beads to the surface. The isodensity surface $\rho_A = 0.5$ is shown.

total number of parameters as small as possible. The effect of the non-selective solvent CHCl_3 is modelled as an effective interaction parameter $\varepsilon_M = \varepsilon_M^{\text{melt}} \Phi_P$.

We find that modelling with $\varepsilon_{AB} = 6.5$ matches our experimental data best. Figure 5.10(a) and (b) shows for comparison TM-SFM phase images of two annealed SBS films with different initial film thickness. Both films have formed regions of well-defined film thickness as indicated by the height profile shown in Figure 5.10(c). Figure 5.10(d) shows the result of a simulation done in a wedge-shaped geometry. It exhibits exactly the same sequence of phases as the experimental data. Starting from a disordered phase (dis) for $H = 3$ grid units, spheres or very short upright cylinders, C_{\perp} , form ($H = 4$). These are followed by parallel cylinders, $C_{\parallel,1}$ ($H = 5$), a perforated lamella, PL ($H = 6$), a PL co-existing with $C_{\parallel,1}$ ($H = 7$), cylinders with ripples or necks ($H = 8$), then upright

5 Phase Behavior

cylinders, C_{\perp} ($H = 9$), and two layers of parallel cylinders, $C_{\parallel,2}$ ($H = 10, 11$, and 12). The film thickness at which phase transitions occur as well as the relative domain spacings are correctly predicted. The distance between next-nearest holes of the PL is found to be 1.15 times larger than the distance between next-nearest cylinders, $a_0 = 7.0 \pm 0.5$ grid units, of the C_{\parallel} and C_{\perp} phase. We also observe this in our experiments [Figure 5.10(b)].

In summary, we can unambiguously identify the microdomain phases: From the SAXS and the Nanotomography experiments [Mag00] we know that SBS forms hexagonally ordered cylinders in bulk and in thick films, respectively. The True Surface measurements allow us to identify the PS microdomains as bright structures in the phase images. They show further that the sample surface is covered by a PB layer of about 10 nm thickness. Additionally we can compare these results with recent calculations based on dynamic density functional theory (DDFT) using the MesoDyn code, which are discussed in more detail in [Hor02]. The excellent agreement between simulation and experimental results strongly corroborates the following identification of the microdomain structure: C_{\parallel} corresponds to PS-rich cylinders (bright) in a PB-rich matrix oriented parallel to the surface, C_{\perp} corresponds to cylinders oriented perpendicular to the surface (bright dots), and PL corresponds to a perforated PS lamella oriented parallel to the surface (bright continuous structure perforated by dark dots). The featureless pattern dis could either be attributed to a wetting layer (half lamella) or to a disordered phase, where microphase separation is suppressed by confinement of the material.

An interesting detail of the microdomain structure is seen between the first layer of cylinders and the C_{\perp} phase. Here the cylinders show undulations, which makes it difficult to define unambiguously the border between lines and dots in the phase images. We identify this structure as “cylinders with necks”, which have been found before in the same system [Kon00] and can also be found in the DDFT simulations [Hor02].

5.3.6 Phase diagram

We construct a phase diagram by plotting the observed phases as a function of the film thickness and the polymer concentration in the films. To localize the boundaries between phases occurring at different film thickness, we determine

the absolute values of the film thickness at the contour lines in the SFM images, where the lateral phase boundaries are located. To measure the absolute thickness of any given terrace a scratch was applied to the film with either a needle or a scalpel. Then a smooth edge of the scratch was chosen using an optical microscope and the step height was measured with SFM. Scan sizes between 5×5 and $20 \times 20 \mu\text{m}^2$ were chosen. Background subtraction was done by fitting a plane to the area in the image, where the bare silicon substrate is exposed. Close to the scratch, images with smaller scan sizes (between 3×3 and $5 \times 5 \mu\text{m}^2$) were taken at steps of the terraces to measure the existing microdomain phase patterns and their height relative to the terraces. Height histograms were calculated from the height images and background subtraction was optimized by maximizing the peaks in the height histogram. The lower peak was then taken as a reference and the relative heights were added to the absolute height of the corresponding lower terrace. By this procedure we determined the absolute heights h_{dry} of the different regions of the films after solvent extraction.

In order to account for the fact that the observed microdomain structures are formed in the swollen films, we calculate the thickness in the swollen state, $h_{wet} = h_{dry}/\phi_P$, from h_{dry} as determined above and the polymer volume fraction ϕ_P as determined with ellipsometry.

The results are presented in Figure 5.11 showing both, the heights at which terraces form and the heights at which microdomain structures change. The heights of the terraces scale approximately with $\phi_P^{0.6}$, which is indicated by the solid lines in the diagram. This scaling is stronger in ϕ_P than what is found for the scaling of lattice parameters of bulk solutions [Han98, Has83, Lod95].

At very small film thicknesses we observe a disordered surface structure. We note that the height difference measured between the substrate and the first layer of cylinders (T1) amounts to about 60 nm, which appears very large for a single layer of cylinders with lateral spacing of about 40 nm. This finding indicates that the polymer layer found in the regions of smallest film thickness may extend over the entire substrate surface with the layers observed in thicker films being placed on top. Figure 5.12 shows the film thicknesses h_T of terraces formed the rim of the sample for $\phi_P = 0.62$. h_T increases approximately linearly with the number of terraces as shown by the linear fit of the data with terrace number > 0 (solid line). The data point given at terrace number 0 represents the thickness of the

5 Phase Behavior

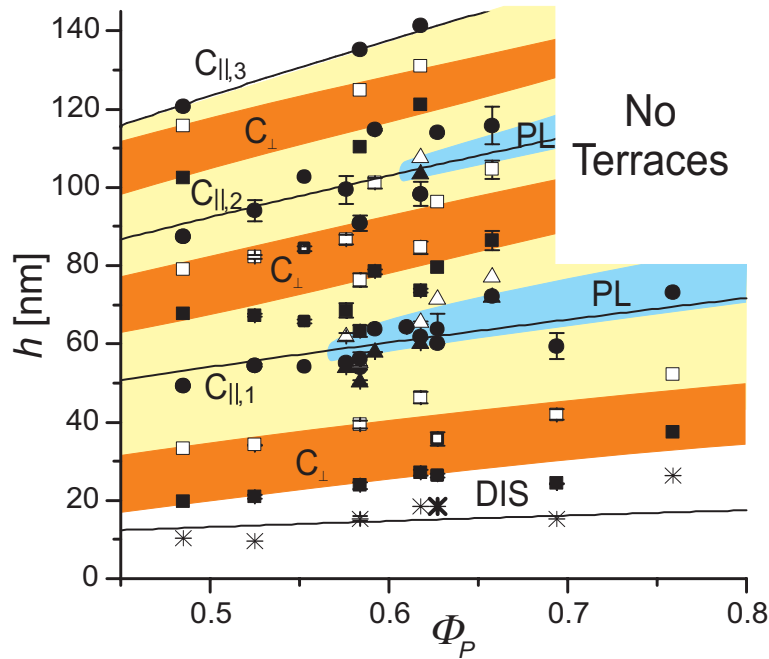


Figure 5.11: Phase diagram of observed surface structures. Solid lines correspond to functions $d = A\phi_P^{0.6}$, with $A = 20, 82, 140$ and 187 nm representing the thickness of the terraces. Data are given for equilibrium film thicknesses of $C_{||}$ (●) and “dis” (*) and for upper and lower bounds (open and closed symbols, respectively) of C_{\perp} (□, ■) and PL (△, ▲) phases. The latter correspond to the height at contour lines such as those shown in Figure 5.7. All lines and areas are drawn to guide the eye.

wetting layer. From the linear fit we determine a mean thickness of a cylinder layer c_0 to be $c_0 = 35 \pm 2$ nm, which fits well to the measured distance of in plane cylinders of about 39 nm. The linear fit suggests also an additional layer of material underneath the film of thickness $h_0 = 27 \pm 5$ nm, which corroborates the existence of a wetting layer everywhere at the film-substrate interface. This value is somewhat larger than the thickness of the “dis” phase of 18 ± 5 nm but also considerable smaller than c_0 .

5.4 Discussion

Sample preparation in a controlled environment of solvent vapor gives additional insight into the phase behavior of thin block copolymer films. The volatile solvent chloroform is nonselective and merely enhances the mobility of polymer molecules

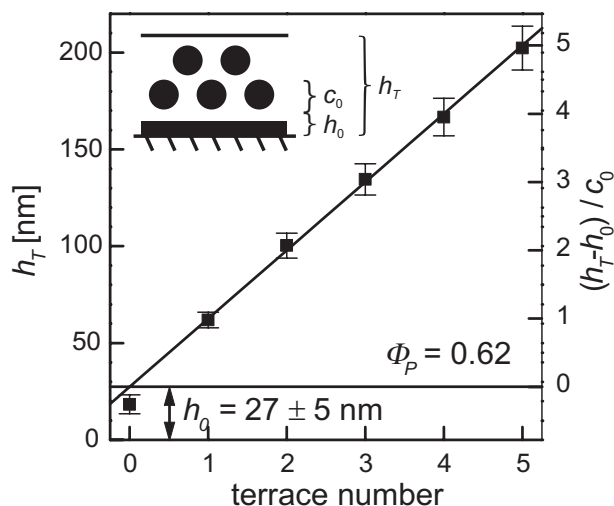


Figure 5.12: Terrace height h_T and relative thickness of a cylinder layer $(h_T - h_0)/c_0$ as a function of terrace number, where c_0 denotes the natural layer thickness. The heights increase approximately linearly with the number of cylinder layers in the film. The offset h_0 of the plot at terrace number 0 corroborates the existence of a wetting layer with thickness h_0 underneath all films. The inset shows a sketch of this situation.

in the system. Its high volatility enables us to quench the microdomain structure, which has developed during annealing. The control of the polymer concentration ϕ_P allows us to vary the effective interactions between the two components and between the two components and the boundary surfaces.

The polymer concentration ϕ_P was chosen high enough that the block copolymer solutions were microphase separated in all experiments. The SAXS results, the formation of terraces even in the most diluted films and the in-situ observation of the microdomain structure corroborate this assumption. Note that this is very different from experiments done by Kim et al. [Kim98, Kim98a], who used the dynamics of solvent evaporation to control the resulting microdomain structure in their thin film. The key difference is that Kim et al. started solvent extraction from the one-phase region. Therefore structure formation took place during the drying process only and is largely influenced by the evaporation rate. Our system in contrast is well phase separated before drying and the dynamics of the polymers is too slow to follow the sudden quench of the system.

In all but the thinnest regions of the films, cylinders oriented parallel to the plane of the film (C_{\parallel}) dominate the SFM images. The parallel alignment of the cylinders is favored over the perpendicular orientation because of the preferential

5 Phase Behavior

attraction of PB to the surface and a penalty for the additional unfavorable interfaces occurring at the ends of the upright cylinders. As a result, terraces with a thickness corresponding to an integer multiple of the cylinder layer spacing form spontaneously. This behavior is well known from lamella forming systems where the lamellae tend to orient parallel to the plane of the film and the local film thickness adjusts to a well-defined multiple of the lamellar spacing [Cou89].

In between neighboring terraces exhibiting parallel oriented cylinders we find regions where the cylinders are oriented perpendicular to the plane of the film. We anticipate that the formation of upright cylinders is energetically favorable over a compression or stretching of the parallel structures to a thickness significantly deviating from an integer multiple of the natural layer thickness. This notion is corroborated by the DDFIT simulation results [Kno02, Hor02], which also predict the formation of upright cylinders as a stable thin film structure at intermediate film thickness. We note that the slope across the edges between neighboring terraces appears highly exaggerated in the SFM height images (Figure 5.6). This slope is determined by an interplay of the surface tension and the energetic penalty of creating a film with an unfavorable film thickness. While this penalty should decrease with increasing dilution of the polymer, the surface tension should be only moderately affected, since this value is similar for the solvent and the polymer. The use of solvent in this way reduces the slope across the edges and stabilizes the non favorable microdomain structure C_{\perp} . In fact, the maximum slope amounts to only some 5° in the thinnest films between T0 and T1 and 3° between terrace T1 and T2. Over a lateral distance of a single cylinder diameter the film thickness varies therefore at most about 3 nm. Therefore, we may safely exclude the gradient in film thickness as an important driving force for the formation of upright cylinders.

A perforated lamella (PL) is found at high polymer concentrations and at a film thickness close to one or two layers of cylinders. The natural thickness of the PL phase seems to be somewhat larger than the one of the C_{\parallel} phase, since it appears at the rim of holes at intermediate polymer concentrations. We emphasize that the perforated lamella is not a stable bulk structure of the SBS material, but it is induced by the presence of the two boundary surfaces. Both, the planar symmetry of the boundary surfaces and their preference to the majority (PB) phase lead to the stabilization of a “non-bulk structure”, also referred to as a

“surface reconstruction” [Reh01]. Simulation results show that the surface field favors accumulation of PB at the homogeneous surfaces of the film, thereby depleting the center of the film of the majority phase [Hor02]. As a consequence, the PS density increases in this portion of the film, leading to the formation of a continuous PS structure perforated by isolated PB channels. DDFT simulation results predict [Kno02, Hor02] that an even stronger surface field eventually should lead to the formation of a complete PS lamella in the center of the film. In our experiments, however, this effect was not observed. This is probably due to the fact that the experimentally accessible surface fields are limited in our system and cannot exceed the surface field of SBS without solvent.

We find that for thicker films (T_{2h}) the PL phase appears only at the highest polymer concentrations ϕ_P (see also Figure 5.11). This supports the DDFT simulation results of Horvat et al. [Hor02] and can be interpreted in the following way. The solvent is expected to screen the interactions both between the two polymeric components and at the interfaces, higher polymer concentrations correspond to a stronger surface field. Therefore, the effective surface field acting on the topmost layer of the film is stronger in thinner films. This finding indicates that the two surface fields of both confining surfaces exhibit a characteristic decay length of the order of a microdomain spacing [Hui00]. In thin enough films the effects of both surfaces can add and thereby stabilize the PL structure already at lower polymer concentrations.

We note that the PL phase was observed before in the bulk [Kha95, Foe94] as well as in thin films [Rad96]. While in bulk the PL is considered to be metastable [Haj97], both, our experiments and the DDFT simulations [Kno02, Hor02], indicate that the existence of one or two planar interfaces preferentially attracting the majority phase stabilizes this structure.

At a film thickness below about one fourth of the cylinder-cylinder distance, we observe in terrace T0 a grainy, disordered surface structure. We may offer two explanations for the nature of this layer and terrace T0: Either it consists of strongly adsorbed polymers, in which molecules are pinned to the substrate and their mobility is too low to rearrange during solvent vapor annealing [Har00]. The other possibility is the presence of a wetting layer or a half lamella as reported by Karim et al. [Kar93], which would imply that the SiO_x surface preferentially attracts PS.

5 Phase Behavior

The existence of an adsorbed layer or a wetting layer has implications regarding the surface field acting on the remaining copolymer film. Given the copolymer composition of $f_{PB} = 0.74$, any adsorbed layer will exhibit preferential attraction to PB. Similarly a wetting layer will form such that PS is located close to the substrate exposing PB to the inside of the film. Such a layer would also exhibit preferential attraction to PB for the rest of the film. Since the free surface of the film preferentially attracts PB, corresponding to the lower surface energy of PB (see above), qualitatively symmetric boundary conditions are established. The excellent agreement between the experimental results and the DDFT simulations performed with symmetric boundary surfaces (see below, [Kno02, Hor02]) corroborates this conclusion. However, the strength of the surface field can not be expected to be equal at the free surface and at the film-substrate interface.

The DDFT simulations [Kno02, Hor02] predict a disordered phase for the thinnest films. For a strong preference of the minority block to the surfaces, a wetting layer is predicted. As chain adsorption onto the boundary surfaces is NOT captured by the simulations, however, a direct comparison between experiment and simulations seems questionable in this thickness regime. Also taking into account two dissimilar interfaces is probably essential to model such very thin films. For an in-depth discussion of the microdomain structure of the thinnest films, we refer to Refs. [Hor02] and [Lya03].

5.5 Conclusion

We have studied the phase behavior in thin films of a SBS block copolymers swollen in chloroform vapor. Both, the film thickness h_{wet} and the polymer volume fraction ϕ_P were varied and a phase diagram of surface structures was established.

- The variation of ϕ_P can be interpreted as a variation of the molecular interactions between the two polymer components and between the components and the boundary surfaces.
- The surface field causes cylinders to align parallel to the plane of the film, whenever the thickness fits an integer multiple of cylinder layers. At intermediate thickness the cylinders align perpendicular to the film plane. At

5.5 Conclusion

higher polymer concentration, i.e., at stronger surface fields, a perforated lamella (PL) of PS forms. The surface field needed for PL formation increases with increasing film thickness. This corroborates simulation results that indicate a decay length of the surface field of about one microdomain spacing [Hui01, Hui00, Kno02, Hor02].

- A wetting layer exists underneath all films, which either consists of pinned molecules or of a half lamella.
- The experimental results are in excellent agreement with computer simulations based on dynamic density functional theory [Kno02, Hor02].

Both the experimental findings and the computer simulations indicate that the phase behavior of thin block copolymer films is governed by an interplay between surface fields and confinement effects. The preferential attraction of one of the two blocks to the surface (the surface field) can induce alignment as well as structural changes in the near-surface regions, so-called surface reconstructions. Confinement to a particular film thickness may imply compression / stretching of the respective structures, which involves additional entropic contributions to the free energy of the system. The interplay between both effects defines the existence range of the respective microdomain structures.

5 Phase Behavior

6 Principal Dimensions of the Microdomain Structure in Thin Films of Cylinder-Forming Block Copolymers

In this chapter we study the principal dimensions of the microdomain structure in thin films of a polystyrene-*block*-polybutadiene-*block*-polystyrene (SBS) triblock copolymer. A image analysis algorithm permits the recognition of individual structures, phase boundaries and defects from the phase contrast scanning force microscopy (SFM) images. The determination of the local orientation, curvature and spacing of the microdomain structure yields rich information about the physics of thin block copolymer films: The quality of ordering in the thin films can be quantified by evaluating the orientational correlation function. An increase in the local curvature of in plane lying cylinders leads to an increase in their microdomain spacing, which can be explained by simple geometric arguments. The information about the microdomain spacing of all structures is correlated with the local thickness of the polymer thin film and compared to the bulk cylinder spacing. The results are compared to the predictions made by the strong segregation theory presented in chapter 4. Deformations induced by the planar nature of the surface/interface and by the incommensurability of the microdomain structure to the local film thickness result in systematic variations of the lateral cylinder spacing.

6 Principal Dimensions of the Microdomain Structure

6.1 Introduction

Thin films of lamella forming block copolymers have been studied extensively, for reviews see [Bin99][Mat98][Fas01]. In the case of thin supported films the lamellae tend to align parallel to the substrate [Ana89][Rus89][Cou89][Fos92] forming holes and islands with thickness $n L_0$, if both surfaces attract the same block and $(n + 1/2) L_0$ otherwise, where L_0 is the bulk lamellar spacing. No measurable deviations between the lamellar spacing in a terraced thin film and the one in bulk have been found [Ana89][Sik93][Gad99]. In films confined by two rigid interfaces of the same type the block copolymer has to adapt its geometry to the film thickness if the latter is not commensurate to L_0 . In the case of strong interactions it satisfies this constraint by adapting a new lamellar spacing L , which is commensurate to the film thickness [Lam94]. In the case of weak or reduced interactions [Kel96] and an incommensurable film thickness the lamellae tend to orient perpendicular to the surface.

These findings have been confirmed and explained by theoretical studies. For a thin film of a diblock copolymer with bulk lamellar phase the excess surface free energy per unit area has to be evaluated. This quantity has been studied by self consistent field theory methods [Shu92, Mat97], by strong segregation calculations [Mat97, Sem85] and by density functional theory [Fri02]. The minima in the excess free energy per unit area appear at film thicknesses, which are separated by the bulk lamellar spacing L_0 . Only the first minima might appear at a slightly different thickness due to packing effects close to the surface [Fri02]. Additionally all minima have the same excess free energy offset determined by an additional configurational entropy of the chains plus the surface energy of the block at the surface. The two equilibrium film thicknesses of islands and holes in a thin supported film have to be determined by a common tangent method of two neighboring minima in the excess free energy plot. Thus the theory supports the experimental results of film thicknesses very close to an integer multiple of the bulk lamellar spacing.

The situation is more complex in the case of block copolymers forming phases other than lamella. In these systems strong interactions induce a transition to other structures close to the interfaces. This was first seen by Karim et al. [Kar93] for a system of hexagonally ordered cylinders in bulk, which formed a half lamella at an interface preferring the minority component. A similar transitions

to a perforated lamellar phase [Rad96] was found in a free standing film in the case of attraction of the majority component to the surfaces. For a summary of experimental findings see [Wan01]. This behavior has been reproduced with the help of various theoretical techniques [Tur94, Bro94, Wan01, Hui00, Hui01]. Additional effects found experimentally are similar to the hybrid structures for lamellar phases and include spheres on top of a perforated lamella [Har98] and cylinders with necks [Kon00].

In the case of weak surface interactions no structural transitions take place and there is a similar effect of film thickness and surface interaction on the orientation of hexagonally ordered cylinders as in the lamellar case. For small repulsive surface interactions of the B block the cylinders orient parallel to the interfaces, terminating with half cylinders at the interface $C_{\parallel}^{1/2}$ [Wan01, Per01, Kim01], while they orient perpendicular C_{\perp} for very weak attractive interactions to the B block. If this attraction becomes stronger the cylinders orient parallel again with the B block covering the surfaces C_{\parallel} . The parallel phases are stable around film thicknesses, which form as terraces in a thin film. This behavior was also found in the strong segregation calculations presented in chapter 4. This calculation predicts that the equilibrium film thickness of an island or hole for the C_{\parallel} structure does not coincide exactly with multiples of the bulk spacing of cylinder layers $\sqrt{3}/2L_0$. The reason is a deformation of the hexagonal unit cell at the interfaces due to their planarity. The thickness range of a stable parallel structure is predicted to increase with increasing attraction of one of the blocks to the interfaces in comparison to perpendicular oriented cylinders.

In chapter 5 we established a thin film phase diagram of a SBS/chloroform system, which exhibits a microdomain structure of hexagonally ordered cylinders in bulk. We found that the cylinders show different orientation depending on the film thickness and may even reconstruct to a disordered structure at a very thin film thickness or to a perforated lamellar (PL) structure at polymer concentrations. Since all these structures are formed by identical molecules, it seems interesting to investigate lateral and orientational details of the different structures and to compare them. The Metrology AFM enables us to measure reliably the lateral distances and angles within the microdomain structure of the thin films.

In this chapter we discuss the principal dimensions of the microdomain struc-

6 Principal Dimensions of the Microdomain Structure

tures formed in the SBS/chloroform system. A new image analysis algorithm analyzes the details of the respective structures. It determines not only the local spacing of the microdomains in all structures with lateral features, but also measures the local orientation of the lattice sites. This analysis together with the local thickness information of the thin film from the AFM height image enables us to study distinct effects of the film thickness and the local structure on the local spacings of the different microdomain structures.

6.2 Experimental

6.2.1 Materials

We have studied thin films of a polystyrene-*b*-polybutadiene-*b*-polystyrene (SBS) Copolymer with molecular weights $M_{w,PS} = 14$ kg/mol, $M_{w,PB} = 73$ kg/mol, and $M_{w,PS} = 15$ kg/mol (PS is polystyrene, PB is polybutadiene). The Polymer was obtained from Polymer Source Inc. Taking into account the densities of the homopolymers (1.05 g/cm³ for PS and 0.93 g/cm³ for PB) [Bra89] the volume fraction of PS is $f_{PS} = 0.26$. Silicon substrates were cut from wafers, cleaned in fresh 1 : 1 H₂SO₄ (conc.)/H₂O₂ (30%) solution, thoroughly rinsed in boiling and cold Millipore water and additionally cleaned by a Snowjet.

6.2.2 Preparation

Thin films of SBS were prepared by spin casting dilute toluene solutions onto silicon substrates. To equilibrate the samples they were subjected to a controlled solvent vapor atmosphere of chloroform. The procedure of vapor treatment has been described in chapter 5: Two gas flows are mixed, one saturated by Chloroform vapor, the other pure N₂ or dried air. The amount of volume flow of the two gas flows then determines the vapor pressure of chloroform relative to its saturated vapor. After sufficient treatment the microdomain structure is quenched via fast solvent removal by switching to pure N₂/air flow.

6.2.3 SFM

The microdomain structures at the surface of the dry films were studied using a Dimension 3100 Metrology SFM from Digital Instruments, Veeco Metrology Group and a Nanoscope III controller. The metrology system uses a hardware linearized piezo scanner, which allows a reliable and quantitative measurement of lateral dimensions and heights from the images. The instrument was operated in Tapping Mode SFM. Olympus and Nanosensors Tapping Mode cantilevers were used (spring constant 40 N/m, resonance frequency ranging from 200 to 300 kHz). All measurements were performed at free amplitudes of about 30-50 nm and a relative setpoint of about 0.95.

6.3 Results and Discussion

One way often found in literature to measure periodic distances in an image is to Fourier analyze the image. Nevertheless, this procedure only gives average information about the distribution of periodic structures in the image. Since we want to evaluate the microdomain spacings of different structures from the AFM phase images separately, we need a tool to distinguish them and measure distances only for selected structures. Therefore we establish an image analysis algorithm, which not only recognizes the structures and measures their lateral microdomain spacing, but is also capable of obtaining the local director of any structure and the local curvature of the in plane lying cylinders. This algorithm is explained in detail in the appendix. It determines specific points in all the morphologies, i.e. connected points along the center of the cylinders in C_{\parallel} and isolated points at the center of the respective unit cell for the structures PL and C_{\perp} . Then for every point the neighboring points are analyzed. The point is only accepted as a regular point, if it fulfills certain criteria outlined in the appendix. The analysis of the neighbors gives access to the local director of the structure and to the distances to its nearest neighbors. For further reference we assign the letters $L_{C_{\parallel}}$, $L_{C_{\perp}}$ and L_{PL} to the lateral microdomain spacings of the structures C_{\parallel} , C_{\perp} and PL, respectively. Additionally we can use the AFM height image to correlate measured features with the local film thickness of the SBS film.

As an example Figure 6.1 a) shows an AFM Phase image of an SBS film with thickness between one and two layers of cylinders. The respective terraces are

6 Principal Dimensions of the Microdomain Structure

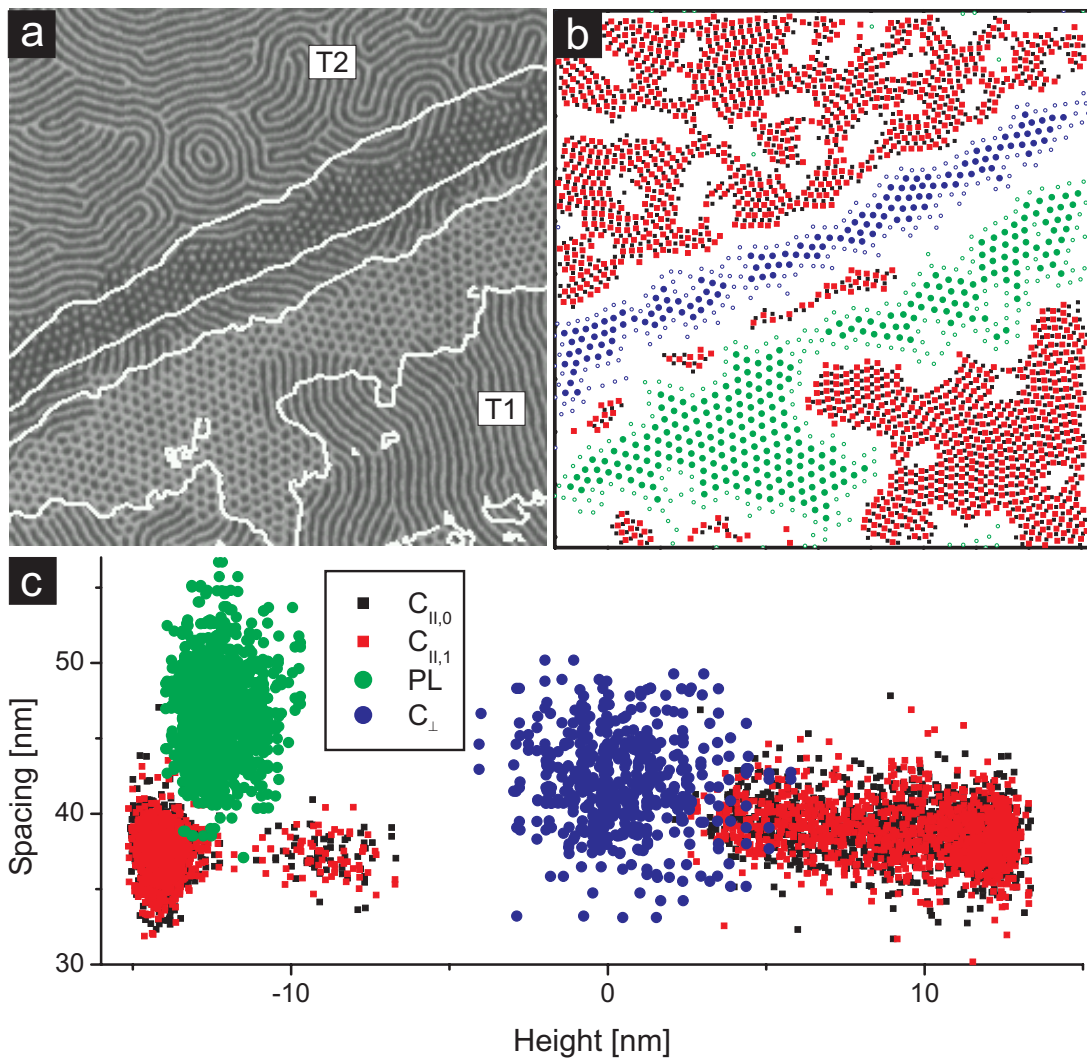


Figure 6.1: a) Phase image of a SBS film with thickness between one (T1) and two layers of cylinders (T2). White lines correspond to contour lines of constant height in the SFM height image. b) Result of the image analysis: For the structures PL and C_{\perp} green and blue points are drawn at the center of structures. Accepted and rejected cells are shown with full and open symbols, respectively. For the C_{\parallel} structure only accepted points along the cylinders are shown in black and red for better visibility. The indices 0 and 1 denote the data for white and black stripes in the phase image, respectively. Note that defects in the structures are avoided. c) Distribution of the local microdomain spacings for the respective structures versus the local height in the AFM height image.

called T1 and T2. The white lines in the image correspond to contour lines of the AFM height image. The image shows all four structures with lateral features found in this system (see chapter 5). The lower half of the image represents a film thickness of a single cylinder layer. It shows stripe-like patterns corresponding to the C_{\parallel} phase and a pattern of dark dots corresponding to the PL phase. The upper terrace in the upper half of the image shows only the C_{\parallel} structure. At the step between the terraces we find a structure of bright dots, which we identified as C_{\perp} phase.

Figure 6.1 b) shows the points determined by the image analysis algorithm for this image. The comparison shows that the structures are very well recognized by the software. Furthermore defects and boundaries to other structures are avoided to exclude possible distortions induced by the defects. The raw distribution of distances measured in this image as a function of the relative height is shown in Figure 6.1 c). At high and low heights the C_{\parallel} structure is dominating, since those heights represent the terraces. We find the PL cloud close to the first terrace and the C_{\perp} cloud at intermediate heights. The gap at -5 nm can be explained by the fact that the points determined for the C_{\perp} phase lie in the center of polystyrene rich areas, which often appear elevated in the AFM height images. This artefact is induced by the chosen tapping conditions and has been discussed in chapter

efTS. The distributions of the point like structures C_{\perp} and PL have bigger standard deviations than the distribution of the C_{\parallel} structure. This can be seen for all polymer concentrations and is attributed to the fact that the point-like structures have freedom to fluctuate in all directions in the plane of the film. For the C_{\parallel} structure only the projection of fluctuations around the cylinder axis to the plane of the film is evaluated.

Having information about the local director, and the local distances inside the structures, it is possible to extract information about the correlation length of each structure and the dependence of the local spacing from the local curvature. Furthermore we can compare the microdomain spacing of different structures throughout the thin film phase diagram shown in chapter 5.

6.3.1 Orientational Correlation of the C_{\parallel} Structure

As a first result we want to present the evaluation of the correlation length of the C_{\parallel} structure from the image analysis. In principle the evaluation of the

6 Principal Dimensions of the Microdomain Structure

correlation length could be done for all structures, nevertheless it becomes very unprecise for other structures than C_{\parallel} because of their narrow existence area in the images.

Figure 6.2 shows two examples of the distribution of angles and distances in the AFM phase images. The analyzed structures of a film prepared at low and medium polymer concentration is shown in Figure 6.2 a) and 6.2 b), respectively. Below those images the distribution of the angles is shown in Figure 6.2 c) and 6.2 d) and of the distances in Figure 6.2 e) and 6.2 f). To establish a filled color coded image from the discrete points found by the algorithm, a Gaussian filter with a width comparable to the distance of points is applied. Thus every pixel in the images 6.2 a) to 6.2 d) represents an average over the distance/angle distribution of the nearest lying points. A similar procedure was used by Harrison et al in ref. [Har99]. The angular distributions make the domain size of the different structures clearly visible. Areas with uniform color have the same direction and therefore represent single domains. The dot-like structures C_{\perp} and PL exhibit angles ranging from 0 to 60 degrees, and appear therefore mainly red in the images. Comparing the results for low and high polymer concentration, Figure 6.2 c) and 6.2 d), respectively, it becomes clear that the average domain size for the C_{\parallel} structure is larger for the film prepared at lower polymer concentration. The shape of the domains in this phase is not circular but rather rectangular. All rectangles of a given color are extended in the same direction, perpendicular to the local director of the cylinders.

The distribution of the distances for the sample prepared at low polymer concentration shown in Figure 6.2 e) appears very homogeneous for all the structures. The sample prepared at higher polymer concentration in contrary shows distinct distances for different structures. The PL structure has the highest spacing of all structures. The upright cylinders show intermediate spacing and the lying cylinders have the lowest spacing. If one looks closely at the lying cylinders on top of the first and the second terrace one recognizes that the spacing on the higher terrace is a little larger than on the lower terrace. We come back to this point later in this chapter.

To quantify an average size of the domains in the C_{\parallel} structure we determine the correlation length of the individual structures by evaluating the orientational correlation function. A similar approach is described in [Har02] for a similar

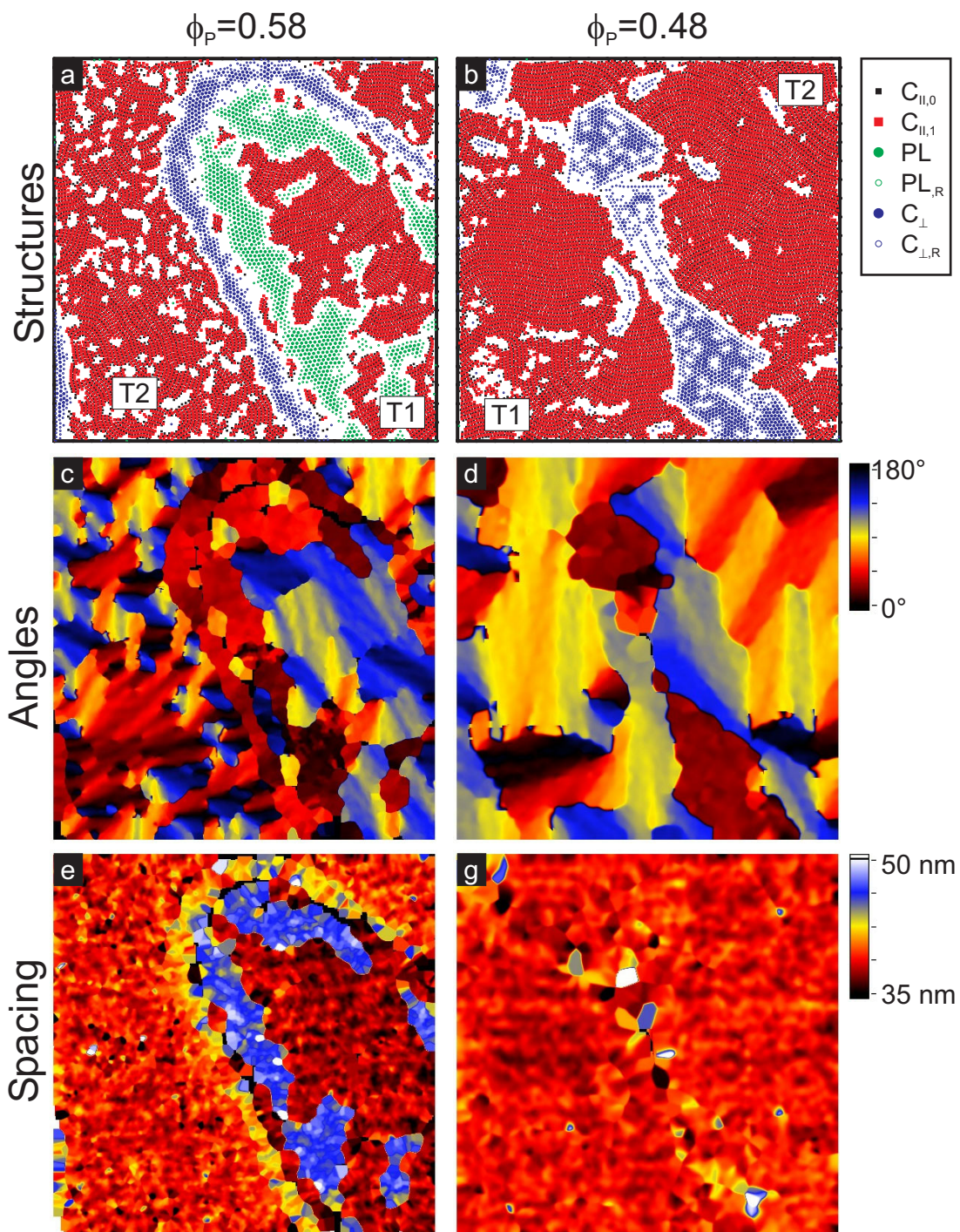


Figure 6.2: Results of the image analysis algorithm for two AFM phase images for samples prepared at $\phi_P = 0.58$ (left) and at $\phi_P = 0.48$ (right). The top two images a) and b) show the recognized structures PL, C_{\perp} and C_{\parallel} . Images c) and d) show the distribution of angles. The filling of the area is done by applying a gaussian filter as described in the text. Images e) and f) show the distribution of the lateral microdomain spacings for all structures.

6 Principal Dimensions of the Microdomain Structure

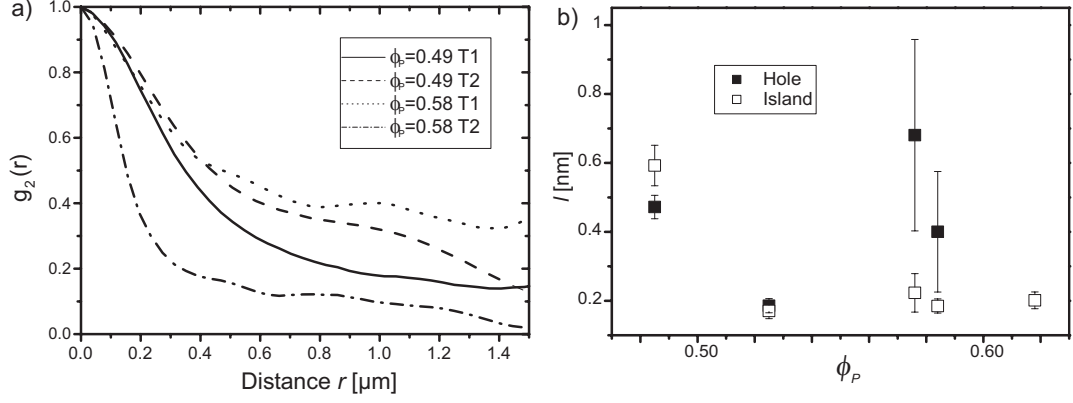


Figure 6.3: a) Orientational correlation functions for the two samples show in Figure 6.1 separated for the two terraces of the samples denoted by T1 and T2. b) Averaged correlation lengths as a function of the polymer content of the thin film.

block copolymer system and in [Str96] for the persistence of a polymeric chain. We first define a continuous order parameter field $\psi(\vec{r})$ as

$$\psi(\vec{r}) = \exp[2i\theta(\vec{r})], \quad (6.1)$$

where $\theta(\vec{r})$ is the local direction of the cylinders. The correlation function $g_2(r)$ is then computed directly from correlation pairs as

$$g_2(r) := \langle \psi(\vec{0})\psi(\vec{r}) \rangle, \quad (6.2)$$

where the brackets indicate an average over all points in one image. The correlation length l is then determined by the integral width of the correlation function $g_2(r)$.

Figure 6.3 a) shows the correlation function for the $C_{||}$ structure in the lower and the higher terrace of the two phase images shown in Figure 6.3. The correlation function is expected to decrease monotonous to zero for large distances r . Since the images have only finite size and the $C_{||}$ structure extends only over a finite range, the resulting correlation functions for well aligned systems will not reach zero within accessible distances r . Additionally the curves shown in Figure 6.3 exhibit shoulders to the right of the main peak. This may be due to the non circular shapes of the domains as mentioned above. In order to quantify

6.3 Results and Discussion

the correlation length in spite of these difficulties, we used two methods: We determined an approximate integral width by setting a threshold by eye where we end the integration. The second method is to fit the first slope of the function with an exponential decay, where the decay length corresponds to the correlation length.

The dependence of the correlation length from the polymer concentration is shown in Figure 6.3b). Plotted is the average value of both procedures where the error bars are given by the difference of the two measures. We see the same trend as already discussed above: The film prepared at low polymer concentration shows larger correlation lengths than the one prepared at medium polymer concentration. This holds for the upper terrace, which shows only C_{\parallel} in both experiments. Nevertheless, at high polymer concentration we find a surprisingly high correlation length of the C_{\parallel} structure in the holes with a thickness of a single cylinder layer. This is seen in all samples, where the PL phase covers the rim of the lower terrace.

As we know from in situ measurements (see chapter 7), the structures formed in the thin film follow the pathway through the phase diagram. At high polymer concentration the structure formation is rather fast compared to the terrace formation and always adapts to the structure given by the phase diagram at a given film thickness. This means that the $C_{\parallel,1}$ phase seen in the center of the holes evolved from a perforated lamellae during hole formation. Since the perforated lamella is a bicontinuous structure in the plane of the film, this structure might help to perfect the resulting C_{\parallel} phase. A similar effect is seen in the in-situ measurements of this system at the phase transition from C_{\parallel} to PL as discussed in chapter 7. As a result the correlation length of the cylinders is higher at the bottom of a hole than at the top of an island, if the polymer concentration is below the critical concentration for PL formation.

In melt films of hexagonally ordered spheres there exists an optimal temperature close to the order-disorder-transition (ODT), where the number of defects is minimized [Seg03]. The quality of healing increases first with temperature, since mobility of the chains increases and then decreases, when fluctuations induce lattice defects. Transferring this to our system means there should be an optimal polymer concentration at which the correlation length is maximized. A high amount of solvent inside the system means high mobility of the chains as we see

6 Principal Dimensions of the Microdomain Structure

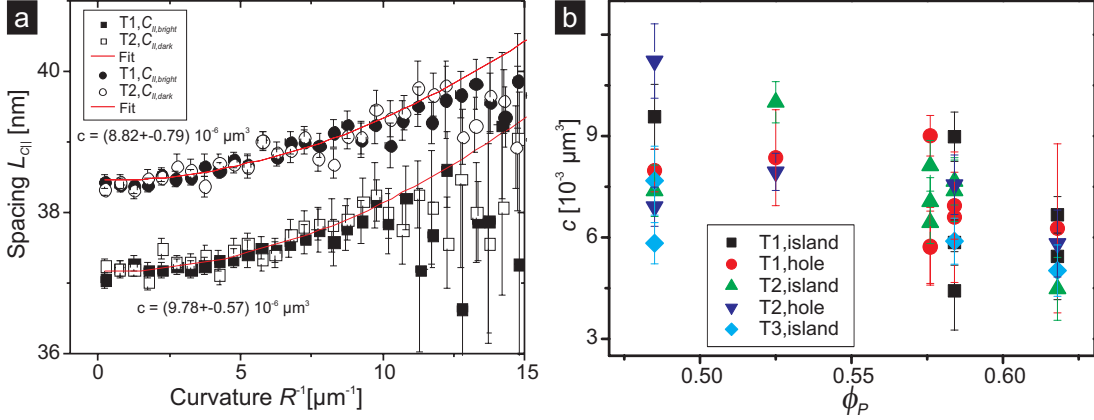


Figure 6.4: a) Example of the measured spacing in the $C_{||}$ structure as a function of the local curvature of the cylinders for a film prepared at $\phi_P = 0.57$. The red lines correspond to fit curves of a function of second order with the minimum at the y axis.

at $\phi_P = 0.48$. Excluding the effect discussed in the previous paragraph we find the highest correlation lengths at this polymer concentration. The comparison to the melt experiments implies that the polymer concentration in our system is still considerably larger than the ODT concentration. Since all our experiments were done on a similar time scale, we can attribute the large correlation length in these films to an increase in the mobility of the polymer.

It should be noted that the microdomain structure is less developed at places where no terrace formation was observed, especially in concentrated samples. Obviously the terrace formation forces the molecules to diffuse from the holes to the islands. This diffusion induces reorientation of the polymer in the terraces, which in turn leads to better ordering of the structures.

6.3.2 Effect of curvature on the microdomain spacing

Since we have information about the positions of points lying along a cylinder in the phase image, we can calculate a local curvature of the cylinders. This is automatically done by the algorithm (see appendix), when the principal distances in the cylinder forming phase are determined. Figure 6.4. shows the dependence of the cylinder spacing from the local curvature of the cylinders. For all the films measured the spacing increases first up to a value of the curvature of approximately $10 \mu\text{m}^{-1}$ to $15 \mu\text{m}^{-1}$. After this critical value the spacing seems

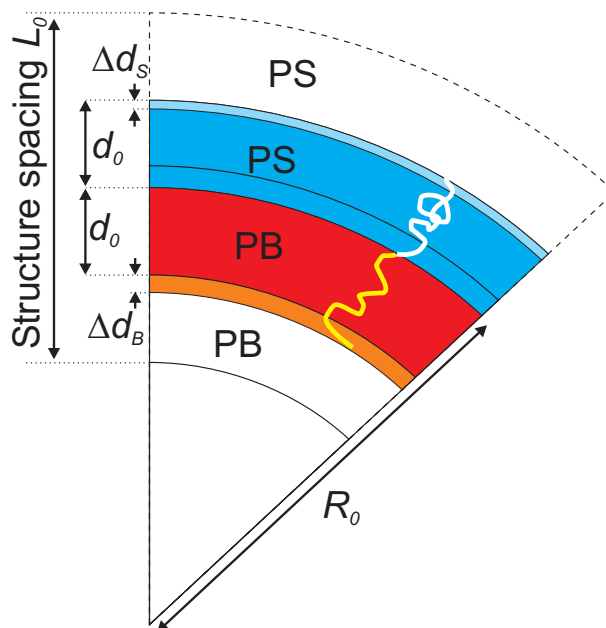


Figure 6.5: Simple Model of diblock copolymer PS-PB forming a two dimensional lamella bend with Radius R_0 . We assume that the volume of the blocks and the density of chains per unit length are conserved. The bending induces a compression of the PS molecules from d_0 to $d_S = d_0 - \Delta d_S$ and a stretching of the PB molecules from d_0 to $d_B = d_0 + \Delta d_B$.

to decrease again, but the statistics are very poor for this rather high curvature. The best fit found for the increase in spacing is a polynomial equation of second order with its minimum at zero curvature.

$$t(R^{-1}) = t_0 + cR^{-2} \quad (6.3)$$

The parameter c is also shown in Figure 6.4 a) for both curves. Equation 6.3 seems reasonable considering the symmetry of the problem. The values found for c for the different polymer concentrations and film thicknesses are shown in Figure 6.4b). The value of c varies from $3 \cdot 10^{-6} \mu\text{m}^3$ to $12 \cdot 10^{-6} \mu\text{m}^3$. Its dependence on the polymer concentration is rather weak, nevertheless c decreases with increasing polymer concentration. There is no significant correlation found between this parameter and the local film thickness or the correlation length.

Let us assume a very simple geometrical model to understand this behavior. The model is shown in Figure 6.5. It assumes a simple two dimensional structure

6 Principal Dimensions of the Microdomain Structure

of parallel stripes, which are bent with a radius R . The two stripes represent two phases of a PS rich and PB rich polymer. The thickness d of the stripes is assumed to be equal, if they are not bent. In this case the spacing between areas of the same kind amounts to L_0 . If the bending does not change the density of molecules at the boundary between PS and PB rich domain, and density conservation is assumed, the boundaries of the stripes have to move. The outer boundary has to move towards the middle boundary and the inner one moves further away from it. The argument of area conservation can be written as: $d_0 R = d_B R + \frac{1}{2} d_B^2$ for the outer area and $d_0 R = d_S R - \frac{1}{2} d_S^2$ for the inner area. Solving these expressions for the modified diameters d_B and d_S and expanding them for small d/R yields a simple expression for the spacing L of the structure in the bend case:

$$L = L_0 + \frac{3}{16} \frac{L_0^3}{R^2} + L_0 O\left(\frac{L_0^4}{R^4}\right) \quad (6.4)$$

In second order approximation the spacing increases by $\frac{3}{16} \frac{L_0^3}{R^2}$, which is quadratic in the curvature $1/R$ as we see it in the experiment. The coefficient c can be evaluated for our model and yields $\frac{3}{16} L_0^3 \approx 11 \cdot 10^{-6} \mu\text{m}^3$ for $L_0 = 39 \cdot 10^{-3} \mu\text{m}$.

In spite of the very simple model for a diblock lamellar structure this value fits very well to the values we get from the experiments. Therefore we may assume that the measured effect can be explained in terms of density conservation and simple geometric arguments.

Note that the calculated value fits best to experiments done at a low polymer concentration, i.e. in rather weakly segregated systems as shown in Figure 6.4 b). As we will see later and as found in chapter 4, strongly segregated systems have a strong tendency to minimize the interfacial area between the polymers. The result is a reduced effect in stronger segregated systems since the interfacial area increases with the increase in spacing in the case of bend cylinders. This reasoning is corroborated by a strong segregation calculation of this problem done by Williams [Wil94]. He determines the free energy of a bend cylinder and shows that upon minimization its cross section is no longer circular. In the case of weak segregation the penalty for increasing the interface is much smaller and the simple argument of density conservation applies better.

6.3.3 The Microdomain Spacing as a Function of Film Thickness

In the previous section we found that the cylinder spacing $L_{C\parallel}$ depends on the local curvature of the cylinders, which could be explained by simple geometric arguments. We already saw in Figure 6.4 that also the mean spacing of the cylinders for the given example is lower for terrace T1 than for terrace T2. Let us now examine the influence of the local film thickness on the lateral microdomain spacing in more detail. In order to separate both effects we consider only spacings measured at points belonging to cylinders with less than $5 \mu\text{m}^{-1}$ curvature. At this curvature $L_{C\parallel}$ increases only by about 0.3 nm, which is comparable to the scatter of the data. The height measured as topography by the AFM can be used to correlate height information for every structural point with the locally determined spacings.

Since the distribution of the measured distance data is rather broad, we need to average it over certain height intervals. Figure 6.6 displays the variation of the mean microdomain spacings averaged over height intervals of 1 nm of for the different structures as function of the local thickness of the polymer film. The error bars represent standard errors of the average values. The x axis represents the local thickness of the polymer film in the quenched state, i.e. after the solvent has been removed. Background subtraction in the AFM height images has been done by maximizing the peaks of the terraces in the height histogram as described in chapter 5. The mean heights of the terraces are shown as vertical black lines in the figure. They have been measured by metrology AFM as described in 5. The three figures from top to bottom show data for samples prepared at rather low polymer concentration, $\phi_P = 0.62$ in Figure 6.6 a), at intermediate concentration, $\phi_P = 0.58$ in Figure 6.6 b) and at low concentration $\phi_P = 0.48$ in Figure 6.6 c).

The spacing L_{PL} plotted for the PL structure has been calculated by multiplying the measured spacing of the PL holes by a factor of $\sqrt{2}/3$. L_{PL} then is a measure of the distance between the lines of the holes of the perforated lamella. This seems reasonable since it determines the distance between polystyrene rich areas rather than between polybutadiene rich areas. Therefore L_{PL} becomes comparable to the spacing of the other structures.

As a first result we find that the spacings of all samples follow the same general trend. The spacing of the C_{\perp} structure $L_{C\perp}$ is larger than $L_{C\parallel}$ over the whole

6 Principal Dimensions of the Microdomain Structure

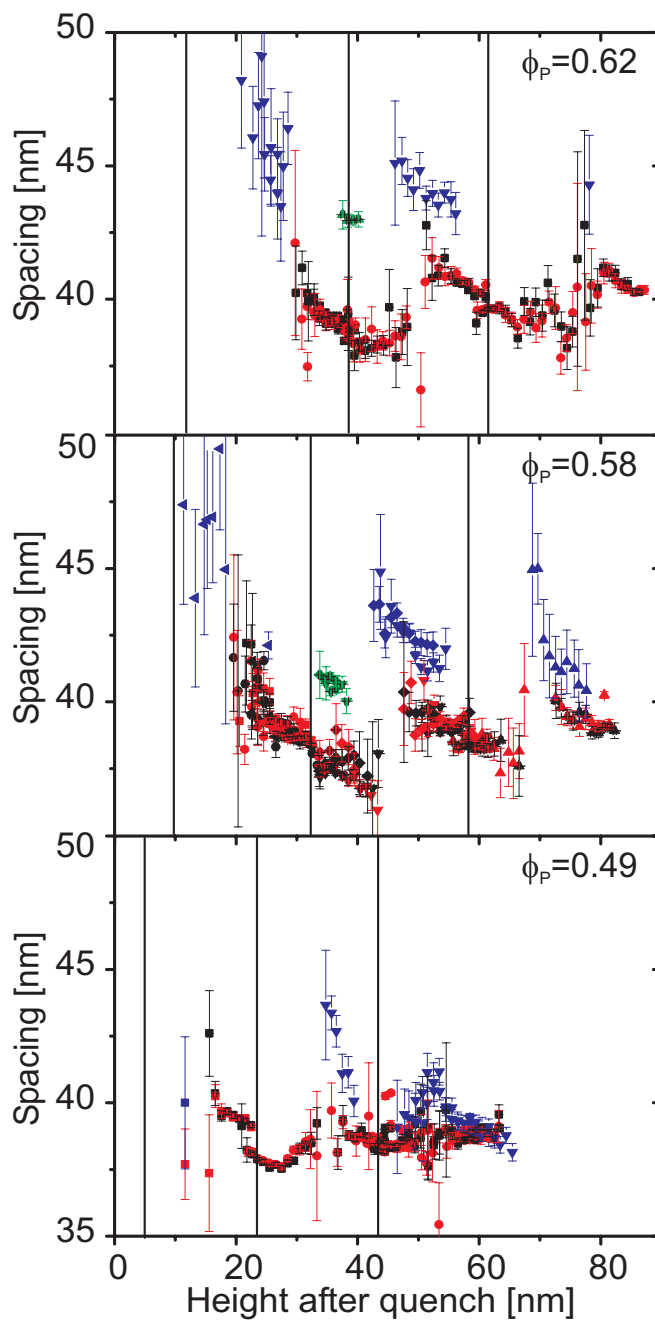


Figure 6.6: Plots of the microdomain spacing versus the local film thickness for the structures C_{\perp} (blue), PL (green) and C_{\parallel} (red and black). From top to bottom the polymer content in the thin film decreases from $\phi_P = 0.62$ to $\phi_P = 0.58$ to $\phi_P = 0.48$. Black vertical lines denote the heights of the terraces T_n incorporating n layers of cylinders. Different samples are marked by different symbol shapes. All spacings have been averaged over height intervals of 1 nm. The error bars correspond to standard errors of the averaged spacings.

6.3 Results and Discussion

thickness range. The spacing of the PL structure L_{PL} lies in between. This effect decreases with lower polymer concentration, i.e. with lower segregation. The polymer content $\phi_P = 0.48$ is below the existence range of the perforated lamella. For this sample $L_{C\perp}$ is almost equal to $L_{C\parallel}$.

All spacings depend on the local thickness of the film, especially $L_{C\parallel}$ and $L_{C\perp}$. The thickness range of the PL structure is rather small and therefore the dependence of its spacing on the film thickness is not very evident. It appears to decrease slightly with increasing film thickness.

$L_{C\perp}$ decreases as the film thickness increases from one terrace to the next terrace. We attribute this effect to the existence of hybrid structures as discussed in the next section of this chapter.

Let us now concentrate on the data for the C_{\parallel} structure. The microdomain spacing $L_{C\parallel}$ of the cylinders in this phase varies systematically with the local film thickness. At any terrace thickness it assumes an intermediate value, while it increases for smaller thicknesses and decreases for larger thicknesses. This effect is stronger for more concentrated samples and for a lower number of cylinder layers in the thin film. The values of the slopes can be found in table 6.1.

Table 6.1: Measured slopes of $L_{C\parallel}$ for the terraces T1, T2 and T3 as shown in Figure 6.6 as a function of the polymer content ϕ_P .

Polymer content ϕ_P	Terrace T1	Terrace T2	Terrace T3
0.62	-0.2	-0.17	-0.16
0.58	-0.15	-0.10	-0.08
0.49	-0.1	-0.05	0

In chapter 4 we discussed the microdomain spacing as a function of the film thickness in the strong segregation regime. The result is very similar to what we see in the experiments. If the unit cell has to adapt to the film thickness by stretching or compression, the width of the unit cell and therefore the cylinder spacing decreases or increases, respectively. The reason is that any deformation of the circular core of the unit cell increases the interfacial area between A and B blocks. If the system is forced to stretch in one direction it tries to minimize the interfacial tension by shrinking in the perpendicular direction. The strong segregation treatment predicts a decrease of the cylinder spacing L with film

6 Principal Dimensions of the Microdomain Structure

thickness t according to

$$dL/dt = -1/n, \tag{6.5}$$

where n is the number of cylinder layers in the system. For the first three layers we therefore expect slopes of -1, -0.5, -0.33, which is considerably more than seen in the experiments.

There are several issues to be discussed. Let us first estimate the degree of segregation in our system. An estimation of the interfacial tension between the blocks of a ABA triblock copolymer is given by $\chi N/2$, where χ is the monomeric interaction parameter between A and B monomers and N is the total degree of polymerization of the molecules. For block copolymers build from PS and PB we find χ values in the literature [Sak92]. For the three values of χ given in this reference we get an average interfacial interaction of $\chi N/2 = 49 \pm 6$ at a temperature of $T = 25^\circ C$. Using the dilution approximation for calculating an effective interaction in the diluted system we get values of $\chi N/2 \phi_P = 31 \pm 4$ at $\phi_P = 0.62$ and $\chi N/2 \phi_P = 24 \pm 3$ at $\phi_P = 0.48$. The latter value for $\phi_P = 0.48$ is rather close to the order disorder transition and therefore close to the weak segregated regime, while the value at $\phi_P = 0.48$ is in the intermediate segregation regime.

The strong segregation theory treats all chains as uniformly stretched, and therefore overestimates the influence of the interface between the blocks [Mat03]. Since our system is always in intermediate segregation any effect caused by interfacial minimization will be much less pronounced than predicted by the SST calculations. Therefore the effective slope measured in the experiments is much smaller than predicted and tends to decrease with decreasing polymer concentration.

Another issue is the connectivity of the cylinders. Although the thickness gradient of a terrace is rather small inside the terrace it becomes considerable close to the edge of the terraces in comparison to the cylinder spacing. Since cylinders are highly elongated structures they may not be able to adapt a new spacing in a neighboring area of somewhat different films thickness since the two structures will not be commensurable. One way for the cylinders to avoid this problem would be to align parallel to the rim of the terraces. Nevertheless, this

is not seen in our experiments.

6.3.4 Comparison of Relevant Dimensions

The microdomain spacing of the C_{\parallel} structure $L_{C_{\parallel}}$ determines the width of the unit cell of cylinders oriented parallel to the substrate. In this section we want to compare this dimension to other relevant dimensions in the thin film, namely the thickness of the cylinder layer and the microdomain spacings of the structures PL and C_{\perp} . In order to do so, we need to establish mean or optimal values of the microdomain spacings of the different structures. In the case of the C_{\parallel} structure we would like to consider the spacing of the unperturbed, i.e. not stretched or compressed, cylinders. To determine this quantity for a given terrace T_n we establish the following procedure. If the terrace is formed as an island with maximum thickness t_{max} , we measure the spacing for a thickness range of $t_{max} - 4 \text{ nm}$ to t_{max} . If the terrace is formed as a hole we do the same around the minimum thickness of the hole. Then both quantities are averaged and a mean error is computed. Since the statistics for $L_{C_{\perp}}$ are rather poor, we simply apply a gaussian fit to the distribution to find a most probable spacing. The same is done for L_{PL} . The thickness of the cylinder layers has been determined from the phase diagram shown in chapter 5 as the difference of the averaged (black lines in the phase diagram) terrace heights T_{n+1} and T_n . The error is estimated from the scatter of the measured thicknesses around these lines.

Figure 6.7 shows all dimensions as a function of the polymer content ϕ_P of the polymer film. Also shown is the average spacing in the bulk as determined by small angle X-ray scattering (SAXS) measurements outlined in chapter 5. At low polymer concentration all quantities have similar values of $39 \pm 1 \text{ nm}$, while the scatter becomes larger with increasing polymer concentration.

The scaling of the bulk microdomain spacing with increasing polymer concentration in good solvents has been measured for different systems before [Has83, Han98, Lod03a]. All studies determine an increase of the spacing following a power law with exponents close to 0.3 in the concentrated regime, i.e. far from the order disorder transition. The SAXS data in our experiment increase according to $\phi_P^{0.12}$.

In the following we want to discuss the deviations of the different spacings from the bulk spacing L_0 in detail and compare them to the predictions made

6 Principal Dimensions of the Microdomain Structure

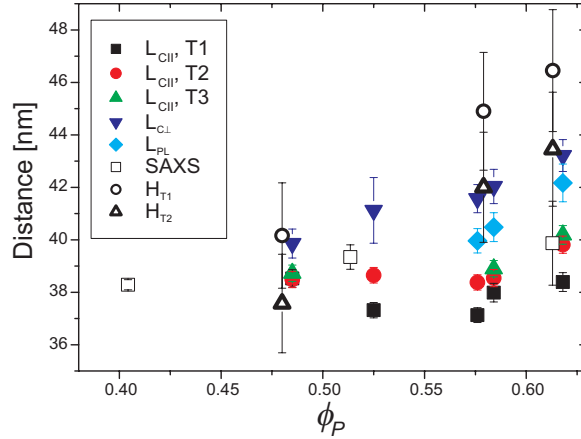


Figure 6.7: Comparison of the relevant dimensions measured in the thin films. Lateral average microdomain spacings are shown for $L_{C\parallel}$ for terraces T1, T2 and T3, for the PL structure L_{PL} and for the C_{\perp} structure $L_{C\perp}$. Also shown is the thickness H_{T1} and H_{T2} of the 1st and the 2nd cylinder layer and the average spacing in the bulk as measured by SAXS.

by the SST treatment of thin films of cylinder forming polymers in chapter 4.

Cylinder layer thickness H

The thickness of the first cylinder layer H_{T1} exceeds all other spacings measured for this system. This is not expected from the theory. The theory predicts a thickness of the first layer of cylinders, which is 8% smaller than L_0 but also 8% larger than the bulk cylinder layer spacing $L_1 = \sqrt{3}/2 L_0$. It does predict a much smaller thickness of the second layer in comparison to the first, but again also smaller than L_0 .

In contrast to this result, the average spacing of the cylinder layers can be determined more accurately and consistent to the theory, if one has access to a higher number of cylinder layers. In Figure 5.12 in chapter 5 we found an average layer thickness of 35 ± 2 nm, which fits to the measured cylinder spacing of 39 nm. The result implies that the wetting layer underneath a cylinder layer is thicker than the pure wetting layer, which makes the determination of the layer thickness as described above unreliable.

Another considerable effect might be due to the solvent distribution in the thin film, which will not be perfectly homogeneous. The solvent tends to screen repulsive interaction and accumulate at the respective locations. This has been

shown theoretically for solvent accumulating at the A-B interface of an AB diblock copolymer [Fre89]. On the other hand it will enrich at the surface since it has the lower surface energy. Measuring any accumulation layer with ellipsometry proved difficult since the refractive indices of polymer and solvent are rather close.

Another reason may be systematic errors in the determination of the wet terrace heights. This cannot be excluded since the film preparation and the ellipsometric measurements outlined in chapter 5 were conducted in a different experimental setup.

Perpendicularly oriented cylinders C_{\perp}

The spacing $L_{C_{\perp}}$ of the upright cylinders increases moderately with ϕ_P and assumes the largest value of the in plane measured microdomain spacings. $L_{C_{\perp}}$ is also larger than the measured bulk spacing L_0 . This result is in contradiction to the predictions made by strong segregation theory in chapter 4 that the upright cylinders should assume the bulk spacing.

The SST theory assumes no deformation of the bulk unit cell structure for the perpendicularly oriented cylinders. This assumption is rather crude and any relaxation might lead to an increase in the spacing of the cylinders. SCFT calculations of perpendicular and mixed lamellar phases of diblock copolymers predict this increase only for the mixed morphologies [Mat97]. Early measurements on our systems already revealed the existence of hybrid or mixed structures formed as cylinders with necks [Kon00]. Therefore the assumption of a mixed morphology seems reasonable. As shown in Figure 6.6 $L_{C_{\perp}}$ is dependent on the thickness of the film and decreases with increasing film thickness. This behavior can be explained by a transition of cylinders with necks to upright cylinders with increasing film thickness. The AFM phase images as shown in figure 6.1 a) and in chapter 5 corroborate this assumption. They show first a modulation of the white stripes, which transforms into clearly isolated bright dots in the center of C_{\perp} phase. Since we only measure an average spacing of this structure we determine a larger value than expected.

Another effect might be induced by the quenching process of the swollen films. We assume that the film shrinks only along the surface normal leaving all lateral structures intact. This should be a good approximation since the diffusion of

6 Principal Dimensions of the Microdomain Structure

the solvent molecules is much faster than the diffusion of the block copolymer. Nevertheless, if there is a slight effect of this shrinkage on the lateral structures it should be mostly visible in the steps of the terraces and at high dilution of the polymer. Any lateral shrinkage should in turn induce an anisotropic deformation of the hexagonal unit cell of the C_{\perp} structure parallel and perpendicular to the rim of the terrace. Nevertheless, this could not be measured within the experimental errors.

In plane cylinders C_{\parallel}

The mean spacing $L_{C_{\parallel}}$ of the parallel oriented cylinders is always lower than L_0 . The effect increases with a decreasing number of cylinder layers with a maximal deviation of about 4% for the first layer of cylinders at $\phi_P = 0.62$. Note that the effect prevails at all concentrations except the lowest one at $\phi_P = 0.48$. As seen in Figure 6.6 c) the samples prepared at this concentration show a rather large difference in $L_{C_{\parallel}}$, $T1$ as measured on top of an island and at the bottom of a hole.

A decreased spacing of the first cylinder layer is predicted by the SST calculations and is due to the deformation of the hexagonal unit cell in the C_{\parallel} structure to a more rectangular unit cell close to the surfaces. In the strong segregation limit the deviation amounts to approximately 3% for the first layer of cylinders (see chapter 4), which is in good agreement with the measured data. This seems initially surprising since the SST treatment overestimates the dependence of $L_{C_{\parallel}}$ on the local film thickness. Nevertheless, the decreased spacing is caused by a different shape of the unit cell and not by any anisotropic deformation. Therefore the influence of interfacial effects is rather weak and the results may be valid qualitatively also for weaker segregated systems. The dependence of the effect on ϕ_P is rather weak, which corroborates this assumption.

Spacing of the perforated lamella L_{PL}

The lateral spacing of styrene-rich microdomains in the perforated lamella structure L_{PL} is always somewhat larger than the measured bulk cylinder spacing. Since the PL structure has another symmetry than the cylindrical phases it seems questionable to compare their spacings. The transition to the PL structure occurs preferentially in the first layer, which in turn has the smallest spacing for

the parallel cylinder structure C_{\parallel} .

In chapter 5 we discussed this transition to be caused by the surface field, which preferentially adsorbs the PB-block at the surface. If we define an order parameter as the local density of the A block, this quantity is therefore reduced at the surface and enhanced in the center of the film. We argued that this is the predominant effect for a transition to the PL structure at large surface fields.

In the light of the results of the SST treatment and the evaluation of the lateral spacings we may add additional arguments:

The SST treatment predicts an increase in the minimal free energy of the C_{\parallel} structure due to the deformation induced by the rectangular unit cell close to the surface. Per molecule this effect is most pronounced in the first layer of cylinders. The free energy per molecule of the PL phase should not change in thin films since it anyway has planar interfaces. Therefore a transition to a perforated lamella is predicted to occur preferentially in the first layer of cylinders.

In terms of the microdomain spacings this argument may be written as follows. Due to the deformation of the C_{\parallel} unit cell in the first layer of cylinders $L_{C_{\parallel}}$ becomes considerably smaller. The spacing measured for the PL structure is in between the one for the C_{\parallel} and the C_{\perp} structure. Therefore the lateral compression of the cylinders can be relaxed by reconstructing to a perforated lamella.

6.3.5 Conclusion

We established an image analysis algorithm, which enables us to precisely study the details of the microdomain structure in thin SBS films.

The evaluation of the orientational correlation length of the C_{\parallel} structure quantifies the better long range order for more diluted samples. A better alignment of the C_{\parallel} structure can also be mediated by the path of structure formation through the phase diagram upon terrace formation. If the C_{\parallel} structure originates from the bicontinuous PL structure a largely improved long range order is observed.

An examination of the dependence of $L_{C_{\parallel}}$ from the local curvature of the cylinders yielded an effect of second order, which could be explained in terms of density conservation of the polymer blocks.

The spacing of the C_{\parallel} structure depends on the local thickness of the thin film. The C_{\parallel} phase is stable around a certain thickness range of its preferred thickness.

6 Principal Dimensions of the Microdomain Structure

Within this range it has to adapt the cylinder height to be commensurable with the film thickness. Minimization of the interface between the blocks leads to a smaller or larger cylinder spacing if the cylinder has to stretch or shrink its dimension perpendicular to the plane of the film. The SST calculations presented in chapter 4 overestimate the effect dramatically due to the highly exaggerated influence of the interface between the blocks in the SST treatment. The effect diminishes at higher dilution since interfacial effect become less important in this regime.

A comparison of the mean spacings of all structures to the bulk spacing of the hexagonally ordered cylinders reveals additional effects of thin film constraints on the microdomain structure. The comparatively large spacing of the C_{\perp} phase points to the existence of hybrid structures like cylinders with necks in the thin film. The spacing of the C_{\parallel} structure increases with the numbers of cylinder layers and approaches the bulk value for thick films as predicted by the SST theory. The deviation in thin films can be explained by the increasing deformation of the cylinder unit cell by the planar symmetry of the surface/interface. This deformation in turn increases the free energy of the cylinders in very thin films and therefore favors a transition to a PL in one layer of cylinders.

6.4 Appendix: Image Analysis - Determination of the Characteristic Spacings

In short the image analysis is performed in three steps: first the phase image is binarized. Then the structure is determined by filling the resulting areas with the help of a area filling algorithm, which assigns single points along the structures by weight averaging local areas. Third the neighborhood of every point every point is examined in order to detect defects and phase boundaries. In the following we describe in detail the procedure for each step.

Step 1: Binarizing the AFM phase contrast image

The transformation of the original phase images into binary patterns proves difficult due to the fact that the different lateral patterns (parallel cylinders (C_{\parallel}), perforated lamellae (PL), upright cylinders (C_{\perp})) tend to exhibit different average values of the phase shift. Therefore, the original phase images were filtered first by a Fourier filter, which removes all wavelengths below 100 nm.

6.4 Appendix: Image Analysis - Determination of the Characteristic Spacings

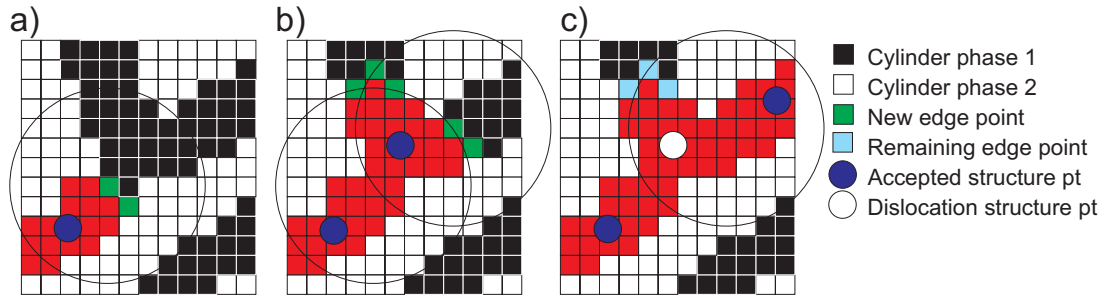


Figure 6.8: Filling of the binarized phase image. Here the recognition of a dislocation in the C_{\parallel} structure is shown. Black and white squares represent unfilled areas. Image a) to c) depict three consecutive steps of the filling process. All points are filled within distance 0.8λ (circle) from a randomly chosen starting point (green squares). A structural point (blue circle) is then placed at the phase weighted center of the newly filled area. The dislocation (white circle) is recognized in c), since not all edge points of step b) are filled (blue squares).

This procedure merely reveals the laterally averaged values of the phase shift for the different microdomain structures. The filtered image is then multiplied by a factor k ($k = 0.1$) and subtracted from the original data (corrected phase image). In some cases the original phase images needed to be slightly smoothed by a FFT-cutoff filter with cutoff wavelength set to 25 nm. The images are then binarized by setting a threshold value around zero. The exact value of the threshold and the factor k are chosen such that the areas on and between the lying cylinders in C_{\parallel} are about equal and that isolated dots are revealed in the PL and the C_{\perp} phases.

Step 2: Structure determination

From a Fourier-Transform of the resulting image we then determine an average characteristic spacing λ . In order to find the central lines within the cylindrical microdomains, the following procedure was applied (see Figure 6.8). Starting from a point at the boundary between two stripes, all adjacent points of the same color are filled up to a distance 0.8λ from the starting point. Points of same color located at a distance 0.8λ of the starting points are NOT filled and will be referred to as the boundary of the marked area. Subsequently, the center of gravity (S1) of the filled area weighted by the phase values of the corrected phase image is determined. S1 determines one point in a line of points along the center of the C_{\parallel} structure. A point at the boundary is used as starting point to repeat the above procedure as shown in Figure 6.8 b). This step reveals

6 Principal Dimensions of the Microdomain Structure

a neighboring point S2. A dislocation is recognized, if there are remaining edge points of S1 after filling the area around S2 as shown in Figure 6.8 c). S1 is then marked as dislocation and the remaining edge points are put into memory for later evaluation. The procedure is iterated until no boundary is found and all edge points are filled, i.e. the entire area of the stripe has been filled. The points S1, S2, S3, ... establish lines located in the center of the respective stripe. The same procedure is applied to all stripes (black and white).

If the above procedure does not reveal any boundary, i.e. if the initial filling step already suffices to fill the entire area, the respective area is identified as an isolated point. Again, the weighted center of gravity is determined to localize the center of this area.

Step 3: Examination of the local neighborhood

So far we have determined structural points for each of the structures C_{\parallel} , C_{\perp} and PL. C_{\perp} and PL can be identified if there is only a single point of color white and black, respectively. The connected lines of points represent the C_{\parallel} structure. For further evaluation it is necessary to examine the local environment for each point to accept it as the given structure in order to minimize errors. For example the matrix of the structures PL and C_{\perp} is continuous and would therefore be accepted as C_{\parallel} structure. On the other hand defects inside the C_{\parallel} structure are often point like and would be falsely determined as PL or C_{\perp} structure. Therefore we establish a set of rules for each structure, which has to be fulfilled to accept a specific point of the structure as valid.

Figure 6.9a) shows the situation for the C_{\parallel} structure. The first rule for a point identified as C_{\parallel} structural point is that it is situated between two points of the same kind, i.e. it belongs to a connected line of points and is at least one point away from a defect. It has to have two neighboring lines of the same type and two neighboring lines of reverted type in between (green and blue points in Figure 6.9a)).

In order to measure a microdomain spacing at the recognized point, a circle is constructed from the central three points as shown in Figure 6.9a). Two distances are extracted for every C_{\parallel} point as the distance of the closest points lying on the neighboring lines of points of the same color to the circle. Additionally the local curvature of the cylinder can be measured as the inverse of the radius of the circle.

6.4 Appendix: Image Analysis - Determination of the Characteristic Spacings

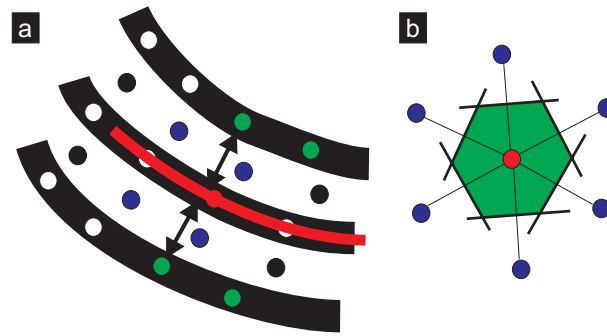


Figure 6.9: Examination of the neighborhood of the C_{\parallel} structure (a) and the point like structures C_{\parallel} or PL (b). For a) the two neighboring lines of points of equal and opposite color are examined. The local curvature is measured by constructing a circle to the center point and its two neighbors. The spacing of the structure is determined from the distance of two points from the circle as indicated by the arrows. The condition for b) is a hexagonal unit cell. All distances to the six neighbors are taken into the statistics.

Figure 6.9b) displays a dot like structural point and its environment. It is accepted as PL or C_{\perp} , if it has 6 nearest neighbors of the same type. The number of nearest neighbors is determined by applying a Voronoi construction, which is equivalent to constructing the Wigner-Seitz unit cell for the given point. In this way points lying at a phase boundary are avoided as well as points lying close to a defect. It has been shown that the distances measured close to a defect deviate considerably from those measured far away from any defect [Seg03].

The direction of the structure is then determined as the average over the angles to each neighbor modulo 60 degrees. The distances to the six nearest neighbors are taken as individual microdomain spacings.

6 Principal Dimensions of the Microdomain Structure

7 Dynamics of Structure Formation in Thin Films of Cylinder Forming Block Copolymers

The dynamics of structure formation in a thin film of a concentrated solution of polystyrene-*b*-polybutadiene-*b*-polystyrene (SBS) in chloroform has been studied by *in-situ* scanning force microscopy (SFM). The initial film thickness has been chosen such that the film is unstable against thickness variations and spontaneously forms areas of larger and smaller film thickness called islands and holes, respectively. The microdomain structure transforms from cylinders oriented perpendicular to the substrate C_{\perp} to cylinders oriented parallel C_{\parallel} and finally to a perforated lamella PL as the thickness of the film decreases within the holes. In both phase transitions the first grains of the new structure are formed at grain boundaries of the original phase and the transitions proceeds along the grain boundaries. The C_{\parallel} phase is formed via interconnection of next nearest C_{\perp} cylinders. Since the two structures are incommensurable a reorientation of the lying cylinders is necessary to regain their natural lateral domain spacing. The grain size is smallest within the C_{\parallel} phase, since this structure has only twofold symmetry. The defects decorating the grain boundaries of the C_{\parallel} phase serve as nucleation centers for the PL structure. The PL grains grow along the C_{\parallel} grain boundaries via the undulation of in plane cylinders, which eventually connect to form PL lattice sites. Due to the bicontinuous nature of the PL elementary structure in the plane of the film, healing of the microdomains is very efficient both for the C_{\parallel} phase close to the transition into the PL phase and for the PL phase itself. The healing process of the PL phase is described by an analysis of the defect movements in this two dimensional hexagonal phase. The elementary motions, the creation and annihilation of dislocations are studied and the splitting and merging of lattice sites is explained.

7 Dynamics of Structure Formation

7.1 Introduction

The bulk kinetics of structure formation and structure transitions in block copolymers and block copolymer solutions have been studied to a noticeable extent in the past. The specimens were studied by various techniques, including optical birefringence [Amu92, Amu93, Amu94], small angle x-ray scattering (SAXS) [Boe02b, Boe02a], transmission electron microscopy (TEM) [Has95, Has98], rheology and depolarized light scattering [Dai96, New98].

The first set of experiments regards the structure formation from a disordered state. The samples are quenched from a temperature above the order-disorder transition temperature (T_{ODT}) to a temperature below. After a finite incubation time slow nucleation takes place. The resulting grains were shown to be highly anisotropic, extended in the lamellar phase perpendicular to the lamellar direction as revealed by TEM imaging [Has95] but along the cylinder direction as concluded from depolarized light scattering experiments [Dai96]. The grains grow rather fast, depending on the depth of the temperature quench until the whole volume is filled by grains [Has98, Dai96]. It has been shown that there is an optimal quench depth, where the grain growth rate is maximized as a result of the interplay between phase separation driving forces and frictional forces [Kim01a]. The subsequent growth of individual grains on the expense of other grains via defect annihilation was shown to be very slow [New98].

The second set of experiments examines order-order transitions (OOT). In these experiments a non equilibrium morphology is prepared for example in a selective solvent and is then annealed to regain its equilibrium morphology [Sak93, Jeo03]. Another way to induce order-order transitions is to choose a suitable composition of the block copolymer close to a phase boundary in the phase diagram. Annealing at different temperatures or dilution with a nonselective solvent then induces phase transitions [Lod03a, Sak96]. The same effect can be reached by using selective solvents to selectively increase the effective volume fraction of one of the blocks [Han98].

Proposed mechanisms of the structural transitions are the coalescence of the smaller structures to form the more extended structures. Preceding the coalescence is a deformation of the starting structure. The sphere to cylinder transition takes place along the (111) direction of the bcc sphere lattice [Sak96], while cylinders coalesce along their long axis to form a lamellar structure [Sak93]. In both

examples the original and final structures were approximately commensurable resulting in a rather fast phase transition. The subsequent ordering of the structures was shown to be much slower.

In thin films of cylinder forming block copolymers phase transition to other microdomain structures are caused by the surface field and a transition from in plane cylinders to cylinders oriented perpendicularly to the substrate is induced by incommensurability effects as described in chapter 5. The study of the microdomain structure in thin films is mainly done by transmission electron microscopy (TEM), scanning electron microscopy (SEM) or scanning force microscopy (SFM). Since the electron beam induces damage to the polymers the first two methods cannot be applied to study the dynamics in thin films *in-situ*. Multiple samples with different annealing conditions have to be prepared and only statistics of e.g. defect concentrations may be extracted. The same holds, if the microdomain structure is buried underneath a polymeric layer thick and/or hard enough to prevent direct imaging by SFM [Seg03]. In this work the melting of a 2D crystal of spherical microdomains is studied. The authors find an optimum temperature of annealing below the ODT temperature, where the amount of defects is minimized.

In principle SFM provides all necessary means to observe microdomain dynamics *in-situ*. It is nondestructive and can be operated at elevated temperatures and in different environments. Nevertheless the SFM phase contrast vanishes upon heating above the glass transition temperature of both blocks and makes imaging very difficult. Therefore Harrison et al. [Har99, Har02] annealed their samples above the highest glass transitions temperature repeatedly and imaged the same sample spot after cooling under ambient conditions. Thus they investigated defect annihilation and long range ordering in a system of in plane cylinders. The same approach was taken by Hahm et al. [Hah98] to study the defect motion in a similar C_{\parallel} system.

In this chapter we describe the first *in-situ* measurements of block copolymer phase transitions in a thin film. The phase diagram of the system polystyrene-*b*-polybutadiene-*b*-polystyrene (SBS) diluted by the nonselective solvent chloroform has been presented in chapter 5. We prepared a thin film with an unstable film thickness, which splits into islands and holes upon solvent annealing. This process was followed in real space and real time using a modified SFM setup for

7 Dynamics of Structure Formation

imaging in solvent vapor atmosphere. A sufficient tapping mode phase contrast could be achieved by optimizing the scanning parameters.

After describing the materials and the *in-situ* SFM setup we start with an overview of the temporal evolution of the thin film. The film develops islands and holes to minimize its free energy. We show how during hole formation phase transitions take place from cylinders oriented perpendicular to the substrate (C_{\perp}) to cylinders oriented parallel to the substrate (C_{\parallel}) and finally to a perforated lamellar phase (PL). These transitions are studied in detail and the effects of commensurability and symmetry of the phases are discussed. The PL phase is created with a large number of defects, and details of defect motion, creation and annihilation are investigated.

7.2 Material and Method

We study the dynamics in a thin film of a cylinder forming polystyrene-*block*-polybutadiene-*block*-polystyrene (SBS) Copolymer swollen by chloroform. The Polymer was obtained from Polymer Source Inc. with molecular weights $M_{w,PS} = 14$ kg/mol, $M_{w,PB} = 73$ kg/mol, and $M_{w,PS} = 15$ kg/mol (PS is polystyrene, PB is polybutadiene). Taking into account the densities of the homopolymers (1.05 g/cm³ for PS and 0.93 g/cm³ for PB) [Bra89] the volume fraction of PS is $f_{PS} = 0.26$. The silicon substrates were cut from wafers, cleaned in fresh 1:1 H₂SO₄ (conc.)/H₂O₂ (30%) solution, thoroughly rinsed in boiling and cold Millipore water and additionally cleaned by a Snowjet. A 1.5 wt% solution of the polymer in toluene was spin cast onto the substrate at 2000 rpm. The resulting film thickness is about 70 nm.

7.2.1 Solvent vapor control

The amount of solvent vapor in the setup was controlled as described in chapter 5. Two gas flows are mixed, one saturated by chloroform vapor in a washing bottle, the other pure N₂. The volume flow of both channels was controlled by two mass flow controllers connected to a "Multi Gas Flow Controller 647 B" from MKS Instruments; the total flow was 15 cm³/min. The temperature of the solvent bath was kept at 25.0±0.1 °C via a thermostat, slightly above room temperature. The amount of volume flow of the saturated vapor was adjusted to 0.65 of the

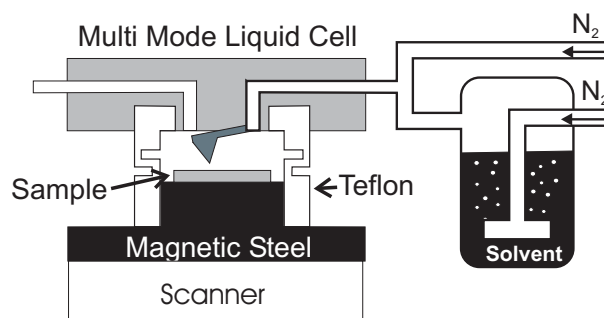


Figure 7.1: Setup for the *in-situ* measurements. The vapor pressure of chloroform is controlled by mixing two gas flows of N_2 , one saturated by chloroform vapor. A little teflon ring and a magnetic steel hat was constructed to establish a sealed environment of solvent vapor atmosphere around tip and sample.

total flow and determines a similar vapor pressure of chloroform relative to its saturated vapor in the mixed gas stream. From ellipsometric measurements (see chapter 5) we can estimate a polymer volume concentration of $\phi_P \approx 0.73$ and therefore a film thickness of the swollen film of $t = t_0/\phi_P \approx 95$ nm.

7.2.2 In-situ Scanning Force Microscopy

The Scanning Force Microscopy (SFM) setup consists of a commercially available MultiModeTM instrument from Digital Instruments, Veeco Metrology Group and a Nanoscope III controller. The instrument was operated in TappingMode SFM. A Olympus Tapping Mode cantilever was used (spring constant ≈ 40 N/m, resonance frequency of about 250 kHz). The TappingMode parameters are discussed below.

Figure 7.1 shows the setup for acquiring the *in-situ* SFM data. The SFM instrument is supplied with a liquid cell, which is normally used for studying samples in water. To create a sealed chamber for organic solvent vapor atmosphere, a little teflon gasket was constructed. This ring fits into the spacer inside the liquid cell, which normally holds a silicon rubber ring. To increase the flexibility of the teflon ring it was shaped like a bellows as shown in Figure 7.1. The resulting gasket was soft enough to establish stable imaging but still introduced distortions to the SFM images as described later. The sample is put on top of a magnetic steel hat, which fits into the teflon ring and is attached to the scanner by magnetic forces. The solvent vapor preparation chamber was connected to the liquid cell by teflon tubes with a diameter of 2 mm. The tubes were attached

7 Dynamics of Structure Formation

to the liquid cell via home made teflon connectors, which fit into the inlets in the liquid cell. No additional overpressure was applied.

Scanning of the swollen block copolymer film proved difficult due to the liquid nature of the sample. The maximum phase contrast of approximately 2 degrees could only be achieved in a very narrow setpoint amplitude range of 0.995 to 0.998 of the free amplitude. The free amplitude was chosen rather high, at 3.5 V, which corresponds to approximately 70 – 90 nm for this type of tip. The combination of the large free amplitude and an amplitude setpoint very close to the free amplitude establishes very short interaction times of the tip to the sample but enough interaction to achieve a measurable phase contrast. Nevertheless the amplitude fraction used for the setpoint varies in time and has to be adjusted continuously, which was done by using the build in "drive feedback" feature. This method checks the free amplitude after every scan line by removing the tip from the surface by 30 nm and corrects the setpoint amplitude to the chosen fraction of 0.997 of the free amplitude. Another important parameter is the scanning speed. Scanning at low speeds resulted in images with frequent bright horizontal stripes in the height image. These stripes are attributed to a pickup, dragging and release of material by the tip. An increase in scan speed reduces this effect, possibly due to the reduced interaction time of the tip with the same spot on the sample surface. In our study we used a scanning speed of 4 lines/sec for the $4 \times 4 \mu\text{m}$ images.

7.2.3 Movies

All frames captured during the measurement were saved as bitmaps by homemade software [NI00] and afterwards converted into "avi" movies with the help of Corel Photo Paint 9 [CC99]. All movies can be found in the web [Hom03] and on the included CD [Kno03]. Since the drift of the setup was rather large and the measurement time exceeded 20 h, a movie of the same spot of the sample was only possible by picking a small area of one frame and tracking this area in earlier and later frames. A detailed description of this procedure is given in the appendix. Furthermore it turned out that registering the images and watching frame by frame enhanced the visibility of typical artifacts introduced by nonlinear SFM scanners. Possibly these artifacts have been enhanced by the rather stiff setup of the teflon gasket in the experiment. In order to reduce or cancel these artifacts

the partial images have been sampled on a non orthogonal lattice corresponding to the induced deformations by the scanner. This procedure is also described in the appendix.

7.2.4 Noise Reduction

The quality of the raw AFM phase images was very good during the first few hours of the experiment. At later times the quality decreased possibly due to tip wear. Additionally the perforated lamella phase turned out to yield a lower phase contrast than the other phases. Individual lattice sites in this phase can hardly be recognized in a single frame of the raw data.

One way to improve the image quality is to reduce noise by Fourier filtering the images. Homemade Labview software [NI00] was used to cut off all frequencies with a wavelength below 25 nm in Fourier space. The resulting movies are marked by the suffix "_fft". The noise in the images could be largely reduced by this procedure without any averaging in time.

Watching the movies with a rather high frame rate turned out to enhance the visibility of lattice site movement drastically. Obviously the eye effectively averages the images in time. We tried to simulate this effect by using filters, which average along the time axis. The freeware program "virtual dub" [Lee03] provides all necessary means. We used two filters supplied with the program to establish time averaging. The first one is the "motion blur" filter, which averages two successive frames by simply taking the average value for every pixel. This is done successively, such that the actual frame is averaged with an already filtered one.

The second filter is called "temporal smoother", which was applied at strength 10. This filter considers pixel wise the actual frame and the three preceding and following frames. A pixel is averaged, if its grey scale distance to the pixel in the actual frame is lower than a certain threshold determined by the filter strength [Lee03a]. The weight of a pixel is inversely proportional to its grey scale distance. Therefore only close pixels in grey scale space are effectively averaged. In our case the maximum grey scale distance for the filter to have any effect was 64 out of 256 total grey values. A very good result of the filters was achieved, if the combination of the temporal smoother and the motion blur filter were applied twice. The resulting movies are marked by the suffix "ts_mb_x2". These movies

7 Dynamics of Structure Formation

show a highly improved visibility of lattice sites in the perforated lamella phase even for single frames.

7.2.5 Defect Recognition in the PL structure

Selected frames showing the perforated lamellar structure were analyzed by the image analysis algorithm described in chapter 6. The algorithm determines single points in the center of the PL lattice sites. It checks the number of nearest neighbors by constructing Voronoi polyhedra. Defects are detected, if the number of nearest neighbors deviates from 6.

7.3 Results

7.3.1 Overview of the experiment

The film thickness of the swollen film of about 95 nm was chosen in the regime of perpendicular oriented cylinders C_{\perp} . Considering the phase diagram in ref. 5, this film thickness is not stable at the given polymer concentration of $\phi_P \approx 0.73$ and therefore splits into islands and holes. For fully developed holes the stable structure within the holes is predicted to be a perforated lamella. The time evolution of the film was expected to be very slow as known from the ex-situ experiments presented in chapter 5.

Figure 7.2 a) shows the overall time line of the experiment. After injection of solvent vapor the SFM tip was approached to the surface and the tapping parameters were adjusted. The first image with sufficient phase contrast could be taken after approximately 5 minutes after solvent vapor injection. The total measurement time was 20 hours and 41 minutes, resulting in a total of 448 images taken during vapor annealing. A black square is plotted for every frame taken in the upper part of figure 7.2 a) as the sequence called "total". The plot is not continuous since adjustments of the tapping mode parameters had to be done in the case of vanishing phase contrast. All phase images belonging to frames with slow scan direction from bottom to top are included in the movie "upframe_ind.avi". The movie shows the buildup of spherical holes, which drift from bottom to top of the frame in time. The first hole leaves the frame after approximately 7.5 h and a new hole enters the frame from the bottom at about

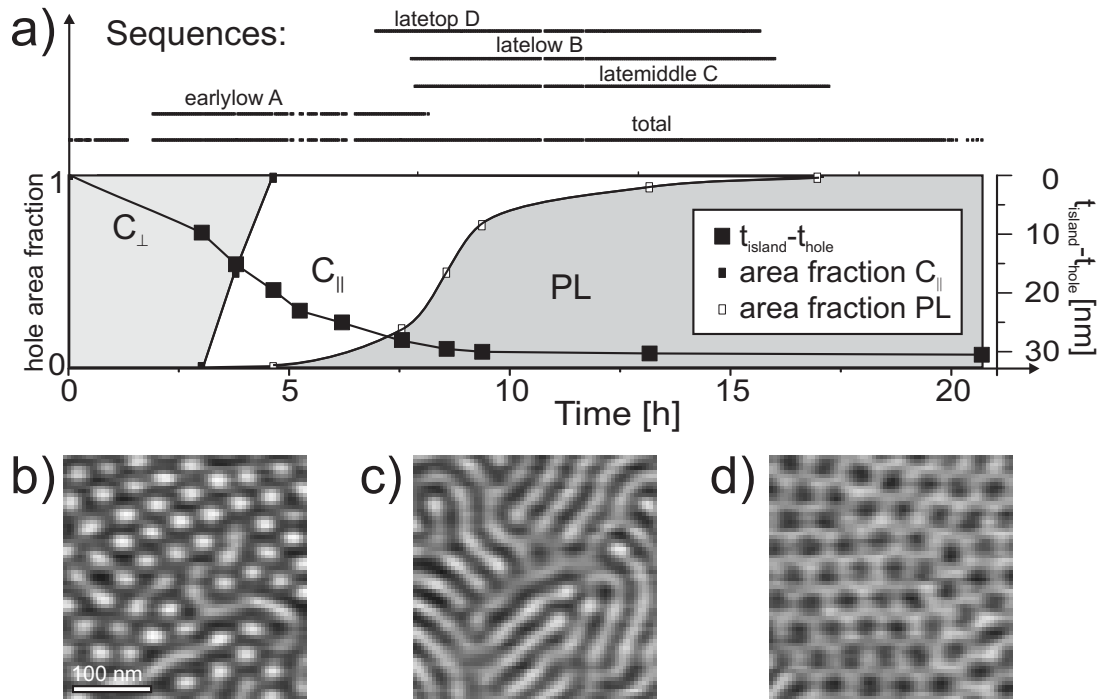


Figure 7.2: a) Position of the captured frames in time plotted as dots along the time axis. The sequence called "total" shows all captured frames, while the other sequences represent the registered frames within the holes used for the movies. Below the sequences the development of the terraces is shown, as measured as difference in height of islands and holes. Also plotted is the partial fraction of the C_{\parallel} and PL phase at the bottom of the developing holes. b) c) and d) depict AFM tapping mode phase images of the structures formed within the holes, namely the C_{\perp} , C_{\parallel} and PL structure, respectively.

the same time.

Here we want to describe the details of the phase transitions at the bottom of the holes. Inside the holes the microdomain structure changes from perpendicular cylinders C_{\perp} seen as white dots to parallel aligned cylinders C_{\parallel} seen as white stripes to a perforated lamellar phase PL seen as dark dots. Sample SFM phase images of all three structures at the bottom of the holes are shown in Figure 7.2 b), c) and d), respectively. These structures have been identified before by comparison to computer simulations in chapter 5.

Different areas of the sample surface were tracked within the holes, rectified, filtered and put into smaller movies. The time line of these partial movies is also shown in Figure 7.2 a). The first one named "earlylow" captures the development of the microdomain structure within the first hole, while the other three are taken

7 Dynamics of Structure Formation

at different spots within the second hole. They are called "latelow", "latemiddle" and "latetop" depending on their position within the hole. For short reference we introduce the abbreviations A, B, C and D for the partial movies in the respective order. The images presented in this chapter are again parts of these movies registered newly and called X_n , where X denotes the capital letter for the movie and n a number for different spots within the large frames.

The deepening of the holes as measured as the vertical distance from island to hole in the SFM height images is shown in Figure 7.2 a). The terrace formation at this polymer concentration is a rather slow process, it takes approximately 10 h to develop its final depth of about 30 nm. The area fractions of the respective structures inside the hole are also plotted in Figure 7.2 a). If the film thickness within the holes approaches a thickness corresponding to a phase boundary in the phase diagram, the transitions to other phases start. The transition from the C_{\perp} to the C_{\parallel} phase takes place at 3 to 5 h after introduction of solvent, while the transition from C_{\parallel} to PL starts immediately afterwards. The completion of the transition to the PL phase takes rather long and ends after approximately 17 h.

7.3.2 Fast Dynamics

The measurement time of a single frame is approximately 153 s. This time resolution is not enough to capture smoothly the fast fluctuations of the microdomain structure. This becomes visible in the unfiltered or Fourier filtered movies, especially for the C_{\perp} phase. The upright cylinders fluctuate around their lattice positions and seem to jump from one position to the next in two adjacent frames. The time to scan one microdomain structure like one upright cylinders can be estimated by the size of the structure of about 8 pixels and the scan speed to approximately 2.4 s. Since the fluctuations of the microdomain structure is still visible in the sequence of the raw data and the local structure in one frame is clearly resolved and only smeared in rare cases, we estimate a lower bound to the time scale of the fluctuations in the order of seconds. On the other hand the time averaged movies show a very continuous movement of the structures without fluctuations. The temporal filters effectively averages over approximately three frames along the time axis, which gives an upper bound to the time scale of the fluctuations in the order of ten minutes. Inside of the microdomain grains

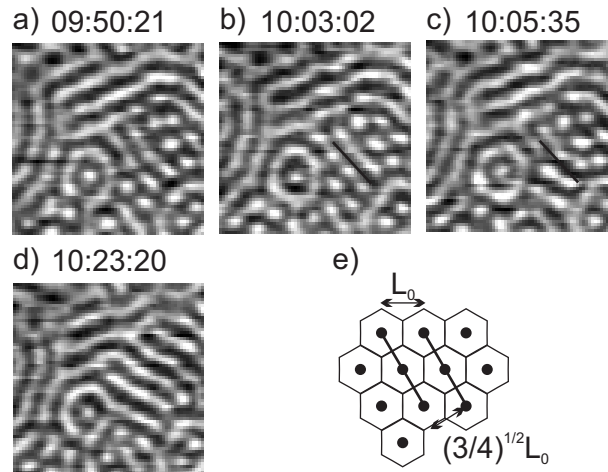


Figure 7.3: a)-d) Fast reorientation process of the local microdomain structure. Images are raw data phase images cut from full frames. The times on top of the frames denote the time after the start of the solvent vapor annealing. The orientation of the local C_{\perp} structure changes within two adjacent frames. The black line is a guide for the eye to estimate the amount of reorientation. e) The reorientation process takes place because of the incommensurability of the structures C_{\perp} and C_{\parallel} (see text). The relevant dimensions of the C_{\perp} structure are shown in terms of the cylinder cylinder spacing L_0 .

the fluctuations are rather small leaving the local microdomain structure intact. They are visibly enhanced at defect sites, for example defects with 5 and 7 neighbors in the hexagonal structures and during the phase transitions. One example of a rapid movement of a few lattice sites is shown in Figure 7.3 a)-d). The figure depicts a reorientation process of the microdomain structure during the phase transition from C_{\perp} to C_{\parallel} . The frames shown in Figure 7.3 a) and b) are 13 min apart and there is almost no change in the structure. The next frame shown in Figure 7.3 c) is the adjacent frame to Figure 7.3 b) and the 6 cylinders around the black line have turned their orientation by approximately 20° . This new orientation is then adapted by the appearing C_{\parallel} phase as show in Figure 7.3 d). Details on the phase transition will be explained in the following section. This rapid movement corroborates the estimate of the upper bound to the time scale of the microdomain fluctuations.

7 Dynamics of Structure Formation

7.3.3 Phase Transition: C_{\perp} to C_{\parallel}

The stable phase within a smooth film of the given initial film thickness is the C_{\perp} structure. In the final state of fully developed terraces this structure exists only at the rim of terraces, at intermediate thicknesses between island and hole, as discussed in chapter 5. This effect has been attributed to an incommensurability of the natural layer spacing of the C_{\parallel} microdomain structure to the film thickness. The observation of the C_{\perp} phase inside a planar film confirms the assumption that the film thickness is the decisive parameter for the structure formation. The existence of the C_{\perp} structure in the terrace step in turn means that the local structure inside the step is not largely influenced by the gradient in film thickness.

The planar film is not stable against thickness variations of the film. In simple SST theory the free energy per unit area of the C_{\perp} structure is found to be independent of film thickness (see chapter 4), while the free energy of the C_{\parallel} phase is lower in the case of a film thicknesses, which is commensurate to the natural layer thickness of the C_{\parallel} phase. Therefore thickness fluctuations of sufficient amplitude grow and the film forms islands and holes. On top of the islands and on the bottom of the holes the C_{\perp} structure transforms into more stable structures.

The transition from C_{\perp} to C_{\parallel} can be followed through the first 5 h of the *in-situ* measurements. After three hours the thickness of the film inside the holes has reached a value at which the C_{\parallel} structure becomes stable. In the phase diagram shown in chapter 5 this film thickness corresponds to the phase boundary of the C_{\perp} and C_{\parallel} phase at $\phi_P \approx 0.73$.

Figure 7.4 shows the transition for two square areas cut from the movie "early-low A". The white lines drawn into the frames depict the resulting orientation of the C_{\parallel} structure and enable a comparison to the orientation of the C_{\perp} structure before the transition. The phase transition takes place by an interconnection or coalescence of the upright cylinders to form a lying cylinder. The upright cylinders first elongate in the plane of the film to neighboring cylinders and finally coalesce. Afterwards the phase contrast is still modulated along the cylinder axis indicating thickness variations of the in plane cylinders. We interpret these thickness undulations as cylinders with necks as found earlier in similar films in our group [Kon00], since the film at this stage is still thicker than a single layer

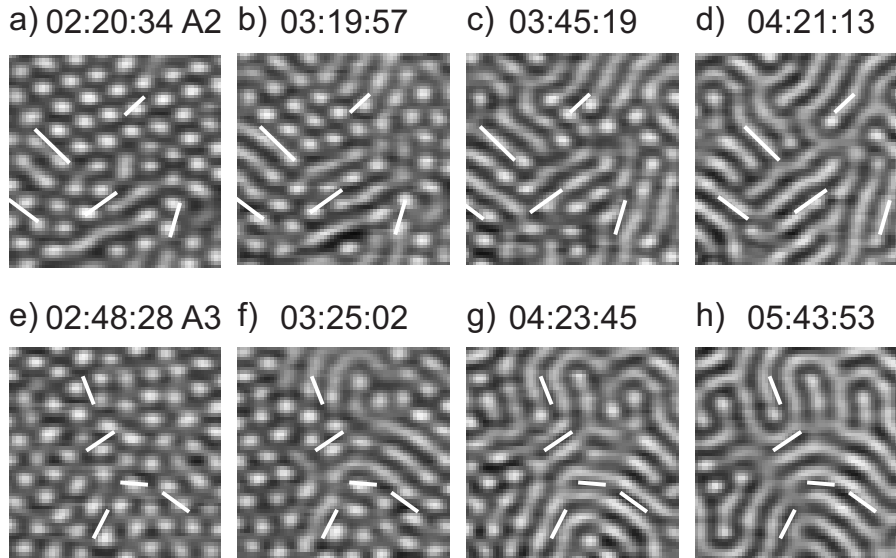


Figure 7.4: Phase transition from C_{\perp} to C_{\parallel} for two examples of movie A2 a)-d) and movie A3 e)-h). The times above the frames denote the time after injection of solvent vapor. The orientation of the C_{\parallel} domains is marked in all images as white lines for better comparability to the orientation of the C_{\perp} grains.

of cylinders. The coalescence of C_{\perp} cylinders occurs first preferentially at grain boundaries in the C_{\perp} structure, which are sometimes already decorated by in plane cylinders. Simultaneous to this process, similar transitions are induced for the cylinders on both sites of the first one, which then align parallel to the first one.

This path has important consequences to the resulting C_{\parallel} phase. As shown in Figure 7.3 e) the cylinder-cylinder distance in the C_{\perp} phase is denoted as L_0 . If the transition proceeds by interconnecting these cylinders, the spacing of the in plane cylinders will only be $\sqrt{3}/2 L_0 \approx 0.87 L_0$. The equilibrium spacing of the cylinders in the C_{\parallel} phase is estimated to be slightly smaller than L_0 . In the simple SST treatment discussed in chapter 4 the perpendicularly oriented cylinders assume bulk spacing, while the spacing of the in plane cylinders is ≈ 3 percent smaller for the first layer of cylinders. Measurements of the cylinder spacing in the different phases of terraced films have been presented in chapter 6. While the spacing measured for the C_{\parallel} structure is consistent with the SST predictions, the C_{\perp} structure shows a larger spacing as found in the bulk.

The initial grains of the C_{\parallel} phase are therefore formed with an unfavorably reduced spacing of the cylinders. This has important consequences for the further

7 Dynamics of Structure Formation

growth of this phase. First of all the C_{\perp} structure cannot simply transform into the C_{\parallel} structure by interconnecting cylinders without inducing strain. Therefore the transition takes place rather slowly and not uniformly starting from a single nucleus. Instead other nuclei are formed at rather close places. Due to the low symmetry of the C_{\parallel} phase and the induced strain field these nuclei will grow in majority in a different direction. The outcome is a much smaller grain size of the C_{\parallel} phase in comparison to the C_{\perp} grain size before the transition.

The grains try to relax their spacing by rotating the cylinders in the plane of the film. This can be seen in Figure 7.3 as described earlier. In this example the cylinders rotate by an angle of approximately 20° , which obviously relaxes the cylinder spacing. The rotation of the cylinders can also be seen by comparing the directions of the grains in the C_{\parallel} phase to the direction of the grains in the C_{\perp} phase recorded earlier. Almost all grains adapt a new direction.

The final grain size is typically not larger than 3 to 4 cylinder spacings. The resulting C_{\parallel} grain structure reflects the symmetry of the hexagonal C_{\perp} phase only in part since most of the grains have rotated. Further healing of the C_{\parallel} phase could not be observed in this experiment since the transition to the PL phase took place immediately after the transition to the C_{\parallel} phase was completed.

7.3.4 Transition from C_{\parallel} to PL

Figure 7.5 depicts the first development of PL lattice sites for three different areas inside the hole in a series of four images per spot. The first frame shows only the C_{\parallel} phase, while the third frame shows already single rings of PS rich microdomains, which we consider as first PL lattice sites. The position of these grains in the third frame are marked by the white circles, which are also drawn in the other frames at the same positions. The images suggest that these first instances of the PL structure are stabilized by grain boundaries of the C_{\parallel} phase. They occur at the boundary of usually more than two C_{\parallel} grains, which are decorated with defects like T-junctions of the in plane cylinders. These defect rich areas act as nuclei for the PL phase.

Before the first PL lattice sites are formed, a zigzag structure of PS-rich material is seen in the images as marked by the white ellipses drawn into the images. The structure may be divided into substructures, which have three arms interconnecting to adjacent cylinders as depicted in Figure 7.5 a). As pointed out

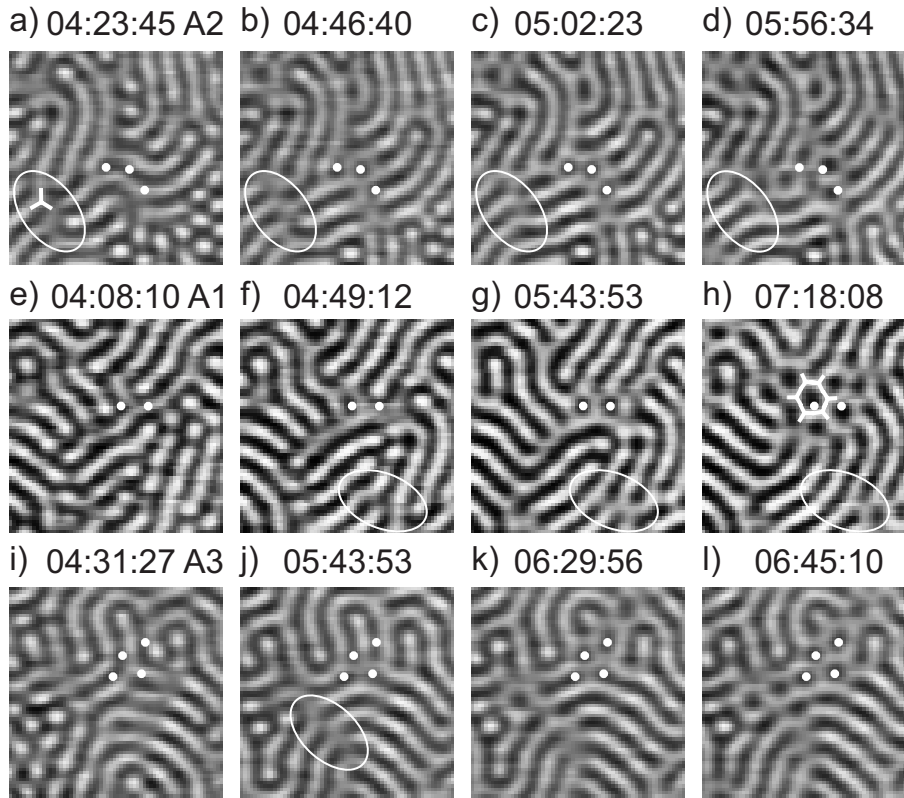


Figure 7.5: Nucleation of the PL phase inside the $C_{||}$ phase for three different spots. The position of the first occurrences of the PL phase are marked by white dots. The nucleation takes place at grain boundaries of the $C_{||}$ phase, where the local structure already supports the formation of PL sites.

by Matsen [Mat97] the complex phase PL is build up from elementary units formed by three jointed struts. The struts themselves are similar to the cylindrical minority domains of the $C_{||}$ phase. Those elementary units resemble the interconnections found in our experiment and build up the threefold coordinated PL lattice as depicted in Figure 7.5 l). In other words one PL perforation site consists of 6 of the elementary units and the interconnections might be considered as first instances of the PL phase.

The interconnections establish a continuous PS-rich phase in the plane of the film. These connections should enhance the diffusion of the block copolymer molecules, since tunneling or hopping of the minority block is not longer necessary for diffusion in any direction parallel to the substrate. Tunneling of A block through a B-rich microdomain is by orders of magnitudes slower than diffusion along microdomains as has been shown for films of lamellar forming block

7 Dynamics of Structure Formation

copolymers [Shu91]. The interconnection of the cylinders therefore enhances the healing of the surrounding microdomain structure. In some cases this results in a better alignment of the C_{\parallel} phase and the interconnections disappear as can be seen for example from Figure 7.5 g) and h).

Since the interconnections sometimes dissolve again at this stage of the experiment, we conclude that the film is still in the existence region of the C_{\parallel} phase. The first appearance of PL lattice sites happens actually in this phase since the high amount of C_{\parallel} lattice defects is very unfavorable. This assumption is corroborated by the slow increase in the area covered by the PL phase at this stage as shown in Figure 7.2 a).

After establishment of the first grains the PL phase grows along the grain boundaries of the C_{\parallel} phase as seen in the forth frame in Figure 7.5. Thereby the already existing sites may shift their position to optimize their environment for the creation of new sites, which explains the shifted positions of the lattice sites in Figure 7.5 d) and h). Once the new PL grain has reached a sufficient size of about 3 to 4 lattice sites in diameter the holes start to rearrange again to form more perfect grains.

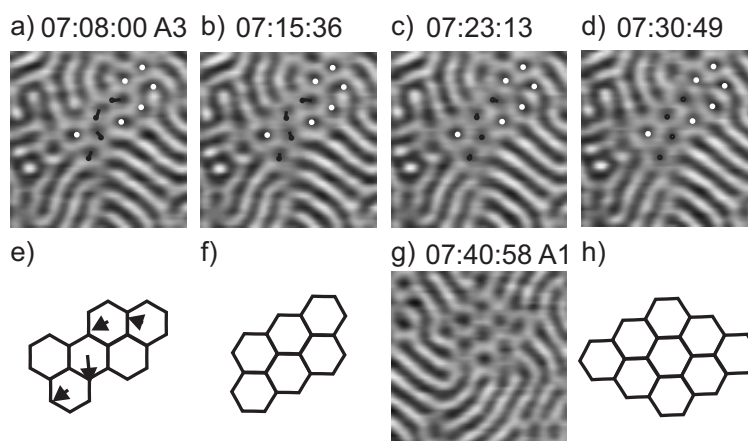


Figure 7.6: a)-d) Reordering of a PL grain to minimize the PL - C_{\parallel} boundary. e) and f) show sketches of the grain structure before and after the movement of the four central sites. g) and h) shows another grain with minimal interface and the corresponding sketch. The PL structure always arranges such that any interface to the C_{\parallel} structure is along the PL lattice lines.

One example of this process is depicted in Figure 7.6 a)-d). The white dots mark the rather static domains, while the black dots and lines mark the movement of a line of 4 PL lattice sites. Figure 7.6 e) and f) show the initial and the

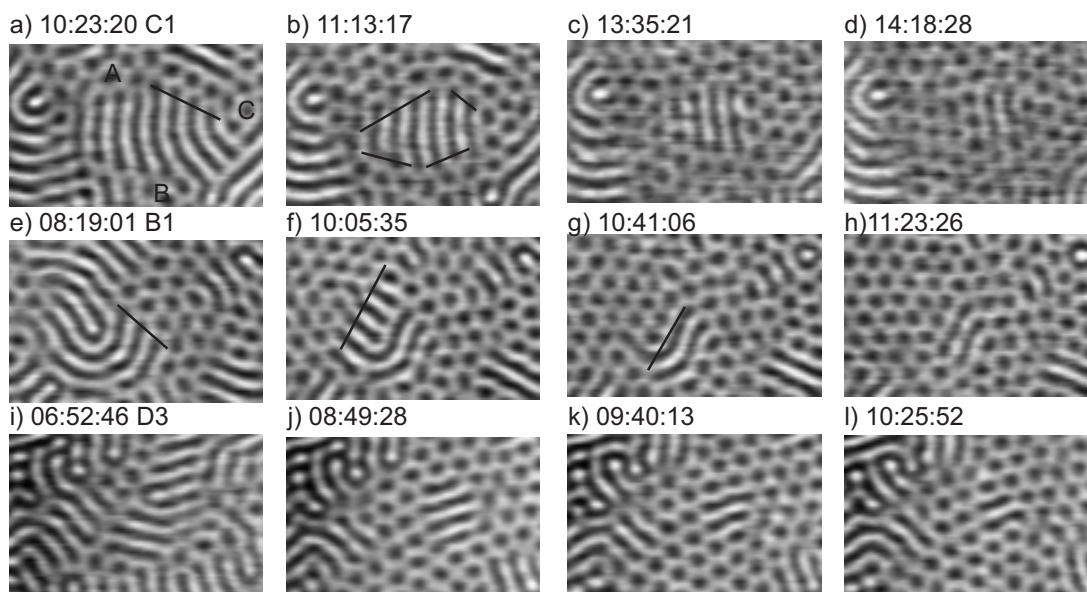


Figure 7.7: Three examples of the growth of the PL grains in time. Capital letters denote the origin of the PL grain formation. The grain growth along the $C_{||}$ grain boundaries, leaving isolated grains of $C_{||}$ behind. The filling of the $C_{||}$ grains leads to the formation of defects in the PL phase.

final state schematically. The initial state consist of a grain of PL microdomains with rather large interface to the surrounding $C_{||}$ phase. The cooperative movement of the four domains effectively rotates the orientation of the grain. The final grain consists of two rows of PL microdomains, which yields the best ratio of grain surface and grain area. The boundaries of this grain are all along the PL lattice, which seems to be the most favorable boundary. A similar grain and its schematic representation is shown in 7.6 g) and h). This grain also has only interfaces to the $C_{||}$ structure parallel to the PL lattice lines. The general concept is the minimization of the PL grain interface to the surrounding $C_{||}$ phase.

The now established grains of the PL structure tend to further grow along the grain boundaries of the $C_{||}$ phase. This process takes place around 7 hours after introduction of the solvent vapor and is the most effective part of the transition to the PL phase as seen by the steep slope in the area fraction of the PL phase in Figure 7.2 a). The film thickness inside the hole has reached a value within the existence range of the PL structure.

Figure 7.7 shows three examples of the further development of the PL phase. In Figure 7.7 a) and b) the PL phase starting points are marked by A, B and C.

7 Dynamics of Structure Formation

The domain size of the C_{\parallel} structure is comparatively large in this example. This sequence is another example of the PL growth along the grain boundaries of the C_{\parallel} structure. In Figure 7.7 b) all boundaries are decorated with PL lattice sites. Again all PL boundaries are formed along the PL lattice lines as marked by the black lines in the images.

The remaining C_{\parallel} grains all have similar architecture, which resemble the PL grains described above. Figure 7.7 b) and j) show rather perfect grains. Note that the grains are elongated perpendicularly to the in plane cylinders. This elongated shape was also found inside the well ordered C_{\parallel} structure as discussed in chapter 6. Elongated grains have been found before [Har02, Has95] and have been attributed to the high penalty for layer compression and dilation, which favors molecular splay over molecular bend [Har02]. These optimal grains are rather stable against a transition to the PL structure since again both lattices are not commensurate. This has been discussed before (see chapter 6) and can also be seen in Figure 7.7 c) and j). In Figure 7.7 j) the C_{\parallel} grain shows 4 lying cylinders, where the PL grain to the right, which is oriented in the same direction, shows only three rows of PL cells. The C_{\parallel} lattice spacing is therefore significantly smaller than the one of the lines of holes in the PL phase.

The filling of the C_{\parallel} grains proceeds by a distortion of the C_{\parallel} lattice to fit to the PL structure. The in plane cylinders next to a PL boundary first show undulations corresponding to the PL spacing and then eventually transform to PL sites. The orientation of the PL grains surrounding the C_{\parallel} grains plays also an important role. The PL grains have random orientation and usually cannot fill the C_{\parallel} grain without introducing defects into the resulting PL lattice. Note that the maximum mismatch in the orientation of PL grains is 30° due to the 3-fold symmetry of the lattice.

7.3.5 Defect Movement in the Perforated Lamellar Phase

Before we continue to describe the details of defect movement in our experiment inside the PL phase, we want to discuss the most common defect processes in 2D hexagonal systems.

Figure 7.8 a)-d) depicts three interconnected reversible processes [Mar96]. The centers of the unit cells are marked by black squares, while the black lines show the Voronoi polyhedra for every PL lattice cite. The grey lines in the background

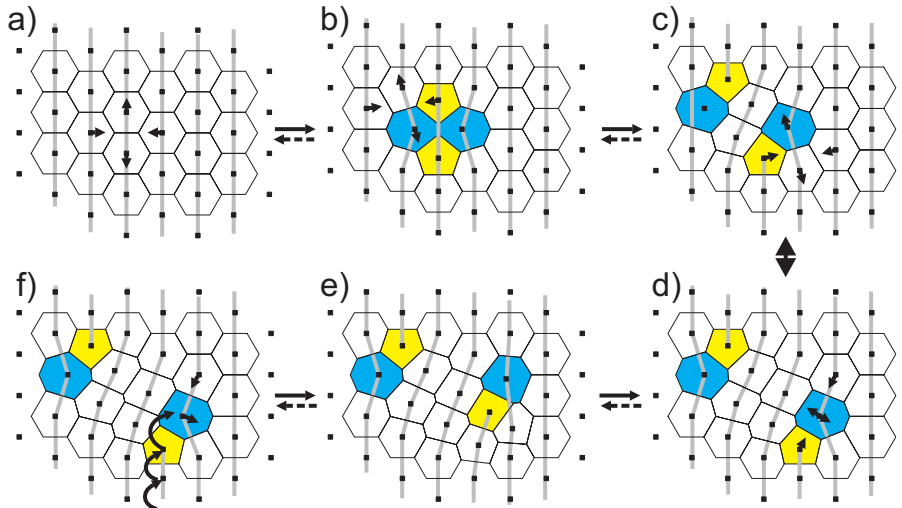


Figure 7.8: Schematic representation of the basic processes involving defect formation and translation. a)-b) Formation (annihilation) of a paired dislocation. b)-c) Unbinding (binding) of the paired dislocation. c)-d) dislocation glides. d)-e) creation (annihilation) of a additional lattice site f)-e) movement of a dislocation line by lattice site jumps. d)-e) and f)-e) denote two possible processes of a dislocation climb.

mark the lattice vector registry. The processes shown are (reversed processes in brackets): a)-b) the nucleation (annihilation) of a bound dislocation pair, b)-c) the unbinding (binding) of a dislocation pair and c)-d) the translation of a free dislocation perpendicular to its axis called "dislocation glide". Figure 7.8 e) shows a state, which can only be reached by a translation of a dislocation pair along its axis called "dislocation climb". Two possible processes to reach this configuration are shown in Figure 7.8 d) and f). The first process d)-e) involves a splitting (merging) of one lattice site into two, while the second process involves positional jumps of an entire row of lattice sites as marked by the black arrows. The effect of both processes is an elongation (shortening) of the dislocation line, which terminates at the fivefold site.

Most of the processes shown can be found in the experimental data. A high density of defects is induced by the phase transition from the $C_{||}$ to the PL phase. Figure 7.9 shows a few examples of movements of defects in the PL phase right after filling remaining $C_{||}$ grains. The most common process is the dislocation glide. In Figure 7.9 a)-c) a phase boundary between the upper PL grain and the lower PL grain is decorated by two dislocations. In the three images already

7 Dynamics of Structure Formation

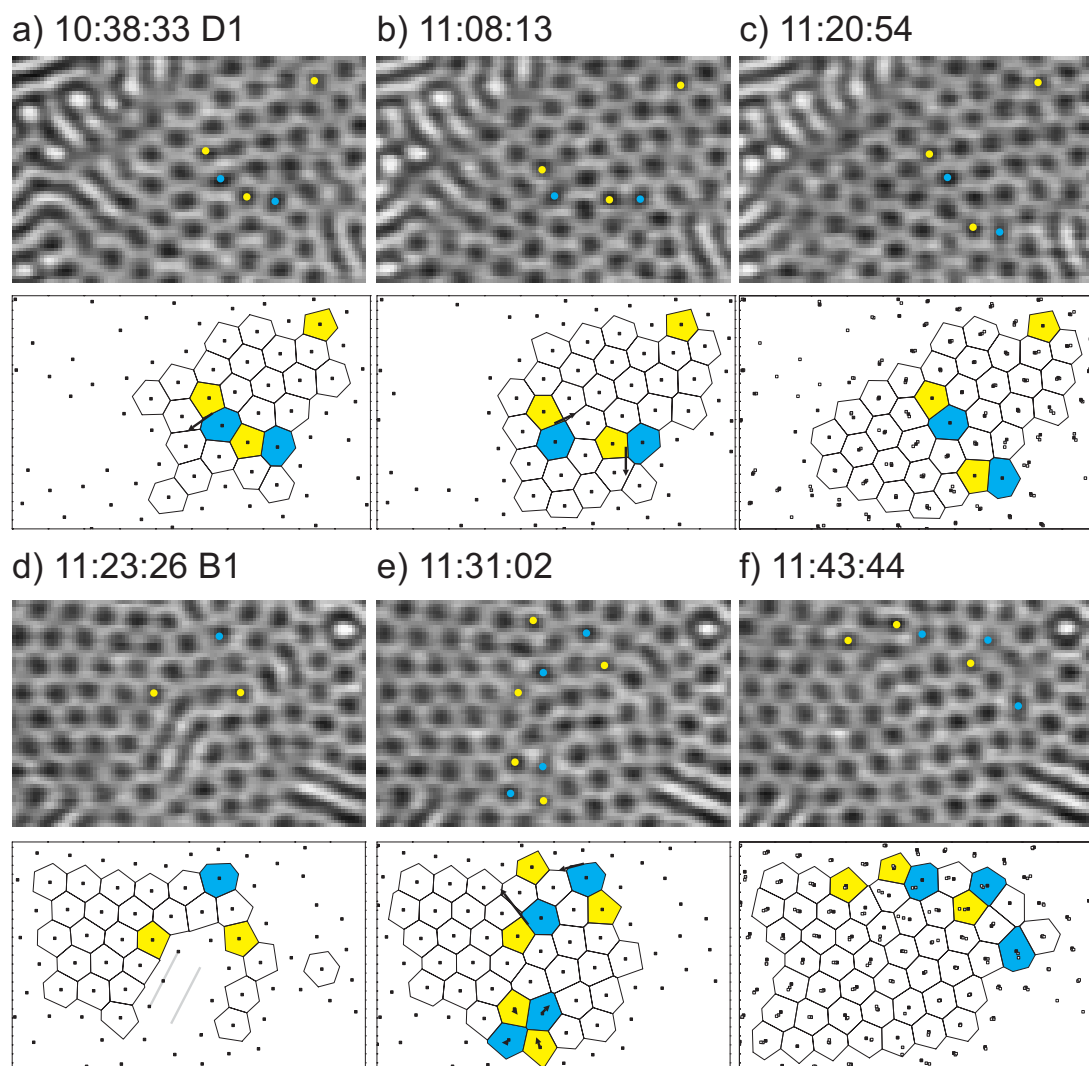


Figure 7.9: Two sequences of frames, which depict the experimentally found processes of dislocation glides. Below the frames the Voronoi polyhedra for the respective frames are shown to increase the visibility of the defects. In the last frame of both examples the positions of the previous lattice sites are included marked by white (first frame) and grey (second frame) squares. d)-e) show additionally the annihilation of a paired dislocation at the bottom of the frame.

three dislocation glides can be found as marked by long black arrows. The time scale of these glides is rather small, faster than the frame capture time. These glides involve the movement of only a few lattice sites as depicted in Figure 7.8 c). Figure 7.9 d)-f) shows the annihilation of a bound dislocation pair. The bound dislocation is nucleated by the phase transition of a C_{\parallel} grain to the PL structure. Note that there are only 2 frames in between the ones shown in Figure 7.9 d) and e). The bound dislocation is annihilated very fast. There are no events of an unbinding of a bound dislocation pair found in the experiment. In Figure 7.9 f) the positions of the sites of all three images is plotted so one can follow the path of the sites. Only the movement of the dislocation pair sites to the right is significant.

A few minutes after the completion of the phase transition only dislocations can be found as defects in the PL phase. There were no occurrences of single disclinations, which might form from dislocations by disclination unbinding [Mar96]. This is an indication that our perforated lamellar phase has no liquid order but rather a hexatic or crystalline order. Nevertheless a precise analysis of the state of order includes the calculation of order parameters and their correlation functions and is beyond the scope of this chapter.

It is also noteworthy that no vacancies or interstitial sites have been found in our experiment. We attribute this fact to the liquid like, self organizing nature of our material. Both defects include a local decrease of density of one of the blocks, which is prevented by the composition of the polymeric chains. If the density of sites is not close to the equilibrium value the polymer can react by building new sites or annihilating sites instead of creating vacancies and interstitial sites.

The creation and annihilation of lattice sites is shown in Figure 7.10. The top two examples show the creation of a new lattice site at a dislocation, while the bottom image shows the annihilation of a site. Both processes represent dislocation climbs, which are shown as red arrows in the Voronoi constructions. Dislocation climbs in a hard sphere system involve the movement of a whole dislocation line as shown in Figure 7.8 f) [Mar96]. In our system a obviously more effective process is the creation and annihilation of lattice sites. Nevertheless this process is still not very probable. The three examples shown are the only ones found in the experiment.

Note that the creation and annihilation increases and decreases the density

7 Dynamics of Structure Formation

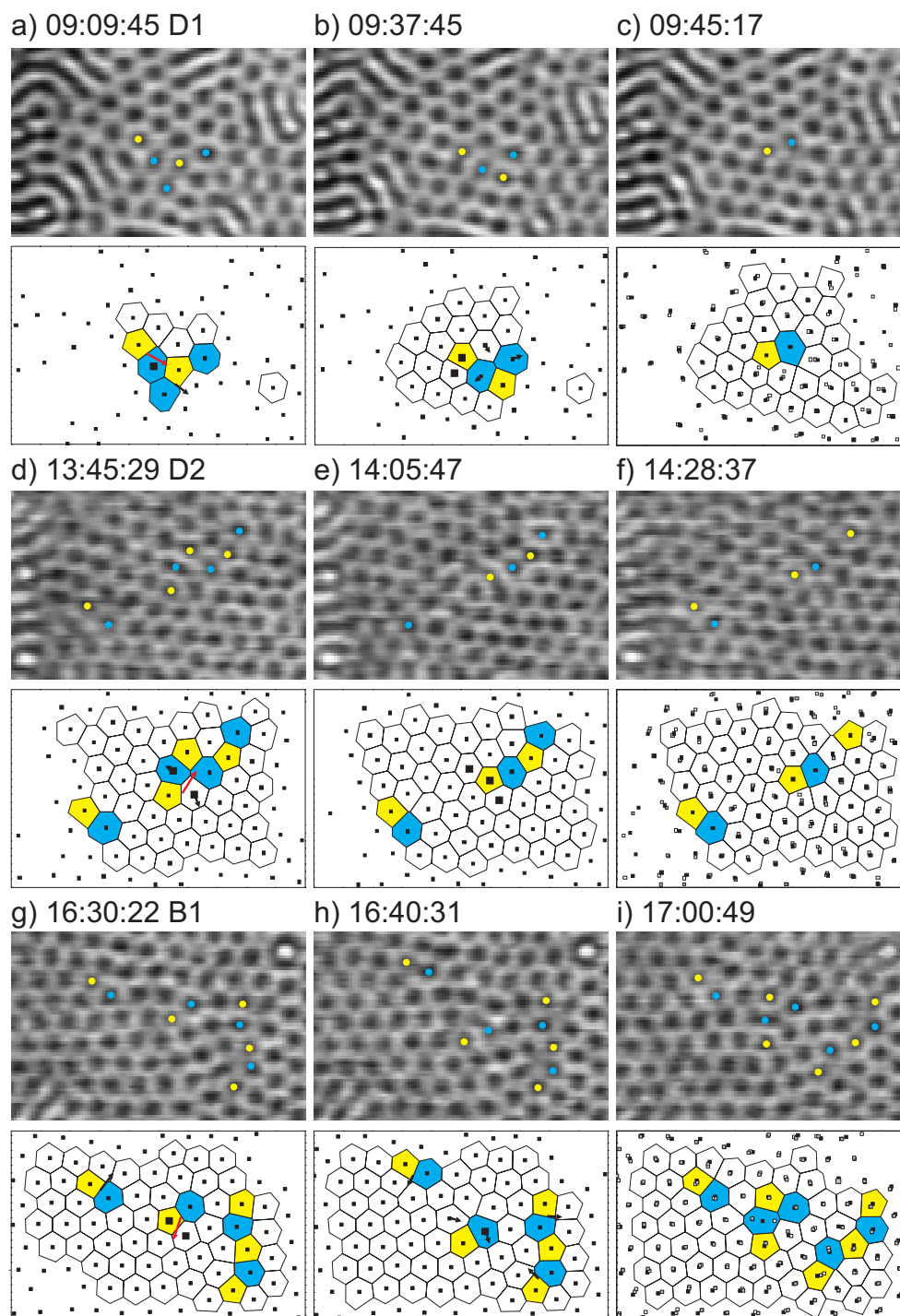


Figure 7.10: Three processes of dislocation climbs found experimentally. a)-c) and d)-f) show the creation of additional lattice sites, while g)-i) show the annihilation of a lattice site. Creation and annihilation of sites is the predominant mechanism of dislocation climbs in our system.

of lattice sites inside the PL structure. The two processes of hole formation take place before the single occurrence of site annihilation. A possible reason for this is the healing of the structure in early stages, which reduces the density of holes and thereby induces the formation of new holes. At later times the healing process becomes very slow and both processes become equally likely.

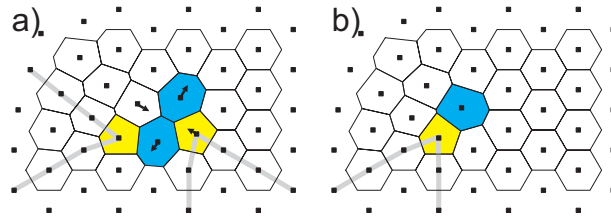


Figure 7.11: Reversible process of the annihilation of two extra half rows of material. Two dislocations oriented parallel to each other under an angle of 120° transform into one dislocation with its axis along the remaining lattice direction. The process may also be seen as a dislocation pair annihilation on top of the remaining dislocation.

In all three processes depicted in Figure 7.10 there is another elementary and reversible defect process involved, the annihilation or creation of two half rows of lattice sites. Figure 7.11 shows this process schematically. The starting situation is the presence of two dislocations, which are oriented in an angle of approximately 120° to each other as shown in Figure 7.11 a). A slight adjustment of 4 lattice sites as marked by the black arrows annihilates both dislocations and a new dislocation of intermediate orientation is created. Thereby two extra half rows of material originating from the starting dislocations merge and annihilate as marked by the grey lines in Figure 7.11. The remaining lines reflect the orientation of the new dislocation.

In the first example of the experimental observations shown in Figure 7.10 a) the dislocation glide serves two reach the configuration of the defects for the process described above. In the second example the newly created dislocation climbs while in the third example a dislocation transforms into two after a dislocation climb with the reversed process. The presence of the dislocation climbs in all three situations suggests that this process provides the necessary adjustment of the density of lattice sites.

The process of dislocation line annihilation should be very essential in the process of healing of hexagonally ordered 2D structures. It describes the annihilation of one dislocation out of two thereby effectively rotating the orientation of the

7 Dynamics of Structure Formation

remaining one. This process therefore efficiently complements the annihilation of two antiparallel dislocations shown in Figure 7.8 b).

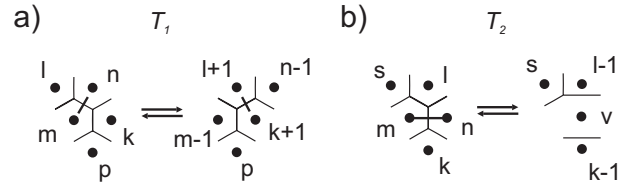


Figure 7.12: T_1 and T_2 processes [Sag93]. The letters denote the number of nearest neighbors at each site. Both processes conserve topological charge.

All processes described in this chapter correspond either to a T_1 or a T_2 process [Sag93] as depicted in Figure 7.12 a) and b). All processes not involving a dislocation climb are T_1 processes. They involve the movement of four lattice sites where two diagonally lying sites are nearest neighbors and the others are not. The two nearest neighbors move apart while the other two lattice sites move closer thereby effectively exchanging nearest neighbors as shown by the black solid lines in Figure 7.12 a). The pure T_1 process in a perfect hexagonal lattice ($l = m = n = k = p = 6$) corresponds to the formation of a paired dislocation as shown in Figure 7.8 a). The dislocation unbinding ($l = n = 6$, $m = 7$, $k = p = 5$) dislocation glide ($l = n = p = 6$, $m = 7$, $k = 5$) and annihilation of two extra half rows of material ($k = 6$, $m = n = 7$, $l = p = 5$) are similar T_1 processes with different starting situations. T_1 processes conserve the topological charge, the number of lattice sites and bonds. The T_2 process involves the merging (splitting) of two lattice sites and is seen in our experiment as dislocation climb ($k=6$, $l=7$, $m=5$, $v=7$). It thereby eliminates (creates) one site and three bonds. Both processes conserve topological charge and the total Burgers vectors [Sag93]. Although this classification simplifies the description of defect processes it does not give general rules for the activation energies of the single processes, which clearly depend on the surrounding strain field induced by the dislocations [Mar97].

Dislocation climbs have been proposed to effectively transport material in a block copolymer system with spherical minority domains [Seg03]. In this study we actually observe dislocation climbs but we think they occur for other reasons. In contrast to the sphere forming system our system has continuous phases of both blocks in the plane of the film, which makes hopping or tunneling of blocks

redundant. Therefore the necessary transport of molecules from the holes to the islands should not be limited by the microdomain structure in our system. We also observe a merging of two lattice sites, which would effectively induce transport of material into the hole and therefore corroborates our assumption.

7.4 Conclusion

In conclusion we have followed *in-situ* in real space and real time the phase transitions inside a thin film of cylinder forming block copolymers. During annealing with a controlled atmosphere of chloroform vapor the film developed islands and holes. The development of the microdomain structure and its spacial fluctuations were captured. The rather high polymer concentration in the thin film results in a time scale of the fluctuations in the order of seconds to minutes. The decreasing film thickness inside the holes triggers phase transitions since stable phases are a function of the thickness of the film. Since the film thickness decreases rather slowly, the phase boundaries are also approached gradually, in contrast to temperature quenches in bulk experiments. We find that the grains of new phases nucleate preferably at defect sites induced by grain boundaries of more than two grains of the original phase and then grow along the grain boundaries. For both transitions the original and the new structure are not commensurable, which induces reorientation processes in the new phases. The grain size in the new phase is dependent on the symmetry of the phase and therefore smallest for the C_{\parallel} phase. The grains of the C_{\parallel} phase heal efficiently close to the phase boundary to the PL phase, since defects are replaced by threefold interconnections of the cylinders, which may be considered as elementary units of the PL phase. We attribute this effect to an enhanced diffusion of molecules along these interconnections. The same effect enhances the healing of the PL structure since this phase is continuous within the plane of the film both in the PS rich phase and PB rich phase.

The healing is mediated by the movement and annihilation of dislocations in the PL phase. The most common process is the dislocation glide. Dislocation climbs are rare and take place by the formation or annihilation of lattice sites and are always accompanied by the annihilation or creation of two half rows of material, respectively. This process effectively annihilates two dislocations of

7 Dynamics of Structure Formation

different orientation and creates a new dislocation with intermediate orientation conserving the Burgers vector. This process therefore efficiently complements the annihilation of antiparallel dislocations.

7.5 Appendix: Registration, Alignment and Filtering

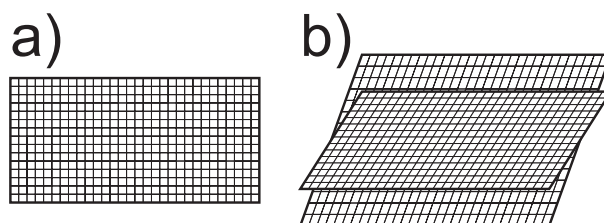


Figure 7.13: Illustration of the non orthogonal lattices used to remove distortions induced by the non linearity of the scanning. Two parameters are used to create the new lattice: shearing about top and bottom line and stretching along the y direction.

As we saw in the previous section the raw data has to be treated to enhance the visibility of the dynamics of small scale and mesoscale effects in the data. One reason is the mechanical setup, which is rather stiff and increases the inherent creep and hysteresis effects of the piezo actuators. Also the thermal drift in the system is rather large compared to the time scale of the experiment. Another obstacle is the pickup of material during the measurements by the tip, which has been already minimized by applying suitable AFM-parameters like fast scanning and very light tapping. Nevertheless typical artifacts visible as white horizontal lines in the raw data have to be reduced to enhance the image quality and to make further analysis possible.

The aim of the alignment procedure was to track a specific part of the sample surface along the time axis. The first step is to define a rectangular area inside of a chosen frame. This rectangular area should then be tracked in all following and previous images. Furthermore the distortions due to creep and hysteresis of the setup should be removed.

The first step has been realized as follows: A chosen rectangle was cut from a suitable frame by setting all pixels outside the rectangle to zero. Then this image is cross correlated to the following image. The cross correlation image has the

7.5 Appendix: Registration, Alignment and Filtering

maximum at the pixel position, which corresponds to the offset of both images where the overlap is optimal. To optimize the position of the maximum to non integer values, the 3 pixels around the center pixel in x and y direction were fitted with a polynomial of second order. In this way a non integer displacement of the rectangle in the next frame is found. For the next frame a similar rectangle is calculated for the non integer center position by linear interpolation of the pixels. Then the procedure is repeated to all following and previous frames. The result is a "path" of the non integer center position of the rectangles through the time line of the images.

The next step is to remove the distortions induced by the nonlinear scanning from the rectangles. The analysis of these artifacts in the images yields that the major distortion is a stretching or compression of the image in the direction of the slow scan axis, i.e. in y direction. This effect is most pronounced at the top and bottom border of each frame. A second distortion considered here is a trapezoidal distortion equivalent to shearing the image with shearing plates at top and bottom of the rectangle. Both distortions are shown in Figure 7.13 b). The corrected images are therefore sampled on a non orthogonal lattice. Since the new lattice again has non integer values, the pixel values are again linearly interpolated.

The procedure of removing these distortions is similar as in step 1. The first step is to take one frame and define the starting values describing both distortions for this frame, i.e. both parameters are set by hand to produce an initial frame with minimal distortions. To check the quality of the distortion removal the Fourier transform of the rectified image is performed and optimized to a circular shape of the most prominent wavelength by adjusting both parameters.

For the next frame a range of distortions for both parameters is considered. In our case both parameters were sampled symmetric to the parameters of the preceding frame in a range of about ± 14 pixels in each direction with a total of 7-10 steps. For each of the trial distortion pairs a new frame was interpolated and compared to the previous frame via calculating the cross correlation image as described above. The cross correlation maximum then was plotted as a function of the two parameters and a best pair of distortion parameters was obtained by finding the maximum in this plot. This is done in a similar fashion as described above for the registration of frames. The cross correlation of the newly corrected

7 Dynamics of Structure Formation

frame and the previous frame gives also a new offset of both frames and corrects the path of center positions. This procedure is repeated for all frames following and preceding the first frame. The result is a path of optimal values for positions and distortions of the rectangular frame through the original data.

It turned out that the procedure described above worked most reliably on the Fourier filtered frames. For these frames the path was found and then applied to the raw data of the measurement. Then the subsequent time averaging procedure was performed as described above.

8 Summary

The equilibrium and dynamic phase behavior in thin films of cylinder-forming block copolymers has been studied. The results range from an extension of an advanced strong segregation theory to the treatment of cylindrical microdomains in a thin film, over the detailed analysis of the phase behavior and the microdomain dimensions of a cylinder forming model system, to the first *in-situ* measurements of phase transitions and microdomain dynamics in a thin block copolymer film.

The first result concerns the characterization of thin films of the model system, a polystyrene-*b*-polybutadiene-*b*-polystyrene (SBS) triblock copolymer, by tapping mode scanning force microscopy (TM-SFM). We present a procedure to establish reliably with TM-SFM the true surface topography of a soft polymeric sample. The measurement of an array of amplitude phase distance (APD) curves enables us to distinguish quantitatively between the “real” surface topography and lateral differences in tip indentation. We find that conventional TM-SFM height images are not necessarily reflecting the surface topography of the sample. In the case of SBS we find that the surface is flat and that conventional TM-SFM height images only reflect lateral differences of tip indentation. Changes in height and phase contrast could be attributed to the crossover between regimes, where attractive and repulsive forces, respectively, dominate the tip-sample interaction. Laterally resolved quantitative determination of indentation depths finally enables one to estimate the thickness of “soft” surface layers on such tiny structures as block copolymer microdomains.

A theoretical treatment of the phase behavior in thin films of cylinder forming block copolymers within an advanced strong segregation theory (SST) framework of Olmsted and Milner [Olm94] is developed. Although the theory is strictly valid only for highly stretched chains and does not account for minority domain structures other than cylinders, the predicted results are in good agreement to the experimental results in this thesis. The microdomain structures under consideration are in plane oriented cylinders terminating with either the matrix component

8 Summary / Zusammenfassung

C_{\parallel} or a half cylinder $C^{1/2}$ at the surface and cylinders oriented perpendicular to the film C_{\perp} . The treatment involves the calculation of the free energies per molecule and per unit area of distorted unit cells of hexagonally ordered cylinders. The planar nature of the thin film interfaces induces such a distortion in the C_{\parallel} phase, resulting in an increased free energy and in microdomain spacings deviating from the ones in bulk for this structure. This in turn enhances the stability region of the C_{\perp} phase at low attraction of the majority block to the surfaces. The stability of this phase is also enhanced if the film thickness is not commensurable to the preferred spacing of cylinder layers of C_{\parallel} and $C^{1/2}$. Half cylinders at the surface are stabilized by a preferential attraction of the minority block to the surfaces.

The thin film phase behavior of concentrated solutions of SBS in chloroform is studied. The stable phases are mapped as a function of film thickness and polymer concentration ϕ_P . The variation of ϕ_P can be interpreted as a variation of the molecular interactions between the two polymer components and between the components and the boundary surfaces. The preferential attraction of the majority component to the surface, the surface field, causes the cylinders to align parallel to the plane of the film, whenever the thickness fits an integer multiple of cylinder layers. At intermediate thickness the cylinders align perpendicular to the film plane. At higher polymer concentration, i.e., at stronger surface fields, a perforated lamella (PL) of polystyrene forms. The surface field needed for PL formation increases with increasing film thickness. This corroborates simulation results that indicate a decay length of the surface field of about one microdomain spacing [Hui01, Hui00, Kno02, Hor02]. A wetting layer exists underneath all films, which either consists of pinned molecules or of a half lamella.

The experimental results are in excellent agreement with both, the strong segregation theory presented in this thesis and computer simulations based on dynamic density functional theory [Kno02, Hor02]. An exception is that the SST treatment cannot make predictions about the PL phase, since this structure is not considered by the theory.

Furthermore the principal microdomain spacings of the thin film microdomain structure are investigated in detail and compared to the SST results. A new image analysis algorithm provides the recognition and the localization of the different structures in the SFM phase contrast images. The microdomain spacings

are discussed as a function of various parameters like the film thickness, the polymer concentration and the local curvature of the structure. An examination of the dependence of the spacing in the C_{\parallel} structure from the local curvature of the cylinders yields an effect of second order, which can be explained in terms of density conservation of the polymer blocks.

The spacing of the C_{\parallel} structure also depends on the local thickness of the thin film. The C_{\parallel} phase is stable in a certain thickness range close to its preferred thickness. Within this range it has to adapt the cylinder "height" to be commensurable with the film thickness. Minimization of the interface between the blocks leads to a smaller or larger lateral cylinder spacing if the cylinder has to stretch or shrink its dimension perpendicular to the plane of the film, respectively. The SST calculations overestimate this effect due to the highly exaggerated influence of the interface between the blocks in the SST treatment. The effect diminishes at weaker segregation, since interfacial effects become less important in this regime. The optimal spacing of the C_{\parallel} structure increases with the numbers of cylinder layers and approaches the bulk value for thick films as predicted by the SST theory.

Finally the first *in-situ* observation of phase transitions in thin block copolymer films is presented. During annealing with a controlled atmosphere of chloroform vapor the film develops islands and holes. The development of the microdomain structure and its spacial fluctuations are captured. The rather high polymer concentration in the thin film results in a time scale of the fluctuations in the order of seconds to minutes. The decreasing film thickness inside of the holes triggers phase transitions from C_{\perp} to C_{\parallel} to PL according to the phase diagram of the system. We find that the grains of new phases nucleate preferably at defect sites decorating the grain boundaries of more than two grains of the original phase and then grow along the grain boundaries. For both transitions the original and the new structure are not commensurable, which induces reorientation processes in the new phases. The grain size in the new phase is dependent on the symmetry of the phase and therefore smallest for the C_{\parallel} phase. The grains of the C_{\parallel} phase heal more efficiently close to the phase boundary to the PL phase, since defects are replaced by threefold interconnections of the cylinders, which may be considered as elementary units of the PL phase. We attribute this effect to an enhanced diffusion of molecules along these interconnections. The same effect

8 Summary / Zusammenfassung

enhances the healing of the PL structure since this phase is continuous within the plane of the film both in the polystyrene-rich phase and the polybutadiene-rich phase.

The healing of the PL phase is mediated by the movement and annihilation of dislocations. The most common process is the dislocation glide. Dislocation climbs are rare and take place by the formation or annihilation of lattice sites and are always accompanied by the annihilation or creation of two half rows of material, respectively. This process effectively annihilates two dislocations of different orientation and creates a new dislocation with intermediate orientation conserving the Burgers vector. This process therefore efficiently complements the annihilation of antiparallel dislocations.

Zusammenfassung

Im Rahmen dieser Arbeit wurde Gleichgewichts- und dynamisches Phasenverhalten von Blockcopolymeren mit zylindrischer Mikrodomänenstruktur in dünnen Filmen untersucht. Die Resultate reichen von einer Erweiterung einer fortschrittlichen Theorie starker Segregation auf die Behandlung von zylinderförmigen Mikrodomänen in einem dünnen Film über das Studium des Phasenverhaltens und des Mikrodomänenabstands eines Modellsystems mit zylinderförmigen Mikrodomänen bis hin zu den ersten *in-situ* Messungen von Phasenübergängen und Mikrodomänendynamik in einem dünnen Blockcopolymerfilm.

Das erste Resultat betrifft die Dünnschichtcharakterisierung unseres Modellsystems, ein Polystyrol-*block*-polybutadien-*block*-polystyrol (SBS) Dreiblockcopolymer, mit Hilfe der "tapping mode"-Rasterkraftmikroskopie (TM-RKM). Ein Verfahren wird präsentiert, mit dessen Hilfe man zuverlässig die wahre Oberflächentopographie von weichen, polymeren Proben bestimmen kann. Die Messung eines Arrays von Amplitude-Phase-Distanz (APD) Kurven ermöglicht es, quantitativ zwischen der "wahren" Oberflächentopographie und lateralen Unterschieden der Eindringtiefe der Spitze zu unterscheiden. Es stellt sich heraus, dass die konventionellen Höhenbilder einer TM-RKM Messung nicht notwendigerweise die Oberflächentopographie wiedergeben. Im Falle der SBS-Proben ermitteln wir eine flache Beschaffenheit der Oberfläche und stellen fest, dass das konventionelle Höhenbild nur die lateralen Unterschiede der Eindringtiefe der Spitze widerspiegelt. Änderungen im Höhen- und Phasenkontrast können auf eine Überschneidung von unterschiedlichen Bereichen zurückgeführt werden, in denen entweder anziehende oder abstoßende Kräfte überwiegen. Schließlich ermöglicht uns eine lateral aufgelöste Bestimmung der Eindringtiefe die Dicke einer weichen, oberflächennahen Schicht über solch winzigen Strukturen wie den Blockcopolymermikrodomänen zu bestimmen.

Es wurde eine theoretische Behandlung des Dünnschichtphasenverhaltens von

8 Summary / Zusammenfassung

Blockcopolymeren mit zylinderförmiger Mikrodomänenstruktur im Rahmen einer fortschrittlichen Theorie starker Segregation (strong segregation theory: SST) von Olmsted und Milner [Olm94] entwickelt. Obwohl die Theorie im strengen Sinne nur für stark gestreckte Ketten gültig ist und nur zylinderförmige Mikrodomänenstrukturen behandelt werden, stehen die Ergebnisse in gutem Einklang mit den experimentellen Ergebnissen dieser Arbeit. Die betrachteten Mikrodomänenstrukturen sind senkrecht zur Filmebene orientierte Zylinder C_{\perp} und Zylinder, die in der Filmebene orientiert sind und entweder mit der Matrixkomponente C_{\parallel} oder einem halben Zylinder $C^{1/2}$ an den Oberflächen terminieren. Die theoretische Abhandlung beinhaltet die Berechnung der freien Energie pro Molekül und pro Fläche von verzerrten Einheitszellen von hexagonal geordneten Zylindern. Die planare Natur der Filmoberflächen bedingt eine solche Verzerrung in der C_{\parallel} Phase, die in einer Zunahme der freien Energie und in einem vom Volumen unterschiedlichen Mikrodomänenabstandes resultiert. Eine direkte Folge ist eine Erweiterung des Stabilitätsbereiches der C_{\perp} Phase bei einer schwachen Anziehung der Majoritätsphase zu den Oberflächen. Die Stabilität dieser Struktur ist auch erhöht, wenn die Filmdicke nicht kommensurabel zum bevorzugten Zylinderlagenabstand der C_{\parallel} und der $C^{1/2}$ Phase ist. Halbe Zylinder an der Oberfläche werden durch eine präferentielle Anziehung der Minoritätsphase zur Oberfläche stabilisiert.

Das Dünnschicht-Phasenverhalten von konzentrierten SBS-Lösungen wurde studiert. Die stabilen Phasen werden als Funktion der Filmdicke und der Polymerkonzentration ϕ_P aufgetragen. Die Variation von ϕ_P kann als eine Variation der effektiven molekularen Wechselwirkungen zwischen den beiden Polymerkomponenten und zwischen den Komponenten und den Oberflächen interpretiert werden. Die bevorzugte Anziehung der Matrixkomponente zu den Oberflächen, das Oberflächenfeld, verursacht eine Anordnung der Zylinder parallel zur Filmebene immer dann, wenn die Filmdicke zu einem ganzzahligen Vielfachen von Zylinderlagen passt. Bei dazwischen liegenden Filmdicken richten sich die Zylinder senkrecht zur Filmebene aus. Bei höheren Polymerkonzentrationen, also bei höheren Oberflächenfeldern, wird eine perforierte Lamelle (PL) von Polystyrol gebildet. Dies bestätigt Ergebnisse aus Simulationen, die eine Abklinglänge des Oberflächenfeldes von etwa einem Mikrodomänenabstand anzeigen [Hui01, Hui00, Kno02, Hor02]. Eine Lage Polymer existiert unter allen Filmen

und besteht entweder aus gepinnten Molekülen oder einer halben Lamelle.

Die experimentellen Ergebnisse stimmen hervorragend sowohl mit den in dieser Arbeit aufgezeigten Ergebnissen aus der Theorie starker Segregation als auch mit Computersimulationen, die auf einer dynamischen Dichtefunktionaltheorie basieren [Kno02, Hor02], überein. Eine Ausnahme ist, dass die SST keine Aussagen über die PL-Phase treffen kann, da diese Phase nicht von der Theorie berücksichtigt wird.

Weiterhin wurden die bestimmenden Mikrodomänenabstände in den dünnen Filmen im Detail untersucht und mit den Vorhersagen der SST- Theorie verglichen. Ein neuer Bildverarbeitungsalgorithmus wurde entwickelt, der aus den RKM-Phasenbildern die unterschiedlichen Strukturen erkennt und lokalisiert. Die Mikrodomänenabstände werden als Funktion verschiedener Parameter wie der Filmdicke, der Polymerkonzentration und der lokalen Krümmung der Mikrodomänenstruktur diskutiert. Eine Untersuchung der Abstände der C_{\parallel} Struktur von der lokalen Krümmung der Zylinder ergibt einen Effekt zweiter Ordnung, der durch die Dichteerhaltung der polymeren Blöcke erklärt werden kann.

Die Zylinderabstände in der C_{\parallel} Struktur hängen außerdem von der lokalen Filmdicke ab. Die C_{\parallel} Phase ist in einem Bereich von Filmdicken stabil, der nicht zu weit von der optimalen Filmdicke dieser Struktur abweicht. Innerhalb dieses Bereiches muss sich die Zylinderdicke der Filmdicke anpassen. Je nachdem, ob die Zylinder senkrecht zur Filmebene gestreckt oder gestaucht werden, führt die Minimierung der Interface-Fläche zwischen den beiden Blöcken zu einem kleineren oder größeren lateralen Zylinderabstand. Die SST-Rechnungen überschätzen diesen Effekt, da der Einfluss des Interfaces zwischen den Blöcken in den Rechnungen stark übertrieben ist. Experimentell verschwindet der Effekt bei niedrigen Konzentrationen, da der Einfluss des Interfaces in schwächer segregierten Systemen nachlässt. Wie von der Theorie vorhergesagt, nimmt der optimale laterale Mikrodomänenabstand der C_{\parallel} Struktur mit zunehmender Anzahl von Zylinderlagen zu und nähert sich dem Wert des Abstandes im Volumen.

Schließlich werden die ersten in-situ Messungen von Phasenübergängen in dünnen Blockcopolymerfilmen beschrieben. Während der Präparation in einer Atmosphäre mit kontrolliertem Chloroformdampfdruck bilden sich Löcher und Inseln im Film. Sowohl die Entwicklung der Mikrodomänenstruktur als auch die räumlichen Fluktuationen konnten aufgezeichnet werden. Die eher hohe Polymerkon-

8 Summary / Zusammenfassung

zentration im dünnen Film bedingt eine Zeitskala der Fluktuationen im Bereich von Sekunden bis Minuten. Die abnehmende Filmdicke innerhalb der Löcher triggert Phasenübergänge von C_{\perp} zu C_{\parallel} und schließlich zu PL, wie sie vom Phasendiagramm des Systems vorhergesagt werden. Außerdem stellt man fest, dass sich neue Phasen bevorzugt an den Defekten, die die Korngrenzen von mehr als zwei Körnern dekorieren, bilden und dann entlang der Korngrenzen wachsen. In beiden Fällen gilt, dass die Strukturen der ursprünglichen und der neuen Phase nicht kommensurabel zueinander sind, was durch einen Reorientierungsprozess in der neuen Phase ausgeglichen wird. Die Korngröße ist am kleinsten in der C_{\parallel} Phase, da diese Phase die niedrigste Symmetrie besitzt. Die Körner dieser C_{\parallel} Phase heilen am besten in der Nähe des Phasenübergangs zur PL Phase, da dort die typischen Defekte durch eine dreiarmlige Zwischenverbindung ersetzt werden, die als Elementarzelle der PL Phase betrachtet werden kann. Diese Strukturen scheinen die Diffusion der Moleküle entlang der Zwischenverbindungen und damit zwischen den Zylindern zu erhöhen. Der selbe Effekt beschleunigt das Ausheilen der PL Struktur, da diese Struktur innerhalb der Filmebene sowohl in der polystyrolreichen als auch in der polybutadienreichen Mikrophase kontinuierlich ist.

Das Ausheilen der PL-Phase findet durch die Bewegung und die Auslöschung von Versetzungen statt. Der häufigste Prozess ist hierbei das Gleiten von Versetzungen (glide), wohingegen das Steigen (climb) von Versetzungen sehr selten ist und durch das Entstehen oder die Zerstörung einer Gitterstelle geschieht. Dieser Prozess ist außerdem immer mit der Auslöschung oder der Entstehung zweier Materialhalbzeilen gekoppelt. Dabei geschieht diese Auslöschung durch einen Prozess, in dem zwei Versetzungen mit unterschiedlicher Orientierung durch eine Versetzung mit mittlerer Orientierung ersetzt werden. Dabei bleibt der Burger's-Vektor erhalten. Dieser Prozess macht damit eine effektive Rotation einer Versetzung möglich und ergänzt effizient die Auslöschung zweier antiparalleler Versetzungen.

9 Bibliography

- [Ada94] J. L. Adams, W. W. Graessley, and R. A. Register. *Macromolecules*, **27**(21), 6026 (1994)
- [Ada98] J. L. Adams, D. J. Quiram, W. W. Graessley, R. A. Register, and G. R. Marchand. *Macromolecules*, **31**(1), 201 (1998)
- [Alm90] K. Almdal, J. H. Rosedale, F. S. Bates, G. D. Wignall, and G. H. Fredrickson. *Phys. Rev. Lett.*, **65**(9), 1112 (1990)
- [Amu92] K. Amundson, E. Helfand, S. S. Patel, X. Quan, and S. D. Smith. *Macromolecules*, **25**(7), 1935 (1992)
- [Amu93] K. Amundson, E. Helfand, X. Quan, and S. D. Smith. *Macromolecules*, **26**(11), 2698 (1993)
- [Amu94] K. Amundson, E. Helfand, X. Quan, S. D. Hudson, and S. D. Smith. *Macromolecules*, **27**(22), 6559 (1994)
- [Ana89] S. H. Anastasiadis, T. P. Russell, S. K. Satija, and C. F. Majkrzak. *Phys. Rev. Lett.*, **62**, 1852 (1989)
- [Bar00] G. Bar, R. Brandsch, M. Bruch, L. Delineau, and M. H. Whangbo. *Surf. Sci.*, **444**(1-3), L11 (2000)
- [Bat90] F. S. Bates and G. H. Fredrickson. *Annu. Rev. Phys. Chem.*, **41**, 525 (1990)
- [Bat94] F. S. Bates and G. H. Fredrickson. *Macromolecules*, **27**(4), 1065 (1994)
- [Bat99] F. S. Bates and G. H. Fredrickson. *Physics Today*, **52**(2), 32 (1999)
- [Beh99] O. P. Behrend, L. Odoni, J. L. Loubet, and N. A. Burnham. *Appl. Phys. Lett.*, **75**(17), 2552 (1999)

9 Bibliography

- [Bin86] G. Binnig, C. F. Quate, and C. Gerber. *Phys. Rev. Lett.*, **56**(9), 930 (1986)
- [Bin99] K. Binder. *Adv. Polym. Sci.*, **138**(Polymers in Confined Environments), 1 (1999)
- [Bin00] K. Binder and M. Muller. *Curr. Opin. Colloid Interface Sci.*, **5**(5,6), 315 (2000)
- [Bla01] C. T. Black, K. W. Guarini, K. R. Milkove, S. M. Baker, T. P. Russell, and M. T. Tuominen. *Appl. Phys. Lett.*, **79**(3), 409 (2001)
- [Boe02] A. Boeker. *Self-Assembly of Block Copolymers in External Fields*. Ph.D. thesis, Universität Bayreuth (2002)
- [Boe02a] A. Boeker, H. Elbs, H. Hänsel, A. Knoll, S. Ludwigs, H. Zettl, V. Urban, V. Abetz, A. H. E. Mueller, and G. Krausch. *Phys. Rev. Lett.*, **89**(13), 135502 (2002)
- [Boe02b] A. Boeker, A. Knoll, H. Elbs, V. Abetz, A. H. E. Mueller, and G. Krausch. *Macromolecules*, **35**(4), 1319 (2002)
- [Boi98] R. Boisgard, D. Michel, and J. Aime'. *Surf. Sci.*, **401**, 199 (1998)
- [Bra89] J. Brandrup and E. H. Immergut. *Polymer Handbook*. Wiley, New York (1989)
- [Bro94] G. Brown and A. Chakrabarti. *J. Chem. Phys.*, **101**(4), 3310 (1994)
- [BW91] F. Brochard-Wyart, J. M. Di Meglio, D. Quere, and P. G. De Gennes. *Langmuir*, **7**(2), 335 (1991)
- [CC99] Corel-Corporation. "Corel Photo Paint" (1998-1999)
- [Cha00] C. Chaibundit, W. Mingvanish, S. C. Turner, S.-M. Mai, J. P. A. Fairclough, A. J. Ryan, M. W. Matsen, and C. Booth. *Macromolecular Rapid Communications*, **21**(14), 964 (2000)
- [Che98] X. Chen, M. Davies, C. Roberts, S. Tendler, P. Williams, J. Davies, A. Dawkes, and J. Edwards. *Ultramicroscopy*, **75**, 171 (1998)

9 Bibliography

- [Che01] J. Y. Cheng, C. A. Ross, V. Z. H. Chan, E. L. Thomas, R. G. H. Lammertink, and G. J. Vancso. *Adv. Mater.*, **13**(15), 1174 (2001)
- [Cle98] J. P. Cleveland, B. Anczykowski, A. E. Schmid, and V. B. Elings. *Appl. Phys. Lett.*, **72**(20), 2613 (1998)
- [Cou89] G. Coulon, T. P. Russell, V. R. Deline, and P. F. Green. *Macromolecules*, **22**(6), 2581 (1989)
- [Dai96] H. J. Dai, N. P. Balsara, B. A. Garetz, and M. C. Newstein. *Phys. Rev. Lett.*, **77**(17), 3677 (1996)
- [Del00] L. Delineau, R. Brandsch, G. Bar, and M. H. Whangbo. *Surf. Sci.*, **448**(1), L179 (2000)
- [Dor99] I. Dorofeyev, H. Fuchs, G. Wenning, and B. Gotsmann. *Phys. Rev. Lett.*, **83**(12), 2402 (1999)
- [Elb01] H. Elbs. *Mikrophasenseparation von ABC-Dreiblockcopolymeren in dünnen Filmen*. Ph.D. thesis, University of Bayreuth (2001)
- [Fas00] M. J. Fasolka, P. Banerjee, A. M. Mayes, G. Pickett, and A. C. Balazs. *Macromolecules*, **33**(15), 5702 (2000)
- [Fas01] M. J. Fasolka and A. M. Mayes. *Annu. Rev. Mat. Res.*, **31**, 323 (2001)
- [Fen02] J. Feng, H. Liu, and Y. Hu. *Macromolecular Theory and Simulations*, **11**(5), 556 (2002)
- [Fen02a] J. Feng and E. Ruckenstein. *Polymer*, **43**(21), 5775 (2002)
- [Fen02b] J. Feng and E. Ruckenstein. *Macromolecular Theory and Simulations*, **11**(6), 630 (2002)
- [Flo89] P. J. Flory. *Principles of Polymer Chemistry*. Cornell University Press, third edition edition (1989)
- [Foe94] S. Foerster, A. K. Khandpur, J. Zhao, F. S. Bates, I. W. Hamley, A. J. Ryan, and W. Bras. *Macromolecules*, **27**(23), 6922 (1994)

9 Bibliography

- [Fos92] M. D. Foster, M. Sikka, N. Singh, F. S. Bates, S. K. Satija, and C. F. Majkrzak. *J. Chem. Phys.*, **96**(11), 8605 (1992)
- [Fre87] G. H. Fredrickson. *Macromolecules*, **20**, 2535 (1987)
- [Fre87a] G. H. Fredrickson and E. Helfand. *J. Chem. Phys.*, **87**(1), 697 (1987)
- [Fre89] G. H. Fredrickson and L. Leibler. *Macromolecules*, **22**(3), 1238 (1989)
- [Fri91] H. Fried and K. Binder. *J. Chem. Phys.*, **94**(12, Pt. 2), 8349 (1991)
- [Fri02] A. L. Frischknecht, J. G. Curro, and L. J. Douglas Frink. *J. Chem. Phys.*, **117**(22), 10398 (2002)
- [Fuk03] K. Fukunaga, T. Hashimoto, H. Elbs, and G. Krausch. *Macromolecules*, **36**(8), 2852 (2003)
- [Gad99] N. Gadegaard, K. Almdal, N. B. Larsen, and K. Mortensen. *Appl. Surf. Sci.*, **142**(1-4), 608 (1999)
- [Gar98] R. García, J. Tamayo, M. Calleja, and F. García. *Appl. Phys. A*, **66**, S309 (1998)
- [Geh92] M. D. Gehlsen, K. Almdal, and F. S. Bates. *Macromolecules*, **25**(2), 939 (1992)
- [Gua02] K. W. Guarini, C. T. Black, and S. H. I. Yeung. *Adv. Mater.*, **14**(18), 1290 (2002)
- [Hah98] J. Hahm, W. A. Lopes, H. M. Jaeger, and S. J. Sibener. *J. Chem. Phys.*, **109**(23), 10111 (1998)
- [Haj97] D. A. Hajduk, H. Takenouchi, M. A. Hillmyer, F. S. Bates, M. E. Vigild, and K. Almdal. *Macromolecules*, **30**, 3788 (1997)
- [Ham98] J. W. Hamley. *The Physics of Block Copolymers*. Oxford University Press, Oxford (1998)
- [Han98] K. J. Hanley and T. P. Lodge. *J. Polym. Sci., Part B: Polym. Phys.*, **36**(17), 3101 (1998)

9 Bibliography

- [Han00] K. J. Hanley, T. P. Lodge, and C.-I. Huang. *Macromolecules*, **33**(16), 5918 (2000)
- [Har98] C. Harrison, M. Park, P. Chaikin, R. Register, D. Adamson, and N. Yao. *Macromolecules*, **31**(7), 2185 (1998)
- [Har98a] C. Harrison, M. Park, P. M. Chaikin, R. A. Register, D. H. Adamson, and N. Yao. *Polymer*, **39**(13), 2733 (1998)
- [Har99] C. Harrison. *Block Copolymer Microdomains in Thin Films*. Ph.D. thesis, Princeton University (1999)
- [Har00] C. Harrison, D. H. Adamson, Z. Cheng, J. M. Sebastian, S. Sethuraman, D. A. Huse, R. A. Register, and P. M. Chaikin. *Science*, **290**(5496), 1558 (2000)
- [Har02] C. Harrison, Z. Cheng, S. Sethuraman, D. A. Huse, P. M. Chaikin, D. A. Vega, J. M. Sebastian, R. A. Register, and D. H. Adamson. *Phys. Rev. E*, **66**(1-1), 011706/1 (2002)
- [Has83] T. Hashimoto, M. Shibayama, and H. Kawai. *Macromolecules*, **16**(7), 1093 (1983)
- [Has90] T. Hashimoto, H. Tanaka, and H. Hasegawa. *Macromolecules*, **23**(20), 4378 (1990)
- [Has95] T. Hashimoto and N. Sakamoto. *Macromolecules*, **28**(13), 4779 (1995)
- [Has98] T. Hashimoto, T. Ogawa, N. Sakamoto, M. Ichimiya, J. K. Kim, and C. D. Han. *Polymer*, **39**(8-9), 1573 (1998)
- [Hei99] J. Heier, J. Genzer, E. J. Kramer, F. S. Bates, S. Walheim, and G. Krausch. *J. Chem. Phys.*, **111**(24), 11101 (1999)
- [Hel72] E. Helfand and Y. Tagami. *J. Chem. Phys.*, **56**(7), 3592 (1972)
- [Hel76] E. Helfand and Z. R. Wasserman. *Macromolecules*, **9**(6), 879 (1976)
- [Hel78] E. Helfand and Z. R. Wasserman. *Macromolecules*, **11**(5), 960 (1978)
- [Hel80] E. Helfand and Z. R. Wasserman. *Macromolecules*, **13**(4), 994 (1980)

9 Bibliography

- [Hew86] M. Hewel and W. Ruland. *Makromolekulare Chemie, Macromolecular Symposia*, **4**, 197 (1986)
- [Hom03] Homepage. “The movies can be found on the homepage of our department: <http://www.uni-bayreuth.de/departments/pcii>”. Technical report (2003)
- [Hon83] K. M. Hong and J. Noolandi. *Macromolecules*, **16**(7), 1083 (1983)
- [Hor02] A. Horvat, K. S. Lyakhova, G. J. A. Sevink, A. V. Zvelindovsky, and R. Magerle. *J. Chem. Phys.*, **submitted** (2002)
- [Höp95] R. Höper, T. Gesang, W. Possart, O. D. Hennemann, and S. Boseck. *Ultramicroscopy*, **60**(1), 17 (1995)
- [Hua98] C.-I. Huang and T. P. Lodge. *Macromolecules*, **31**(11), 3556 (1998)
- [Hui00] H. P. Huinink, J. C. M. Brokken-Zijp, M. A. van Dijk, and G. J. A. Sevink. *J. Chem. Phys.*, **112**(5), 2452 (2000)
- [Hui01] H. P. Huinink, M. A. van Dijk, J. C. M. Brokken-Zijp, and G. J. A. Sevink. *Macromolecules*, **34**(15), 5325 (2001)
- [Jeo02] U. Jeong, H.-C. Kim, R. L. Rodriguez, I. Y. Tsai, C. M. Stafford, J. K. Kim, C. J. Hawker, and T. P. Russell. *Adv. Mater.*, **14**(4), 274 (2002)
- [Jeo03] U. Jeong, H. H. Lee, H. Yang, J. K. Kim, S. Okamoto, S. Aida, and S. Sakurai. *Macromolecules*, **36**(5), 1685 (2003)
- [Kar93] A. Karim, N. Singh, M. Sikka, F. S. Bates, W. D. Dozier, and G. P. Felcher. *J. Chem. Phys.*, **100**(2), 1620 (1993)
- [Kel96] G. J. Kellogg, D. G. Walton, A. M. Mayes, P. Lambooy, T. P. Russell, P. D. Gallagher, and S. K. Satija. *Phys. Rev. Lett.*, **76**(14), 2503 (1996)
- [Küh98] A. Kühle, A. Sørensen, J. Zandbergen, and J. Bohr. *Appl. Phys. A*, **66**, S329 (1998)
- [Kha95] A. K. Khandpur, S. Foerster, F. S. Bates, I. W. Hamley, A. J. Ryan, W. Bras, K. Almdal, and K. Mortensen. *Macromolecules*, **28**(26), 8796 (1995)

9 Bibliography

- [Kim98] G. Kim and M. Libera. *Macromolecules*, **31**, 2670 (1998)
- [Kim98a] G. Kim and M. Libera. *Macromolecules*, **31**, 2569 (1998)
- [Kim98b] J. K. Kim, H. H. Lee, Q.-J. Gu, T. Chang, and Y. H. Jeong. *Macromolecules*, **31**(12), 4045 (1998)
- [Kim01] H.-C. Kim and T. P. Russell. *J. Polym. Sci., Part B: Polym. Phys.*, **39**(6), 663 (2001)
- [Kim01a] W. G. Kim, B. A. Garetz, M. C. Newstein, and N. P. Balsara. *J. Polym. Sci., Part B: Polym. Phys.*, **39**(19), 2231 (2001)
- [Kno01] A. Knoll, R. Magerle, and G. Krausch. *Macromolecules*, **34**(12), 4159 (2001)
- [Kno02] A. Knoll, A. Horvat, K. S. Lyakhova, G. Krausch, G. J. A. Sevink, A. V. Zvelindovsky, and R. Magerle. *Phys. Rev. Lett.*, **89**(3), 035501/1 (2002)
- [Kno03] A. Knoll. “CD submitted with thesis” (2003)
- [Kob90] J. T. Koberstein, T. P. Russell, D. J. Walsh, and L. Pottick. *Macromolecules*, **23**(3), 877 (1990)
- [Kon96] N. Koneripalli, R. Levicky, F. S. Bates, J. Ankner, H. Kaiser, and S. K. Satija. *Langmuir*, **12**(26), 6681 (1996)
- [Kon00] M. Konrad, A. Knoll, G. Krausch, and R. Magerle. *Macromolecules*, **33**(15), 5518 (2000)
- [Lam94] P. Lambooy, T. P. Russell, G. J. Kellogg, A. M. Mayers, P. D. Gallagher, and S. K. Satija. *Phys. Rev. Lett.*, **72**(18), 2899 (1994)
- [Lee03] A. Lee. “VirtualDub 1.5.1 (build 15645/release)” (1998-2003)
- [Lee03a] A. Lee. “private communication” (2003)
- [Lei80] L. Leibler. *Macromolecules*, **13**(6), 1602 (1980)

9 Bibliography

- [Li00] R. R. Li, P. D. Dapkus, M. E. Thompson, W. G. Jeong, C. Harrison, P. M. Chaikin, R. A. Register, and D. H. Adamson. *Appl. Phys. Lett.*, **76**(13), 1689 (2000)
- [Lin02] Z. Lin, D. H. Kim, X. Wu, L. Boosahda, D. Stone, L. LaRose, and T. P. Russell. *Adv. Mater.*, **14**(19), 1373 (2002)
- [Lip03] U. Lippert. “Mikrophasenseparation von AB und ABA Blockcopolymeren”. Technical report, PC II, Universität Bayreuth (2003)
- [Lod95] T. P. Lodge, C. Pan, X. Jin, Z. Liu, J. Zhao, W. W. Maurer, and F. S. Bates. *J. Polym. Sci., Part B: Polym. Phys.*, **33**(16), 2289 (1995)
- [Lod03] T. P. Lodge. *Macromol. Chem. Phys.*, **204**(2), 265 (2003)
- [Lod03a] T. P. Lodge, K. J. Hanley, B. Pudil, and V. Alahapperuma. *Macromolecules*, **36**(3), 816 (2003)
- [Lun98] M. Luna, J. Colchero, and A. M. Baró. *Appl. Phys. Lett.*, **72**(26), 3461 (1998)
- [Lya03] K. S. Lyakhova, A. Horvat, R. Magerle, G. J. A. Sevink, and A. V. Zvelindovsky (2003)
- [Mag97] S. N. Magonov, J. Cleveland, V. Elings, D. Denley, and M.-H. Whangbo. *Surf. Sci.*, **389**(1-3), 201 (1997)
- [Mag00] R. Magerle. *Phys. Rev. Lett.*, **85**(13), 2749 (2000)
- [Mai00] S.-M. Mai, W. Mingvanish, S. C. Turner, C. Chaibundit, J. P. A. Fairclough, F. Heatley, M. W. Matsen, A. J. Ryan, and C. Booth. *Macromolecules*, **33**(14), 5124 (2000)
- [Mar96] A. H. Marcus and S. A. Rice. *Phys. Rev. Lett.*, **77**(12), 2577 (1996)
- [Mar97] A. H. Marcus and S. A. Rice. *Phys. Rev. E*, **55**(1-B), 637 (1997)
- [Mat94] M. W. Matsen and M. Schick. *Macromolecules*, **27**(1), 187 (1994)
- [Mat94a] M. W. Matsen and M. Schick. *Phys. Rev. Lett.*, **72**(16), 2660 (1994)

9 Bibliography

- [Mat95] M. W. Matsen. *J. Chem. Phys.*, **102**(9), 3884 (1995)
- [Mat97] M. W. Matsen and F. S. Bates. *J. Chem. Phys.*, **106**(6), 2436 (1997)
- [Mat97a] M. W. Matsen and F. S. Bates. *J. Polym. Sci., Part B: Polym. Phys.*, **35**(6), 945 (1997)
- [Mat98] M. Matsen. *Curr. Opin. Colloid Interface Sci.*, **3**, 40 (1998)
- [Mat99] M. W. Matsen and R. B. Thompson. *J. Chem. Phys.*, **111**(15), 7139 (1999)
- [Mat00] M. W. Matsen. *J. Chem. Phys.*, **113**(13), 5539 (2000)
- [Mat03] M. W. Matsen. *Phys. Rev. E*, **67**(2-1), 023801/1 (2003)
- [Mau98] W. W. Maurer, F. S. Bates, T. P. Lodge, K. Almdal, K. Mortensen, and G. H. Fredrickson. *J. Chem. Phys.*, **108**(7), 2989 (1998)
- [May89] A. M. Mayes and M. Olvera de la Cruz. *J. Chem. Phys.*, **91**(11), 7228 (1989)
- [May91] A. M. Mayes and M. Olvera de la Cruz. *J. Chem. Phys.*, **95**(6), 4670 (1991)
- [Mor96] K. Mori, A. Okawara, and T. Hashimoto. *J. Chem. Phys.*, **104**(19), 7765 (1996)
- [Mor96a] T. L. Morkved, M. Lu, A. M. Urbas, E. E. Ehrichs, H. M. Jaeger, P. Mansky, and T. P. Russell. *Science*, **273**(5277), 931 (1996)
- [Mor97] T. L. Morkved, W. A. Lopes, M. Lu, A. M. Urbas, H. M. Jaeger, P. Mansky, and T. P. Russell. *Materials Research Society Symposium Proceedings*, **461**(Morphological Control in Multiphase Polymer Mixtures), 109 (1997)
- [Mor01] K. Mori, H. Hasegawa, and T. Hashimoto. *Polymer*, **42**(7), 3009 (2001)
- [Nak96] A. I. Nakatani, F. A. Morrison, J. F. Douglas, J. W. Mays, C. L. Jackson, M. Muthukumar, and C. C. Han. *J. Chem. Phys.*, **104**(4), 1589 (1996)

9 Bibliography

- [New98] M. C. Newstein, B. A. Garetz, N. P. Balsara, M. Y. Chang, and H. J. Dai. *Macromolecules*, **31**(1), 64 (1998)
- [NI00] National-Instruments. “Labview 6.02” (2000)
- [Non99] L. Nony, R. Boisgard, and J. P. Aime´. *J. Chem. Phys.*, **111**(4), 1615 (1999)
- [Oht86] T. Ohta and K. Kawasaki. *Macromolecules*, **19**(10), 2621 (1986)
- [Olm94] P. D. Olmsted and S. T. Milner. *Phys. Rev. Lett.*, **72**(6), 936 (1994)
- [Olm95] P. D. Olmsted and S. T. Milner. *Phys. Rev. Lett.*, **74**(5), 829 (1995)
- [Olm98] P. D. Olmsted and S. T. Milner. *Macromolecules*, **31**(12), 4011 (1998)
- [Owe89] J. N. Owens, I. S. Gancarz, J. T. Koberstein, and T. P. Russell. *Macromolecules*, **22**(8), 3380 (1989)
- [Par97] M. Park, C. Harrison, P. M. Chaikin, R. A. Register, and D. H. Adamson. *Science*, **276**(5317), 1401 (1997)
- [Par01] M. Park, P. M. Chaikin, R. A. Register, and D. H. Adamson. *Appl. Phys. Lett.*, **79**(2), 257 (2001)
- [Per01] G. G. Pereira. *Phys. Rev. E*, **63**(6 Pt 1), 061809. FIELD Reference Number: FIELD Journal Code:101136452 FIELD Call Number: (2001)
- [Per03] G. G. Pereira. *Phys. Rev. E*, **67**(2-1), 023802/1 (2003)
- [Pic98] J. P. Pickering and G. J. Vansco. *Polym. Bull.*, **40**, 549 (1998)
- [PT02] POV-Team. “Pov-Ray 3.5” (1991-2002)
- [Qi97] S. Qi and Z.-G. Wang. *Phys. Rev. E*, **55**(2), 1682 (1997)
- [Qui94] A. P. Quist, J. Ahlbom, C. T. Reimann, and B. U. R. Sundqvist. *Nucl. Instrum. Methods Phys. Res., Sect. B*, **88**, 164 (1994)
- [Rad96] L. Radzilowski, B. Carvalho, and E. Thomas. *J. Polym. Sci., Part B: Polym. Phys.*, **34**, 3081 (1996)

9 Bibliography

- [Reh01] N. Rehse, A. Knoll, R. Magerle, and G. Krausch. *Abstr. Pap. - Am. Chem. Soc.*, **221st**, PMSE (2001)
- [Reh03] N. Rehse, A. Knoll, R. Magerle, and G. Krausch. *Macromolecules*, **36**(9), 3261 (2003)
- [Rii95] B. L. Riise, G. H. Fredrickson, R. G. Larson, and D. S. Pearson. *Macromolecules*, **28**(23), 7653 (1995)
- [Ros95] J. H. Rosedale, F. S. Bates, K. Almdal, K. Mortensen, and G. D. Wignall. *Macromolecules*, **28**(5), 1429 (1995)
- [Rus89] T. P. Russell, G. Coulon, V. R. Deline, and D. C. Miller. *Macromolecules*, **22**(12), 4600 (1989)
- [Ryu97] C. Y. Ryu, M. S. Lee, D. A. Haiduk, and T. P. Lodge. *J. Polym. Sci., Part B: Polym. Phys.*, **35**(17), 2811 (1997)
- [Sag93] C. Sagui and R. C. Desai. *Phys. Rev. Lett.*, **71**(24), 3995 (1993)
- [Sak92] S. Sakurai, K. Mori, A. Okawara, K. Kimishima, and T. Hashimoto. *Macromolecules*, **25**(10), 2679 (1992)
- [Sak93] S. Sakurai, T. Momii, K. Taie, M. Shibayama, S. Nomura, and T. Hashimoto. *Macromolecules*, **26**(3), 485 (1993)
- [Sak96] S. Sakurai, T. Hashimoto, and L. J. Fetters. *Macromolecules*, **29**(2), 740 (1996)
- [See01] R. Seemann, S. Herminghaus, and K. Jacobs. *Phys. Rev. Lett.*, **86**(24), 5534 (2001)
- [See01a] R. Seemann, S. Herminghaus, and K. Jacobs. *J. Phys. Condens. Matter*, **13**(21), 4925 (2001)
- [Seg01] R. A. Segalman, H. Yokoyama, and E. J. Kramer. *Adv. Mater.*, **13**(15), 1152 (2001)
- [Seg03] R. A. Segalman, A. Hexemer, R. C. Hayward, and E. J. Kramer. *Macromolecules*, p. ACS ASAP (2003)

9 Bibliography

- [Sem85] A. N. Semenov. *Sov. Phys. JETP*, **61**, 733 (1985)
- [Seu95] M. Seul and D. Andelman. *Science*, **267**(5197), 476 (1995)
- [Sev99] G. J. A. Sevink, A. V. Zvelindovsky, B. A. C. van Vlimmeren, N. M. Maurits, and J. G. E. M. Fraaije. *J. Chem. Phys.*, **110**(4), 2250 (1999)
- [Sev02] G. J. A. Sevink, J. G. E. M. Fraaije, and H. P. Huinink. *Macromolecules*, **35**(5), 1848 (2002)
- [Shi83] M. Shibayama, T. Hashimoto, H. Hasegawa, and H. Kawai. *Macromolecules*, **16**(9), 1427 (1983)
- [Shu91] K. R. Shull, E. J. Kramer, F. S. Bates, and J. H. Rosedale. *Macromolecules*, **24**(6), 1383 (1991)
- [Shu92] K. R. Shull. *Macromolecules*, **25**(8), 2122 (1992)
- [Sik93] M. Sikka, N. Singh, A. Karim, and F. S. Bates. *Phys. Rev. Lett.*, **70**(3), 307 (1993)
- [Spa97] J. P. Spatz, S. Sheiko, M. Möller, R. G. Winkler, P. Reineker, and O. Marti. *Langmuir*, **13**, 4699 (1997)
- [Sto96] W. Stocker, J. Beckmann, R. Stadler, and J. P. Rabe. *Macromolecules*, **29**, 7502 (1996)
- [Str96] G. Strobl. *The Physics of Polymers*. Springer-Verlag Berlin Heidelberg (1996)
- [Suh98] K. Y. Suh, Y. S. Kim, and H. H. Lee. *J. Chem. Phys.*, **108**(3), 1253 (1998)
- [Sza03] G. Szamel and M. Muller. *J. Chem. Phys.*, **118**(2), 905 (2003)
- [TA00] T. Thurn-Albrecht, J. Schotter, G. A. Kastle, N. Emley, T. Shibauchi, L. Krusin-Elbaum, K. Guarini, C. T. Black, M. T. Tuominen, and T. P. Russell. *Science*, **290**(5499), 2126 (2000)
- [TA00a] T. Thurn-Albrecht, R. Steiner, J. DeRouchey, C. M. Stafford, E. Huang, M. Bal, M. Tuominen, C. J. Hawker, and T. P. Russell. *Adv. Mater.*, **12**(11), 787 (2000)

9 Bibliography

- [Tam97] J. Tamayo and R. García. *Appl. Phys. Lett.*, **71**(16), 2394 (1997)
- [Tur92] M. S. Turner. *Phys. Rev. Lett.*, **69**(12), 1788 (1992)
- [Tur94] M. S. Turner, M. Rubinstein, and C. M. Marques. *Macromolecules*, **27**, 4986 (1994)
- [vD95] M. A. van Dijk and R. van den Berg. *Macromolecules*, **28**(20), 6773 (1995)
- [Wal94] D. G. Walton, G. J. Kellogg, A. M. Mayes, P. Lambooy, and T. P. Russell. *Macromolecules*, **27**(21), 6225 (1994)
- [Wan98] L. Wang. *Appl. Phys. Lett.*, **73**(25), 3781 (1998)
- [Wan99] L. Wang. *Surf. Sci.*, **429**, 178 (1999)
- [Wan01] Q. Wang, P. F. Nealey, and J. J. de Pablo. *Macromolecules*, **34**(10), 3458 (2001)
- [Wan03] Q. Wang, P. F. Nealey, and J. J. de Pablo. *Macromolecules*, **36**(5), 1731 (2003)
- [Wha98] M.-H. Whangbo, G. Bar, and R. Brandsch. *Surf. Sci.*, **411**, L794 (1998)
- [Whi90] M. D. Whitmore and J. Noolandi. *J. Chem. Phys.*, **93**(4), 2946 (1990)
- [Whi92] M. D. Whitmore and J. D. Vavasour. *Macromolecules*, **25**(7), 2041 (1992)
- [Wil94] D. R. M. Williams. *Phys. Rev. E*, **49**(3), R1811 (1994)
- [Win96] R. G. Winkler, J. P. Spatz, S. Sheiko, M. Möller, P. Reineker, and O. Marti. *Physical Review B: Condensed Matter*, **54**(12), 8908 (1996)
- [Yok00] H. Yokoyama, T. E. Mates, and E. J. Kramer. *Macromolecules*, **33**(5), 1888 (2000)
- [Zha00] Q. Zhang, O. K. C. Tsui, B. Du, F. Zhang, T. Tang, and T. He. *Macromolecules*, **33**(26), 9561 (2000)

9 Bibliography

- [Zho93] Q. Zhong, D. Inniss, K. Kjoller, and V. Elings. *Surf. Sci.*, **290**, L688 (1993)
- [Zhu03] Y. Zhu, S. P. Gido, H. Iatrou, N. Hadjichristidis, and J. W. Mays. *Macromolecules*, **36**(1), 148 (2003)

10 List of Publications

During the course of this thesis the following papers have been published:

- A. Knoll, A. Horvat, K.S. Lyakhova, G. Krausch, G.J.A. Sevink, A.V. Zvelindovsky, and R. Magerle*,
"Phase Behavior in Thin Films of Cylinder-Forming Block Copolymers."
Phys. Rev. Lett. **89**(3), 035501 (2002)
- A. Knoll, R. Magerle, and G. Krausch*,
"Tapping Mode Atomic Force Microscopy on Polymers: Where Is the True Sample Surface?"
Macromolecules **34**(12), 4159 (2001)
- A. Knoll*, R. Magerle*, and G. Krausch,
"Phase Behavior in Thin Films of Cylinder-Forming ABA Triblock Copolymers: Experiments"
J. Chem. Phys., submitted (2003)
- A. Böker, H. Elbs, H. Hänsel, A. Knoll, S. Ludwigs, H. Zettl, V. Urban, V. Abetz, A.H.E. Müller, and G. Krausch*,
"Microscopic Mechanisms of Electric-Field-Induced Alignment of Block Copolymer Microdomains."
Phys. Rev. Lett. **89**(13), 135502 (2002)
- A. Böker, A. Knoll, H. Elbs, V. Abetz, A.H.E. Mueller, and G. Krausch*,
"Large Scale Domain Alignment of a Block Copolymer from Solution Using Electric Fields."
Macromolecules, **35**(4), 1319 (2002)
- M. Konrad, A. Knoll, G. Krausch, and R. Magerle*,
"Volume imaging of an ultrathin SBS triblock copolymer film."
Macromolecules, **33**(15), 5518 (2000)

10 List of Publications

- M. Lysetska, A. Knoll, D. Böhringer, T. Hey, G. Krauss, and G. Krausch*,
"UV light-damaged DNA and its interaction with human replication
protein A: an atomic force microscopy study."
Nucl. Acids. Res., **30**(12), 2686 (2002)
- N. Rehse, A. Knoll, M. Konrad, R. Magerle, and G. Krausch*,
"Surface reconstruction of an ordered fluid. An analogy with crystal
surfaces."
Phys. Rev. Lett., **87**(3), 035505 (2001)
- N. Rehse, A. Knoll, R. Magerle, and G. Krausch*,
"Surface Reconstructions of Lamellar ABC Triblock Copolymer
Mesostructures."
Macromolecules, **36**(9), 3261 (2003)
- H. Schmalz, A. Knoll, A.J. Müller, and V. Abetz*,
"Synthesis and Characterization of ABC Triblock Copolymers with Two
Different Crystalline End Blocks: Influence of Confinement on
Crystallization Behavior and Morphology."
Macromolecules, **35**(27), 10004 (2002)

Danksagung

Das Gelingen dieser Arbeit wäre ohne das passende Umfeld mit vielen hilfsbereiten Personen nicht möglich gewesen. Mein besonderer Dank gebührt:

Prof. Georg Krausch zum einen für die Möglichkeit an einem interessanten Thema in seinem Arbeitskreis arbeiten zu können, zum anderen für die fürsorgliche und gerechte Art seiner Betreuung, die genügend Freiheiten lässt, um ungewöhnliche Pfade betreten zu können.

Priv. Doz. Dr. Robert Magerle für die Betreuung, die vielen ausführlichen Diskussionen und die eindringlichen Ratschläge, die mir oft die Augen geöffnet haben.

Ganz besonderer Dank gilt der Arbeitsgruppe PC II für die sehr vielfältige und anregende Arbeitsatmosphäre:

Marina Lysetska für ihre andauernde Unterstützung und ihren Einsatz zur Wiedereinsetzung des Weihnachtsmanns.

Larisa Tsarkova für die gute Zusammenarbeit bei vielen Experimenten und für die anregenden Diskussionen.

Andriana Horvat für die Diskussionen über Simulation und Experiment und deren Gültigkeit.

Nico Rehse für seine Ausdauer als Büronachbar und seine bewunderswerte Organisationsfähigkeit, ohne die wir sicher die ein oder andere LAN verpasst hätten.

Helmut Hänsel für seine unglaubliche Hilfsbereitschaft und Diskussionsbereitschaft besonders in programmiertechnischer und theoretischer Hinsicht, für die uns gemeinsame Angewohnheit Experimente wochenlang zu automatisieren anstatt an einem Tag manuell zu messen und für die vielen meist netten Sticheleien, die den Laboralltag aufgelockert haben.

Heiko Zettl für die Organisation der Laborgegenstände, ohne die ein Auffinden "verlorener" Gegenstände unmöglich gewesen wäre, der Kaffeekasse und der

Gummibärchenbeschaffung.

Alex Böker für das Ermöglichen der "Grenoble" Abenteuer und die Hilfe bei allen chemischen Polymerfragen.

Frank Schubert für die Hilfeleistung bei vielerlei L^AT_EX- Problemen und die leckeren Zwei-Komponenten-Salate.

Stefan Höhn für seine Einsatzfreude bei den Experimenten, die sich in so manchem Spektrum bemerkbar gemacht hat, aber auch sehr schnell zu experimentellen Testaufbauten und vielen Daten geführt hat.

Matthias Konrad und Markus Hund für viele gemeinsame Experimente, Diskussionen und Ätzversuche.

Panteleimon Pan Panagiotou für seine menschliche Art, seine lautstarke (musikalische) Untermalung des Laboralltages und seine gute Freundschaft.

Und allen anderen Mitgliedern der PC II - Arbeitsgruppen, Sabine c Ludwigs, Kristin Schmidt, John Bosco, Dr. Wolfgang Häfner, Ute Lippert, Chris Cecco, Dr. Mark Geoghegan, Dr. Hubert Elbs, Dr. Andrej Voronov und Lena Shafranska, Tracy Chun Wang, Markus Gruber und Gustav Sauer für die gute Zusammenarbeit.

Ein besonderer Dank gilt auch Christiane Theurer und Sybille Zimmermann für die Hilfsbereitschaft in bürokratischen und organisatorischen Belangen, Carmen Kunert, Astrid Göpfert und Clarissa Abetz für ihre Mühe meine Proben mit dem Elektronenstahl zu untersuchen, Werner Reichstein für die Einführung und Hilfe am Ellipsometer, den Glasbläsern und der vorzüglichen NW I-Werkstatt rund um Herrn Krejtschi für die sehr gute und schnelle Realisierung von technischen Aufbauten.

Für den unersetzbaren alltäglichen Ausgleich zur Physik möchte ich meine Freunden außerhalb des Arbeitskreises danken, den "Würzburgern", der "Fröbel", den Squash- und den Batminton-Partnern und der LAN-Party-Truppe.

Meiner Familie danke ich für die große Unterstützung während des Studiums und während der Promotion.

Erklärung

Die vorliegende Arbeit wurde von mir selbstständig verfasst und ich habe dabei keine anderen als die angegebenen Hilfsmittel und Quellen benutzt. Ferner habe ich nicht versucht, anderweitig mit oder ohne Erfolg eine Dissertation einzureichen oder mich der Doktorprüfung zu unterziehen.

Bayreuth, den 02.07.2003

Armin Knoll